Fabrication and Chemical Applications of Polymer Microchannel-Microelectrode Chips

Graduate School of Science, Hokkaido University

Kosei UENO

Contents

Chapter 1.

Introduction

1.1 Microchip Chemistry

It is widely known that the development of various electronics devices/products in the past decades is based essentially on that of integrated circuits (IC). Personal computers, memories, cellular phones, and so on composed of a huge number of IC are fabricated by semiconductor micromachining technologies and, these are now widely used in daily life and have become the indispensable basis of the modern society. The minute structures and electronic circuits used in IC are mass-produced on silicon wafers by lithography. It is interesting to note that the key idea of lithography is the printing technique invented by Gutenberg in the 15th century, and the technique was applied later to a photoresist; photolithography is one of the greatest technological innovations in the 20th century. Micro-devices and -circuits can be duplicated and mass-produced by photolithography. This indicates that the most of modern technologies based on micromachining rely on photochemistry.

The technological progresses in microelectronics also influenced the research fields of chemistry. In the 1980's, as an example, microtechnologies mentioned above were applied successfully to fabricate microelectrodes,[1-5] microelectrode arrays,[6-12] interdigitated microelectrodes,[13-17] and so on. These electrodes are now used widely as sensors and detectors for various analytical equipments. On the other hand, Masuhara and his research group (Masuhara Microphotoconversion project, 1988 ~ 1993) proposed chemical researches by using microelectrodes[18-20] and microchemical systems,[21-25] and they elucidated the characteristics of the chemical phenomena and

reactions in minute dimensions. Besides this, the researches on microfluidic devices having minute flow channels were started independently in the beginning of 1990's. As an example, one of the world-wide chemical companies, Ciba-Geigy Co. in Switzerland (now, Novartis Pharmaceuticals Co.) began researches on integration of analysis systems onto a single silicon substrate: microelectrophoresis, micro liquid-chromatography, and so forth.[26-30] A miniaturized total analysis system (μ-TAS),[31-33] they proposed, is the novel concept which enables continuously and automatically a sampling, pre-treatment, injection, separation, detection of an analyte on a single solid substrate, called a microchip. The most important advantage of the use of a microchip is that it enables ultratrace amount analysis of a sample. Now, it is known that Manz (Imperial college) is a leading researcher in the field of μ-TAS.

In the middle of 1990's, the research on the microchip chemistry spread into academic fields. The research groups of Mathies, Manz, Harrsion, and Ramsey demonstrated independently miniaturized capillary electrophoresis systems fabricated on glass or solid substrates.[34-40] Nowadays, various research groups in the world are exploring integration of analysis and chemical systems on a single microchip. Most of microfluidc devices so far reported, however, have been fabricated on silicon or glass substrates by employing conventional photolithography and etching techniques. In different from such approaches, Whitesides and his research group reported fabrication of poly(dimethylsiloxane) (PDMS)-based microchannel chips on the basis of a molding method.[41-43] The molding method is very simple and does not require special facilities such as those for photolithography, since an embossed structure of a template is transferred easily to a polymer substrate. Therefore, various chemical laboratories fabricate PDMS-based microfluidic devices,[44-47] and the devices have contributed to the

development of the microchip chemistry.

On the basis of such research backgrounds, the research reports concerning microchip chemistry have increased since 1999, and over 1000 papers appeared until now. In particular, biological applications of a microfluidic device have received broad interest since it makes possible to analyze an ultratrace amount of expensive and rare biological samples (i.e., DNA,[48-54] RNA,[55-57] and proteins[58-60]) efficiently and quickly. It has been also reported that immunoassay such as enzyme linked immunoassay based on an efficient antigen-antibody reaction can be conducted in a micro space.[61-63] Furthermore, efficient heat transfer in a microfluidic device enables a polymerase chain reaction on a microchip.[64-67] These devices will be used in various medical scenes in the near future. In separation sciences, on the other hand, microchip-based electrophoresis systems and a chromatography system filled with silica in a microchannel have been reported.[68] In addition, nanofluidic devices have been demonstrated on the basis of nanotechnology or molecular self-assembly techniques.[69-73] These researches are indicative of further developments and progresses in the chemistry in nano space.

Besides fabrication of a microchip, the development of the detection system combined with a microfluidic device is also the most important subject in the research fields of the microchip chemistry. As an example, laser-induced fluorescence (LIF),[74-78] mass spectrometry,[79-81] thermal lens microspectroscopy (TLM),[82-84] surface plasmon resonance,[85-87] and electrochemical detection[88-90] techniques have been so far studied, and each analytical technique has both advantages and disadvantages. LIF and TLM are high sensitive detection techniques, and single molecule detection can be also done. In practice, single DNA and protein fluorescence detection have been reported.[91-94] Mass spectrometry is also very useful as high selective and sensitive techniques for analysis

in a microchip and the technique has been currently used for a protein chip. Nonetheless, these detection systems are not in general mobile. This is the main drawback of the detection systems mentioned above. Although the sensitivity of an electrochemical detection is not so high compared to that of emission spectroscopy as an example, electrochemical analysis is very advantageous over above-mentioned methods, since an electrode as a detector can be miniaturized arbitrarily and, thus, incorporated into a microfluidic device and the total system can be miniaturized.

The researches on microfluidic devices are not limited toward the integration of an analysis system on a microchip. In the end of 1990's, in practice, Ehrfeld et al. in Institute for Microtechnology, Mainz, reported for the first time a microreactor chip for organic synthesis.[95,96] Conventionally, a microreactor has been designed and proposed to control the product selectivity and reaction yield of a chemical reaction in minute space modified with self-assembled mesoporous silica or zeolite in the field of catalytic chemistry.[97,98] The concept of a microreactor chip or microreaction system, on the other hand, is different essentially from conventional microreactors mentioned above and, the system offers many advantage over traditional large-scale organic synthesis or conventional microreactor in terms of efficient mass-transfer, high effective heat management, a high specific surface (interface) area, a decrease of wastes and toxicity in various chemical reactions. Chemical synthesis of highly harmful and explosive compounds can be also conducted safely in a microchip. In deed, microreactor chips have been applied successfully to various chemical reaction systems with typical examples being enzymatic reactions[99-101] and organic synthetic reactions.[102-104]

Various researches on microchips were demonstrated in the past decade as described above and a microchip is now interested in the wide research fields of

chemistry. In a practical view point, however, microreaction systems so far reported are still infant and are in the stage of research and development. Nonetheless, since a microchip can be employed in various fields, the development of microchip systems is explored by many institutions and companies over the world. It is certainly true that the devices are expected to be applied to environmental and medical analysis systems as well as to microchemical reaction systems. In order to realize such concepts, basic researches on microchannel chips are absolutely necessary. For further development of the microchip chemistry, in particular, a novel and versatile fabrication method of a microchip integrated with functional elements and characterization of the devices are needed, which is the main issue of the present research as described in details in the following sections.

1.2 Electrochemistry and Spectroscopy by Using Polymer Microfluidic Devices

A number of microfluidic devices have been fabricated by semiconductor micromachining techniques on the basis of a silicon or glass substrate. Although microfabrication techniques have certainly high potential to produce microdevices, they are not still conventional to ordinary chemical laboratories owing to the needs of both expensive equipments and special facilities (i.e., a dry etching system, a clean room, and so forth). As a more convenient method to fabricate microstructures, several organic polymer-based methods in stead of using a silicon or glass substrate have been proposed. In this study, therefore, polymer microfluidic devices integrated with functional elements such as microelectrodes and microheaters were fabricated, and these devices were combined with microelectrochemical and microspectroscopic systems to elucidate

characteristics of chemical and physical processes in the microchip. In the following, some backgrounds of microelectrochemistry, microspectroscopy, and polymer microchips are overviewed.

1.2.1 Microelectrochemistry

Microtechnologies have succeeded in fabricating microelectrodes as electroanalytical tools for liquid chromatography,[105,106] capillary electrophoresis,[107,108] bio-sensor,[109-111] and so forth. Microelectrochemical approaches offer many advantage over conventional electrochemical methods by using a millimeter-sized disk electrode. One of the most important characteristics of the chemistry based on a microelectrode is the fact that precise experiments with a low charge current can be conducted. The presence and appearance of a charging current sometimes disturb quantitative analysis in an electrochemical experiment, since a charging current does not concern with a faradaic current of a solute, but is generated by charging the capacitance in the electric double layer at an electrode. In the case of a microdisk or microband electrode, the faradaic current density increases owing to its hemi-spherical or hemi-cylindrical diffusion profile, respectively. On the other hand, the charging current decreases in proportional to the decrease in an electrode surface area. Therefore, the ratio of the faradaic current to the charging current is much larger for a microelectrode as compared to that by a conventional electrode.

As another characteristic, steady- or quasi-steady-state current can be obtained by using a microelectrode. Namely, it is well known that the diffusion profile of a solute around a millimeter-sized disk electrode exhibits a one-dimensional linear diffusion profile, while that of a microdisk electrode is characterized by a spherical diffusion and,

therefore, a steady-state current is observed. An observation of a steady-state current at a microelectrode is very advantageous, since it makes easy a quantitative analysis of the voltammogram in cyclic voltammetry (CV). Generally, a microband electrode is employed in microelectrochemical measurements, since it affords a relatively large current as compared to a microdisk electrode and the electrochemical responses of the electrode can be dealt similar to those at a microdisk electrode.

Microfluidic devices integrated with microelectrodes have attracted current interests as a new tool for an electrochemical study in minute dimension as well as for electrochemical detectors or sensors in analytical equipments, with a typical example being electrophoresis microchips.[112,113] Also, electroanalytical tools are very advantageous over traditional detection systems in terms of a low cost, low energy, portability, and so forth. As an example, Girault and his co-workers reported fabrication of a polymer-based channel chip integrated with electrodes by using a laser ablation technique and, demonstrated characteristic electrochemical responses in the microchannel.[114] In a restricted space such as a microchannel, it is worth noting that the electrochemical responses at an electrode are different from those in a bulk system. The electrochemical responses of a microband electrode in a restricted volume have been reported by Engblom et al., demonstrating characteristics of the diffusion current at a tubular band electrode.[115] Other research groups also have reported that the electrochemical responses characteristics to a quasi-thin-layer cell can be obtained even by the use of a microelectrode, when an electrode is placed in a small volume.[116,117] In the case of a thin layer cell, namely, a reactant is electrolyzed completely and quickly in a small space and molecular diffusion of the reactant is restricted by the presence of the cell wall. In such a case, the peak current, i_p, is in proportion to a sweep rate, ν, as given

by eq. (1-1),

$$i_p = n^2F^2\nu WC_R^0/4RT \qquad (1\text{-}1)$$

where C^0_R is the concentration of a solute. n, F, R, and T are the number of an electron transferred, the Faraday constant, the gas constant, and a temperature, respectively. The electrochemical responses of a microelectrode positioned in a small space such as those in a microchannel are thus considered to be similar to those in a thin layer cell, and would be analyzed by a computer simulation.

Since a microdisk or microband electrode(s) can be accommodated arbitrarily in space, it provides new analytical modes for micrometer-sized particles and small domains. In practice, electrochemical studies on single cells[118-121] and mass transfer or electron transfer processes at oil droplet/water interfaces[122-124] have been reported. A scanning electrochemical microscope (SECM) has been also developed to analyze and image a small domain of several tens of nanometers.[125-128] Furthermore, dual band-microelectrodes and an interdigitated microelectrode (IDE, see also Figure 1-1) composed of a couple of a microelectrode have been applied to detect an electrochemical intermediate(s). As an example, when a solute is oxidized at one of the comb-like electrodes in the IDE and its oxidized solute is reduced at other electrode simultaneously, the concentrations of the oxidized and neutral species becomes in a steady state known as “redox cycles” and, therefore, the current value is amplified.[129-131] By using such characteristics, the IDE is used as a high sensitive electrochemical detector for liquid chromatography or flow injection analysis.[132-134] Microelectrodes have been thus employed widely in various research fields.

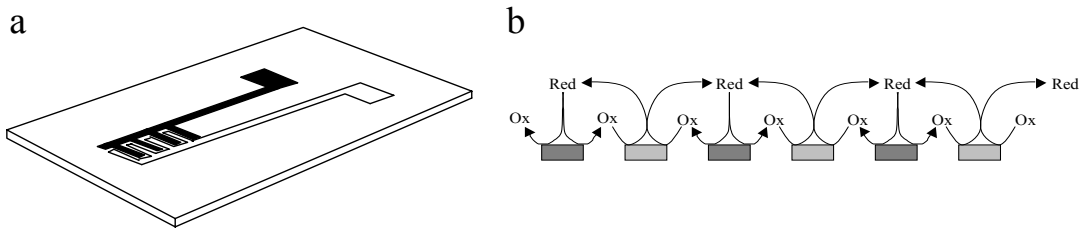

Figure 1-1 (a) Illustration of an interdigitated microelectrode. (b) Schematic drawing of the redox cycles.

1.2.2 Microspectroscopy

Microspectroscopy is a very powerful means to elucidate chemical processes in minute dimensions and is also combined with microfluidic devices. Besides chemistry, the methodology is certainly very useful as a bioanalytical technique and, in practice, it has been applied to study the properties of DNA, a protein, a living cell, and so on.[135-137] As an example, Dittrich et al. reported ultrasensitive confocal detection of fluorescent living bacterial cells in a microfluidic channel and, demonstrated precise sorting and simultaneous spectroscopic characterization of individual cells in the fluid phase.[138] In particular, fluorescence microspectroscopy can detect in single molecule level, so that relevant research fields have grown in these years.[139-141] In addition to fluorescence spectroscopy, microspectroscopic techniques have been also applied successfully to absorption, infrared, Raman spectroscopy, and so on.[142-144]

A laser trapping microspectroscopy technique first proposed by Masuhara et al. is also a very versatile tool to investigate individual single microparticles in solution.[145-147] Chu et al. have demonstrated *in-situ* analysis of a single DNA under solution-flow

conditions by using the laser-trapping method.[148] Kitamura and his coworkers have conducted spectroscopic studies on polymer particles, microdroplets, microcapsules, an ion-exchange resin, and so on. As a typical example, they elucidated the distribution characteristics of a dye molecule in single melamine-resin-wall microcapsules by laser trapping absorption microspectroscopy[149,150] and the ion-exchange processes in polymeric resin particles by dynamic fluorescence microspectroscopy. [151,152]

Among various experimental modes in studying chemical processes in minute dimensions, a combination of an electrochemical technique with spectroscopy is very fruitful, since simultaneous electrochemical and spectroscopic analyses offer both high sensitivity and selectivity in analysis. Nakatani et al. studied an electron transfer reaction across a single microdroplet/water interface by laser trapping spectroscopy combined with a microelectrochemical system.[153,154] Furthermore, microfluidic-electrode devices have been combined successfully with a spectroscopic technique, with a typical example being *in-situ* monitoring of electrogenerated chemiluminescence (ECL) in a microchannel. As an example, Zhan et al. have reported ECL spectra of $Ru(bpy)_3^{2+}$ (bpy = 2,2'-bipyridine) in a PDMS microchannel-electrode chip.[155,156] Since fresh oxidized and reduced species of $Ru(bpy)_3^{2+}$ are produced steadily and simultaneously at the electrode under solution-flow conditions, highly sensitive detection of ECL is achieved by using the channel-electrode chip.

Space-resolved spectroscopy has high potentials to pursue chemical reactions proceeding in a microchannel. Under solution-flow conditions in a microchannel, a chemical reaction can be induced continuously and transient phenomena can be observed repeatedly at an arbitrary position in the channel along the solution-flow direction. This indicates that a chemical reaction(s) can be induced sequentially in a

microchannel and its dynamic processes can be monitored by space-resolved spectroscopy. These discussions indicate clearly that microspectroscopy is very advantageous to elucidate characteristics of chemical and physical processes in a microchannel chip.

1.2.3 Microfluidic Devices

i) Photolithography

The standard methods for fabricating microfluidic devices have been developed on the basis of those employed in the microelectronics industry. Harrison and his co-workers have demonstrated fabrication of a glass-based microfluidic device.[157] They used photolithography-isotropic chemical etching to fabricate a channel structure and a thermal bonding method for the sealing the channel substrate. Such a fabrication technique has been employed widely in various glass microchip researches. Also, the methodology was used partly to fabricate a polymer microchannel chip in the present study. In the following, therefore, conventional photolithographic procedures of substrate cleaning, barrier layer formation, photoresist application, soft baking, mask alignment, exposure, development, and hard-baking are described. The photolithographic procedures are illustrated in Figure 1-2.

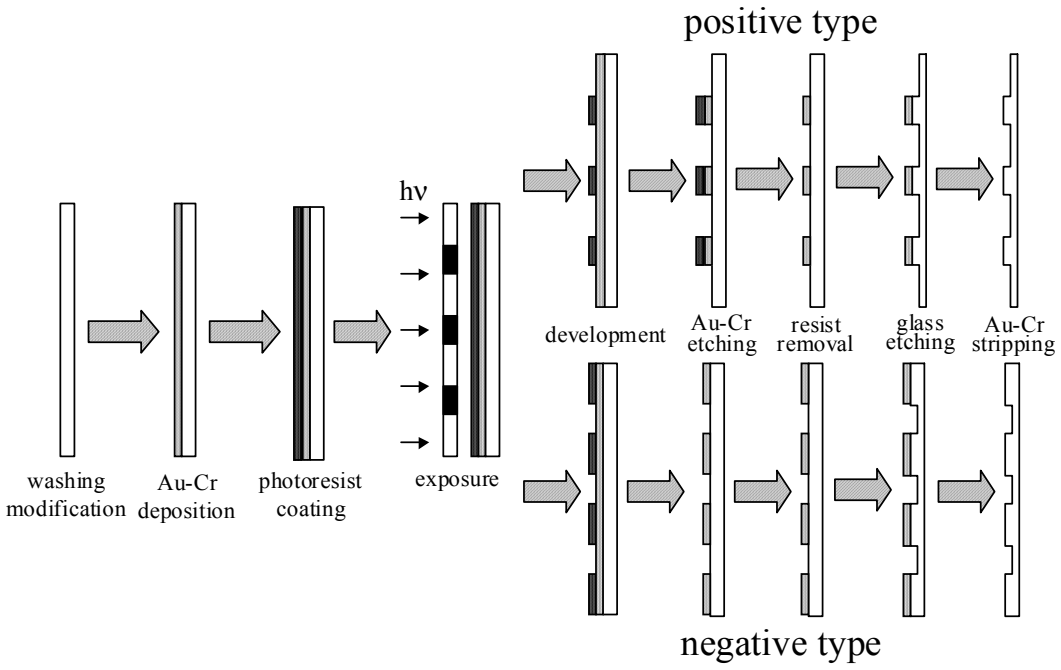

Figure 1-2 Schematic illustration of the photolithographic procedures.

In the first step, a glass plate is cleaned chemically to remove particulate matters and any traces of organic, ionic, and metallic impurities on the surface by a concentrated aqueous sulfuric acid solution. After cleaning, a thin Au-Cr film serves as a barrier layer is deposited on the surface of the substrate. After formation of the Au-Cr layer, a photoresist is spin-coated onto the surface of the substrate.

There are two types of a photoresist: positive and negative types. In the case of a positive-type resist, the irradiated region of the resist layer through a photomask is decomposed photochemically and becomes soluble in a developer. The irradiated region is then washed away by the developer solution, leaving the spatial pattern of the unirradiated resist layer. The spatial pattern of the photomask, therefore, is transferred exactly on the chip substrate. On the other hand, a negative resist behaves just opposite

to a positive resist. Exposure of UV light to a negative resist leads to photopolymerization of the material and the irradiated region becomes insoluble. Therefore, the irradiated region of the negative resist remains on the surface and the relevant developer solution can remove only the unirradiated region. In the case of a negative photoresists, therefore, the spatial pattern opposite to that of a photomask is fabricated on the substrate.

One of the most important steps in photolithography is mask alignment. A photomask is a square glass plate with a patterned metal film on one side, and is put tightly on a resist/substrate. Therefore, the pattern can be transferred precisely onto the resist/substrate surface. Once a photomask is aligned accurately with the pattern on a substrate, lithography makes possible to fabricate three-dimensional structure on the substrate.

The next step in the photolithographic processes is development of the resist layer. Development of a resist layer can be done simply by treating the layer with an appropriate solution for a given resist material. After development, the exposed substrate surface is etched by reactive-ion or wet etching, depending on nature of the substrate material. The methodology is advantageous to create a pattern with high spatial resolution (about 100 nm) and, parallel processing-photolithography and etching can create any patterns in a single step. Although it is certainly true that photolithography has many advantages for fabricating microstructures, the fabrication requires expensive facilities and sophisticated techniques. Clearly, the photolithographic fabrication of a glass or silicon chip is inconvenient to versatile applications of channel chips.

ii) Polymer Microfluidic Devices

Fabrication of microfluidic devices in the next generation requires cheaper mass production technologies for practical and commercial applications. In this respect, polymer- or plastic-based microfluidic devices could play essential roles in the development of future μ-TAS and lab-on-a-chip systems. However, polymer materials have both several advantages and disadvantages when they are applied as a chip material. For example, a solvent(s) used in the experiments might affect integrity of the microdevice. Namely, many polymer materials such as polystyrene, poly(methyl methacrylate) (PMMA), and poly(vinyl chloride) are not tough enough to ordinary organic solvents and might adsorb chemical compounds. However, these problems can be improved partly by fluorination of the surface of a polymer substrate. On the other hand, polymer materials are very advantageous in respect to a good processibility for fabricating a microdevise, optically properties (i.e., transparent in the visible region), an easy bonding ability between channel and cover plates as a fluidic device, and easy modification of polymer-surfaces. In addition to such advantages, a wide variety of organic polymer materials having thermal, chemical, physical, and surface-derivatization properties can be selected arbitrary. Therefore, polymer devices are important as a material for microchemical devices in the next generation.

So far, most of polymer microfluidic devises have been fabricated by laser ablation,[158,159] PDMS molding,[41-47] and imprinting methods.[160-162] In such methods, a silicon or glass substrate possessing a desired microstructure is used as a template and the microstructure is duplicated on a polymer substrate under appropriate conditions. Therefore, once one obtains a template, a desired number of polymer-based microstructures can be produced without complicated microfabrication techniques,

which is one of the most important advantages of the polymer device over silicon- and glass-based devices. Many commercially available polymers such as polystyrene, PET (polyethylene terephthalate), PMMA, and so on can be used as a device substrate.

Microfabrication of polymer materials by laser ablation involves absorption of pulsed laser light (e.g., an excimer laser) by the substrate, which results in sudden heat generation and subsequent thermal and/or photochemical bonds breaking composed of the polymer.[158] Such heat generations also produces shock waves, which causes deposition of the decomposition products of the polymer (e.g., various radicals, C_2H_2, CO_2, or CO) onto the fabricated surface.

On the other hand, microfabrication of a polymer substrate by an imprinting method is applied usually to organic polymers having a relatively low glass transition temperature (T_g), which ranges between 100 and 180 °C. Generally, the imprinting technique uses a silicon template fabricated by silicon micromachining or LIGA processing. Polymer microchannels can be fabricated by pressing a template with a plastic substrate upon heating above T_g of the polymer substrate. This method can be applied to fabricating the microstructures with a low aspect ratio because of elastic properties of organic polymers. As an attractive and wide-spread polymer, furthermore, poly(dimethylsiloxane) (PDMS) is well known and fabricated widely by a molding method. A solution of PDMS and a curable agent is poured onto a positive embossed template, by which a microfluidic channel with a relatively high aspect ratio can be fabricated after curing at 65 °C for several hours. High aspect ratio structures can be obtained since the microstructure of a template is transferred precisely to a PDMS substrate.

The final stage of fabrication is bonding between a cover plate and a

microstructured substrate as a fluidic device. In most cases, a cover plate and a channel substrate made of the same material with the channel substrate is annealed at near its T_g for bonding. In the case of PDMS, a PDMS substrate with microstructures can be contacted simply with a PDMS cover plate or glass plate at room temperature. A polymer device fabricated by low-temperature annealing such as PDMS and polystyrene substrates is very attractive, since a glass-based device fabrication requires extremely high temperature (~600 °C) for bonding with a cover plate. Polymer microfluidics have been fabricated by various approaches as mentioned above, and also their applications are expected to be a key technology for fabricating novel analysis and chemical systems.

iii) Solution-Flow Characteristics in Microfluidic Devices

Microfluidic devices have been combined with electroosmotic pumping and electrophoretic separations. An application of DC voltages to the electrodes set between both ends of an electrolyte-filled channel produces an electroosmotic force as a pumping force of a solute, when the channel walls possess fixed charges. Electroosmotic pumping can control simply the flow direction by switching the polarity of the DC voltage, while pressure driven flow requires a valve to control a flow direction. Furthermore, electroosmotic flow can separate charged analytes on the basis of the difference in an electrophoretic mobility of an analyte. However, electroosmotic pumping has several problems: reproducibility of a flow velocity, adsorption of a high ionic-strength sample, and so forth.

On the other hand, pressure driven flow (laminar flow) can control easily a flow velocity and realizes smooth flow of a liquid without turbulence even at a low flow

velocity. As a flow velocity increases, inertia of a fluid overcomes the frictional force between a fluid and a channel-wall, and turbulence occurs. It is well known that laminar flow takes place at a Reynolds number (Re) below ~2000,

$$\mathrm{Re} = \frac{u\rho l}{\eta} \qquad (1\text{-}2)$$

where u is a flow velocity, ρ is the density of a fluid, η is the viscosity of a fluid, and l is a channel diameter. One of the basic laws of fluid mechanics for pressure driven laminar flow under so-called no-slip boundary conditions indicates that the fluid velocity at the walls must be zero. This produces a parabolic velocity profile within a channel as illustrated in Figure 1-3. Flow characteristics of a fluid in a minute channel are described by Navier-Stokes equations. These equations can be derived from the principles of conservation of masses, momentum, and energy.

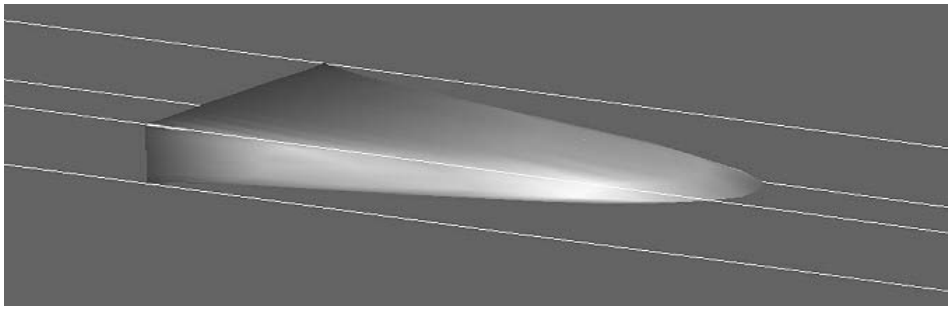

Figure 1-3 Velocity profile in a microchannel with an aspect ratio of 1:5 under conditions of pressure driven flow.

Laminar flow is generally seen in microfluidic devices because of a narrow channel width or depth. When two miscible fluids are introduced once to a single channel, laminar flow in a microfluidic channel produces individual parallel streams of

the fluids, and mixing of two fluids occurs only through diffusion along the channel-width direction. For example, a fluorometric sensor can be constructed on the basis of laminar flow.[163] Other novel applications of laminar flow-based analysis and chemical reactions are expected, which is another issue of the research relevant to the microchip chemistry.

1.3 Purpose and Contents of the Thesis

The purpose of the thesis is to fabricate and characterize both polymer microchannel chips and the chips integrated with functional elements (microelectrode and microheater), and to elucidate chemical reaction processes in the chips on the basis of in-situ microspectroscopy and microelectrochemical techniques. As described in the previous sections, polymer-based microdevices can be fabricated by several methods. Among these, an imprinting method is a very powerful means to fabricate polymer microchannel chips and the chip can be integrated with a functional element such as an electrode(s) or heater(s). Besides these, an imprinting method enables fabrication of arbitrary-structured channel chip (size, shape, length, and so on) very easily. Therefore, a microchannel chip can be used as a very versatile analysis/reaction system, since chemical reactions and/or phenomena are influenced by the channel geometries such as the size and shape of a channel. By utilizing these characteristics and advantages of polymer microchannel chips, the present study was focused on exploring reaction-control in space (channel geometries; size and shape) and time (solution flow velocity). It is worth noting that, although a number of the study relevant to the microchip chemistry have been so far reported, the number of the study on a microchannel-electrode chip and its combination with microspectroscopy is still limited.

Clearly, the basic work along the line mentioned above is worth exploring in detail.

The thesis consists of nine chapters.

In Chapter 1, the roles of a microchip in various sciences and the historical background of the microchip chemistry were described. As the basis for quantitative analyses of chemical and physical events proceeding in a microchip, general characteristics of microelectrochemistry and microspectroscopy techniques were overviewed. The basic concepts on photolithography, polymer microdevices, and solution-flow characteristics in a microfluidic device were also described.

In Chapter 2, a novel fabrication method of polymer microchannel chips on the basis of an imprinting method was outlined, together with the results on characterization of the fabricated chips by a scanning electron microscope and microspectroscopic techniques. The solution-flow characteristics in the fabricated channel chip were also demonstrated as experimental checks of the performances of the channel solution-flow - microspectroscopy system.

In Chapter 3, liquid/liquid extraction of an Al^{3+}-DHAB (DHAB = 2,2'-dihydroxyazobenzene) from water to an oil in a microchannel chip was studied on the basis of spatially-resolved fluorescence spectroscopy. When two immiscible fluids were brought together into the channel chip by pressure-driven flow at the same flow velocity, a stable parallel stream was observed for each phase without mutual mixing. Extraction of Al^{3+}-DHAB from water to an oil was then studied as a fluorescence intensity profile of the complex in the oil phase along the flow direction as well as along the channel-width direction. Numerical simulations of liquid/liquid extraction were also conducted and the results were compared with the experimental observations. Furthermore, analogous experiments with those mentioned above were conducted by

using a silicon channel chip having the same geometries with those of the polymer chip. Solvent effects and the channel-shape effects (a symmetrical or unsymmetrical zigzag-side-walled structure) on the liquid/liquid extraction efficiency were also studied. On the basis of these results, the performances of the fabricated polymer microchannel chips and characteristics of extraction and the mass transfer processes in the microchannel chips were discussed in detail.

In Chapter 4, a photocyanation reaction of pyrene (PyH) across an oil/water interface in a microchannel chip was described. As a typical example of the photoreaction, an aqueous NaCN solution and a propylene carbonate solution of PyH and 1,4-dicyanobenzene were brought separately into a Y-structured microchannel. It was shown that light irradiation on the whole of the channel chip resulted in formation of 1-cyanopyrene (PyCN). The experimental results demonstrated that the interfacial photochemical reaction of PyH proceeded efficiently along the water/oil solution-flow in the channel, and the results were discussed in terms of the flow velocity and the specific interface area between the water and oil phases.

In Chapter 5, characteristic electrochemical responses in the polymer microchannel chips integrated with dual microband electrodes were elucidated in detail on the basis of voltammetry and chronoamperometry. A cyclic voltammetry of 1-hydroxyferrocene (FeCp-OH) in water demonstrated that the electrode responses in the microchannel chip were best characterized by one-dimensional diffusion along the channel length, reflecting the structural dimension of the channel. The characteristic electrochemical behavior was demonstrated on the basis of generation-collection mode experiments under solution-flow conditions, and the experimental results were compared with those predicted by computer simulations.

In Chapter 6, a spectroelectrochemical study on the perylene (Pe) cation radical generated in microchannel-electrode chips was described. A space-resolved absorption spectroscopy enabled *in-situ* analyses of the Pe cation radical in the channel, and the applied potential dependence of the absorbance of the Pe cation radical was compared with the current-potential curve observed at the electrode to elucidate the formation mechanism of the cation radical. Since the dimer cation radical of Pe was also produced under high Pe concentration and low solution-flow velocity conditions, the formation and disappearance processes of the monomer and dimer cation radicals of Pe in the channel were followed by the flow velocity and position dependences of the absorption spectra.

In Chapter 7, one-step electrochemical cyanation reaction of PyH in microchannel-electrode chips was demonstrated. An acetonitrile solution of PyH containing tetra-*n*-butylammonium perchlorate and an aqueous NaCN solution were brought into the chip. Oxidation of PyH at the working band electrode in the channel (1.5 V vs. Ag) produced 1-cyanopyrene (PyCN) and 1,3-dicyanopyrene ($Py(CN)_2$). The product selectivity between PyCN and $Py(CN)_2$ was discussed on the basis of the results by the large-scale reaction and the microchip reaction. In the case of the oil/water interfacial reaction system, furthermore, the microchip experiments as a function of the flow velocity and the electrode position in the channel demonstrated that the yield of PyCN as the sole product could be controlled arbitrary. *In-situ* space-resolved absorption spectroscopy of the electrochemical intermediate and numerical simulations of the mass transfer processes of a solute in the channel were also conducted and, their implications to the reaction mechanisms were discussed in detail.

In Chapter 8, the temperature profile of the solution phase in the microchannel in

the vicinity of the microheater integrated in a microchip was evaluated by space- and time-resolved fluorescence microspectroscopy and, the chip was then applied to control the thermal phase transition of an aqueous poly(*N*-isopropylacrylamide) (PNIPAM) solution. The temperature profile showing below or above the phase transition temperature (i.e., 32 °C) and the solution-flow profile in the microchannel were visualized on the basis of the PNIPAM particle formation. The results were discussed by comparing with the temperature profile evaluated by the microspectroscopy. Furthermore, the microchannel-heater chip was applied to the thermal reaction between benzaldehyde and malononitrile in methanol, giving benzilidenemalononitrile (BMN) as the product. The reaction yields of BMN obtained by using the microchip were discussed in terms of the flow velocity and the heater geometry.

In Chapter 9, the principal results of the study were summarized and future perspective of the study was overviewed.

1.4 References

1) Fleishmann, M.; Pons, S.; Rolison, D. R.; Scmidt, P. P. eds. "*Ultramicroelectrodes*" **1987**, Datatech Systems, North Carolina.

2) Bard, A. J. ed. "*Electroanalytical Chemistry*" **1988**, Vol. 15, Marcel Dekker, New York.

3) Kittlesen, G. P.; White, H. S.; Wrighton, M. S. *J. Am. Chem. Soc.* **1985**, 107, 7373-7380.

4) Murakami, Y.; Takeuchi, T.; Yokoyama, K.; Tamiya, E.; Karube, I.; Suda, M. *Anal. Chem.* **1993**, 65, 2731-2735.

5) Ura, H.; Nishina, T.; Uchida, I. *J. Electroanal. Chem.* **1995**, 396, 169-173.

6) Weber S. G. *Anal. Chem.* **1989**, 61, 295-302.

7) Thormann, W.; Van den Bosch, P.; Bond, A. M. *Anal. Chem.* **1985**, 57, 2764-2770.

8) Fosdick, L. E.; Anderson, J. L. *Anal. Chem.* **1986**, 58, 2481-2485.

9) Long, J. T.; Weber, S. G. *Anal. Chem.* **1988**, 60, 2309-2311.

10) Licht, S.; Cammarata, V.; Wrighton, M. S. *Science* **1989**, 243, 1176-1178.

11) Uosaki, K.; Okazaki, K.; Kita, H.; Takahashi, H. *Anal. Chem.* **1990**, 62, 652-656.

12) Cammarata, V.; Talham, D. R.; Crooks, R. M.; Wrighton, M. S. *J. Phys. Chem.* **1990**, 94, 2680-2684.

13) Matsue, T.; Aoki, A.; Abe, T.; Uchida, I. *Chem. Lett.* **1989**, 133-136.

14) Lindholm-Sethson, B.; Orr, J. T.; Majda, M. *Langmuir* **1993**, 9, 2161-2167.

15) Dennison, M. J.; Hall, J. M.; Turner, A. P. F. *Anal. Chem.* **1995**, 67, 3922-3927.

16) Morita, M.; Niwa, O.; Horiuchi, T. *Electrochim. Acta* **1997**, 42, 3177-3183.

17) Tomcik, P.; Jursa, S.; Mesaros, S.; Bustin, D. *J. Electroanal. Chem.* **1997**, 423, 115-118.

18) Nakatani, K.; Uchida, T.; Funakura, S.; Sekiguchi, A.; Misawa, H.; Kitamura, N.; Masuhara, H. *Chem. Lett.* **1993**, 717-720.

19) Pásztor, K.; Sekiguchi, A.; Shimo, N.; Kitamura, N.; Masuhara, H. *Sens. Actuat. B: Chem.***1993**, 12, 225-230.

20) Uchida, T.; Sugimura, H.; Sekiguchi, A.; Kitamura, N.; Shimo, N.; Masuhara, H. *J. Electroanal. Chem.* **1993**, 351, 343-348.

21) Misawa, H.; Koshioka, M.; Sasaki, K.; Kitamura, N.; Masuhara, H. *Chem. Lett.* **1991**, 469-472.

22) Ishikawa, M.; Misawa, H.; Kitamura, N.; Irie, M.; Masuhara, H. *Chem. Lett.* **1992**,

311-314.

23) Koshioka, M.; Misawa, H.; Sasaki, K.; Kitamura, N.; Masuhara, H. *J. Phys. Chem.* **1992**, 96, 2909-2914.

24) Sugimura, H.; Uchida, T.; Kitamura, N.; Masuhara, H. *Chem. Lett.* **1993**, 379-382.

25) Nakatani, K.; Misawa, H.; Sasaki, K.; Kitamura, N.; Masuhara, H. *J. Phys. Chem.* **1993**, 97, 1701-1706.

26) Manz, A.; Fettinger, J. C.; Verpoorte, E. M. J.; Luedi, H.; Widmer, H. M.; Harrison, D. J. *Trend. Anal. Chem.* **1991**, 10, 144-149.

27) Manz, A.; Harrison, D. J.; Verpoorte, E. M. J.; Fettinger, J. C.; Paulus, A.; Luedi, H.; Widmer, H. M. *J. Chromatogr.* **1992**, 593, 253-258.

28) Effenhauser, C. S.; Manz, A.; Widmer, H. M. *Anal. Chem.* **1993**, 65, 2637-2642.

29) Effenhauser, C. S.; Paulus, A.; Manz, A.; Widmer, H. M. *Anal. Chem.* **1994**, 66, 2949-2953.

30) Raymond, D. E.; Manz, A.; Widmer, H. M. *Anal. Chem.* **1994**, 66, 2858-2865.

31) Harrison, D. J., Van Den Berg, A. Eds. "*Micro Total Analysis Systems* '*98*" **1998**, Kluwer Academic Publishers, Dordrecht.

32) Manz, A.; Becker, H. Eds. "*Microsystem Technology in Chemistry and Life Science*" **1999**, Springer-Verlag, Berlin.

33) Baba, Y.; Shoji, S.; van den Berg, A. Eds. "*Micro Total Analysis Systems 2002*" **2002**, Kluwer Academic Publishers, Dordrecht.

34) Harrison, D. J.; Manz, A.; Fan, Z.; Luedi, H.; Widmer, H. M. *Anal. Chem.* **1992**, 64, 1926-1932.

35) Harrison, D. J.; Glavina, P. G.; Manz, A. *Sens. Actuat. B: Chem.* **1993**, B10, 107-116.

36) Harrison, D. J.; Fluri, K.; Seiler, K.; Fan, Z.; Effenhauser, C. S.; Manz, A. *Science* **1993**, 261, 895-897.

37) Jacobson, S. C.; Hergenroder, R.; Koutny, L. B.; Ramsey, J. M. *Anal. Chem.* **1994**, 66, 1114-1118.

38) Jacobson, S. C.; Hergenroder, R.; Moore, A. W. Jr.; Ramsey, J. M. *Anal. Chem.* **1994**, 66, 4127-4132.

39) Woolley, A. T.; Sensabaugh, G. F.; Mathies, R. A. *Anal. Chem.* **1997**, 69, 2181-2186.

40) Liu, S.; Shi, Y.; Ja, W. W.; Mathies, R. A. *Anal. Chem.* **1999**, 71, 566-573.

41) Duffy, D. C.; McDonald, J. C.; Schueller, O. J. A.; Whitesides, G. M. *Anal. Chem.* **1998**, 70, 4974-4984.

42) Anderson, J. R.; Chiu, D. T.; Jackman, R. J.; Cherniavskaya, O.; McDonald, J. C.; Wu, H.; Whitesides, S. H.; Whitesides, G. M. *Anal. Chem.* **2000**, 72, 3158-3164.

43) Stroock A. D.; Dertinger, S. K. W.; Ajdari, A.; Mezic, I.; Stone, H. A.; Whitesides, G. M. *Science* **2002**, 295, 647-651.

44) Hosokawa, K.; Fujii, T.; Endo, I. *Anal. Chem.* **1999**, 71, 4781-4785.

45) Linder, V.; Verpoorte, E.; Thormann, W.; de Rooij, N. F.; Sigrist, H. *Anal. Chem.* **2001**, 73, 4181-4189.

46) Kim, J. S.; Knapp, D. R. *Electrophoresis* **2001**, 22, 3993-3999.

47) Yamaguchi, A.; Jin, P.; Tsuchiyama, H.; Masuda, T.; Sun, K.; Matsuo, S.; Misawa, H. *Anal. Chim. Acta* **2002**, 468, 143-152.

48) Fan, Z. H.; Mangru, S.; Granzow, R.; Heaney, P.; Ho, W.; Dong, Q.; Kumar, R. *Anal. Chem.* **1999**, 71, 4851-4859.

49) Koutny, L.; Schmalzing, D.; Salas-Solano, O.; El-Difrawy, S.; Adourian, A.;

Buonocore, S.; Abbey, K.; McEwan, P.; Matsudaira, P.; Ehrlich, D. *Anal. Chem.* **2000**, 72, 3388-3391.

50) Lagally, E. T.; Medintz, I.; Mathies, R. A. *Anal. Chem.* **2001**, 73, 565-570.

51) Buchholz, B. A.; Doherty, E. A.; Albarghouthi, M. N.; Bogdan, F. M.; Zahn, J. M.; Barron, A. E. *Anal. Chem.* **2001**, 73, 157-164.

52) Hofmann, O.; Voirin, G.; Niedermann, P.; Manz, A. *Anal. Chem.* **2002**, 74, 5243-5250.

53) Paegel, B. M.; Yeung, S. H. I.; Mathies, R. A. *Anal. Chem.* **2002**, 74, 5092-5098.

54) Dai, J.; Ito, T.; Sun, Li.; Crooks, R. M. *J. Am. Chem. Soc.* **2003**, 125, 13026-13027.

55) Jiang, G.; Harrison, D. J. *Analyst* **2000**, 125, 2176-2179.

56) Lee, H. J.; Goodrich, T. T.; Corn, R. M. *Anal. Chem.* **2001**, 73, 5525-5531.

57) Esch, M. B.; Locascio, L. E.; Tarlov, M. J.; Durst, R. A. *Anal. Chem.* **2001**, 73, 2952-2958.

58) Papra, A.; Bernard, A.; Juncker, D.; Larsen, N. B.; Michel, B.; Delamarche, E. *Langmuir* **2001**, 17, 4090-4095.

59) Meldrum, D. R.; Holl, M. R. *Science* **2002**, 297, 1197-1198.

60) Huber, D. L.; Manginell, R. P.; Samara, M. A.; Kim, B.; Bunker, B. C. *Science* **2003**, 301, 352-354.

61) Sato, K.; Tokeshi, M.; Kimura, H.; Kitamori, T. *Anal. Chem.* **2001**, 73, 1213-1218.

62) Rossier, J. S.; Girault, H. H. *Lab. Chip* **2001**, 1, 153-157.

63) Angenendt, P.; Gloekler, J.; K., Zoltan; L., Hans; C., Dolores J. *Anal. Chem.* **2003**, 75, 4368-4372.

64) Kopp, M. U.; de Mello, A. J., Manz, A. *Science* **1998**, 280, 1046-1048.

65) Jiang, G.; Harrison, D. J. *Analyst* **2000**, 125, 2176-2179.

66) Lagally, E. T.; Simpson, P. C.; Mathies, R. A. *Sens. Actuat. B: Chem.* **2000**, B63, 138-146.

67) Khandurina, J.; McKnight, T. E.; Jacobson, S. C.; Waters, L. C.; Foote, R. S.; Ramsey, J. M. *Anal. Chem.* **2000**, 72, 2995-3000.

68) Breadmore, M. C.; Shrinivasan, S.; Wolfe, K. A.; Power, M. E; Ferrance, J. P.; Hosticka, B.; Norris, P. M.; Landers, J. P. *Electrophoresis* **2002**, 23, 3487-3495.

69) Karlsson, R.; Karlsson, M.; Karlsson, A.; Cans, A.; Bergenholtz, J.; Kerman, B.; Ewing, A. G.; Voinova, M.; Orwar, O. *Langmuir* **2002**, 18, 4186-4190.

70) Cao, H.; Yu, Z.; Wang, J.; Tegenfeldt, J. O.; Austin, R. H.; Chen, E.; Wu, W.; Chou, S. Y. *Appl. Phys. Lett.* **2002**, 81, 174-176.

71) Hibara, A.; Saito, T.; Kim, H.-B.; Tokeshi, M.; Ooi, T.; Nakao, M.; Kitamori, T. *Anal. Chem.* **2002**, 74, 6170-6176.

72) Smirnov, A. I.; Poluektov, O. G. *J. Am. Chem. Soc.* **2003**, 125, 8434-8435.

73) Karlsson, A.; Karlsson, M.; Karlsson, R.; Sott, K.; Lundqvist, A.; Tokarz, M.; Orwar, O. *Anal. Chem.* **2003**, 75, 2529-2537.

74) Moore, A. W., Jr.; Jacobson, S. C.; Ramsey, J. M. *Anal. Chem.* **1995**, 67, 4184-4189.

75) Cheng, J.; Shoffner, M. A.; Mitchelson, K. R.; Kricka, L. J.; Wilding, P. *J. Chromatogr. A* **1996**, 732, 151-158.

76) Effenhauser, C. S.; Bruin, G. J. M.; Paulus, A.; Ehrat, M. *Anal. Chem.* **1997**, 69, 3451-3457.

77) Huang, Z.; Munro, N.; Huhmer, A. F.; Landers, J. P. *Anal. Chem.* **1999**, 71, 5309-5314.

78) Wallenborg, S. R.; Bailey, C. G. *Anal. Chem.* **2000**, 72, 1872-1878.

79) Xue, Q.; Foret, F.; Dunayevskiy, Y. M.; Zavracky, P. M.; McGruer, N. E.; Karger, B. L. *Anal. Chem.* **1997**, 69, 426-430.

80) Ross, P. L.; Davis, P. A.; Belgrader, P. *Anal. Chem.* **1998**, 70, 2067-2073.

81) Lazar, I. M.; Ramsey, R. S.; Sundberg, S.; Ramsey, J. M. *Anal. Chem.* **1999**, 71, 3627-3631.

82) Proskurnin, M. A.; Tokeshi, M.; Slyadnev, M. N.; Kitamori, T. *Anal. Sci.* **2001**, 17, s454-s457.

83) Hisamoto, H.; Horiuchi, T.; Uchiyama, K.; Tokeshi, M.; Hibara, A.; Kitamori, T. *Anal. Chem.* **2001**, 73, 5551-5556.

84) Surmeian, M.; Slyadnev, M. N.; Hisamoto, H.; Hibara, A.; Uchiyama, K.; Kitamori, T. *Anal. Chem.* **2002**, 74, 2014-2020.

85) Furuki, M.; Kameoka, J.; Craighead, H. G.; Isaacson, M. S. *Sens. Actuat. B: Chem.* **2001**, B79, 63-69.

86) Jin-Lee, H.; Goodrich, T. T.; Corn, R. M. *Anal. Chem.* **2001**, 73, 5525-5531.

87) Abrantes, M.; Magone, M. T.; Boyd, L. F.; Schuck, P. *Anal. Chem.* **2001**, 73, 2828-2835.

88) Wang, J.; Pumera, M.; Chatrathi, M. P.; Rodriguez, A.; Spillman, S.; Martin, R. S.; Lunte, S. M. *Electroanal.* **2002**, 14, 1251-1255.

89) Fanguy, J. C.; Henry, C. S. *Analyst*, **2002**, 127, 1021-1023.

90) Martin, R. S.; Ratzlaff, K. L.; Huynh, B. H.; Lunte, S. M. *Anal. Chem.* **2002**, 74, 1136-1143.

91) Osborne, M. A.; Balasubramanian, S.; Furey, W. S.; Klenerman, D. *J. Phys. Chem. B* **1998**, 102, 3160-3167.

92) Weiss, S. *Science* **1999**, 283, 1676-1683.

93) Tachi-iri, Y.; Ishikawa, M.; Hirano, K. *Anal. Chem.* **2000**, 72, 1649-1656.

94) Shortreed, M. R.; Li, H.; Huang, W.; Yeung, E. S. *Anal. Chem.* **2000**, 72, 2879-2885.

95) Ehrfeld, W. Ed. "*Microreaction Technology: Industrial Prospects"* **1999**, Springer Verlag, Berlin.

96) Ehrfeld, W.; Hessel, V.; Löwe, H. Eds. "*Microresctors: New Technology for Modern Chemistry"* **2000**, WILEY-VCH Verlag, Weinheim.

97) Tung, C.; Wu, L.; Zhang, L.; Li, H.; Yi, X.; Song, K.; Xu, M.; Yuan, Z.; Guan, J.; Wang, H.; Ying, Y.; Xu, X. *Pure. Appl. Chem.* **2000**, 72, 2289-2298.

98) Clennan, E. L.; Zhou, W.; Chan, J. *J. Org. Chem.* **2002**, 67, 9368-9378.

99) Lv, Y.; Zhang, Z.; Chen, F. *Analyst*, **2002**, 127, 1176-1179.

100) Peterson, D. S.; Rohr, T.; Svec, F. Fréchet, J. M. J. *Anal. Chem.*, **2002**, 74, 4081-4088.

101) Heo, J.; Thomas, K. J.; Seong, G. H.; Crooks, R. M. *Anal. Chem.* **2003**, 75, 22-26.

102) Hisamoto, H.; Saito, T.; Tokeshi, M.; Hibara A.; Kitamori, T. *Chem. Commun.* **2001**, 24, 2662-2663.

103) Surangalikar, H.; Ouyang, X.; Besser, R. S. *Chem. Eng. J.*, **2003**, 93, 217-224.

104) Daridon, A.; Fascio, V.; Lichtenberg, J.; Wütrich, R.; Langen, H.; Verpoorte, E.; de Rooij, N. F. *Fresen. J. Anal. Chem.*, **2001**, 371, 261–269.

105) Armentrout, D. N.; McLean, D. J.; Long, M. W. *Anal. Chem.* **1979**, 51, 1039-1045.

106) Takahashi, M.; Morita, M.; Niwa, O.; Tabei, H. *J. Electroanal. Chem.* **1992**, 335, 253-263.

107) Wang, J.; Tian, B.; Sahlin, E. *Anal. Chem.* **1999**, 71, 5436-5440.

108) Martin, R. S.; Gawron, A. J.; Lunte, S. M.; Henry, C. S. *Anal. Chem.* **2000**, 72, 3196-3202.

109) Gonon, F. G.; Navarre, F.; Buda, M. J. *Anal. Chem.* **1984**, 56, 573-575.

110) Saraceno, R. A.; Ewing, A. G. *Anal. Chem.* **1988**, 60, 2016-2020.

111) Niwa, O.; Morita, M.; Tabei, H. *Electroanal.* **1994**, 6, 237-243.

112) Rossier, J. S.; Ferrigno, R.; Girault, H. H. *J. Electroanal. Chem.* **2000**, 492, 15-22.

113) Manica, D. R.; Ewing, A. G. *Electrophoresis* **2002**, 23, 3735-3743.

114) Rossier, J. S.; Roberts, M. A.; Ferrigno, R.; Girault, H. H. *Anal. Chem.* **1999**, 71, 4294-4299.

115) Engblom, S. O.; Cope, D. K.; Tallman, D. E. *J. Electroanal. Chem.* **1996**, 406, 23-31.

116) Clark, R. A.; Ewing, A. G. *Anal. Chem.* **1998**, 70, 1119-1125.

117) Kshyap, R.; Gratzl, M. *Anal. Chem.* **1998**, 70, 1468-1476.

118) Cahill, P. S.; Wightman, R. M. *Anal. Chem.* **1995**, 67, 2599-2605.

119) Gavin, P. F.; Ewing, A. G. *J. Am. Chem. Soc.* **1996**, 118, 8932-8936.

120) Bratten, C. D. T.; Cobbold, P. H.; Cooper, J. M. *Anal. Chem.* **1997**, 69, 253-258.

121) Paras, C. D.; Kennedy, R. T. *Electroanal.* **1997**, 9, 203-208.

122) Nakatani, K.; Uchida, T.; Misawa, H.; Kitamura, N.; Masuhara, H. *J. Phys. Chem.* **1993**, 97 5197-5199.

123) Nakatani, K.; Uchida, T. Misawa H.; Kitamra, N.; Masuhara, H. *J. Electroanal. Chem.* **1994**, 367, 109-114.

124) Nakatani, K.; Uchida,T.; Kitamura, N., Masuhara, H. *J. Electroanal. Chem.* **1994**, 375, 383-386.

125) Mandler, D.; Bard, A. J. *Langmuir* **1990**, 6, 1489-1494.

126) Bard, A. J.; Fan, F. R. F.; Pierce, D. T.; Unwin, P. R.; Wipf, D. O.; Zhou, F. *Science*, **1991**, 254, 68-74.

127) Sugimura, H.; Shimo, N.; Kitamura, N.; Masuhara, H.; Itaya, K. *J. Electroanal. Chem.* **1993**, 346, 147-160.

128) Sugimura, H.; Uchida, T.; Kitamura, N.; Shimo, N.; Masuhara, H. *J. Electroanal. Chem.* **1993**, 361, 57-63.

129) Harrington, M. S.; Anderson, L. B. *Anal. Chem.* **1990**, 62, 546-550.

130) Tabei, H.; Morita, M.; Niwa, O.; Horiuchi, T. *J. Electroanal. Chem.* **1992**, 334, 25-33.

131) Niwa, O.; Tabei, H. *Anal. Chem.* **1994**, 66, 285-289.

132) Takahashi, M.; Morita, M.; Niwa, O.; Tabei, H. *J. Electroanal. Chem.* **1992**, 335, 253-63.

133) Tabei, H.; Takahashi, M.; Hoshino, S.; Niwa, O.; Horiuchi, T. *Anal. Chem.* **1994**, 66, 3500-3502.

134) Bjorefors, F.; Strandman, C.; Nyholm, L. *Electroanal.* **2000**, 12, 255-261.

135) Puppels, G. J.; de Mul, F. F.; Otto, C.; Greve, J.; Robert-Nicoud, M.; Arndt-Jovin, D. J.; Jovin, T. M. *Nature* **1990**, 347, 301-303.

136) Feofanov, A. V.; Grichine, A. I.; Shitova, L. A.; Karmakova, T. A.; Yakubovskaya, R. I.; Egret-Charlier, M.; Vigny, P. *Biophys. J.* **2000**, 78, 499-512.

137) Kogi, O.; Kim, H.-B.; Kitamura, N. *Analyst* **2002**, 127, 967-971.

138) Dittrich, P. S.; Schwille, P. *Anal. Chem.* **2003**, 75, 5767-5774.

139) Cotlet, M.; Gronheid, R.; Habuchi, S.; Stefan, A.; Barbafina, A.; Muellen, K.; Hofkens, J.; De Schryver, F. C. *J. Am. Chem. Soc.* **2003**, 125, 13609-13617.

140) Haw; L., G.; Karnchanaphanurach, P.; Louie, T.; Rech, I.; Cova, S.; Xun, L.; Xie,

X. S. *Science* **2003**, 302, 262-266.

141) Holman, M. W.; Liu, R.; Adams, D. M. *J. Am. Chem. Soc.* **2003**, 125, 12649-12654.

142) Yao, H.; Inoue, Y.; Ikeda, H.; Nakatani, K.; Kim, H.-B.; Kitamura, N. *J. Phys. Chem.* **1996**, 100, 1494-1497.

143) Chiu, D. T.; Hsiao, A.; Gaggar, A.; Garza-Lopez, R. A.; Orwar, O.; Zare, R. N. *Anal. Chem.* **1997**, 69, 1801-1807.

144) Ajito, K. *Appl. Spectrosc.* **1998**, 52, 339-342.

145) Misawa, H.; Koshioka, M.; Sasaki, K.; Kitamura, N.; Masuhara, H. *Chem. Lett.* **1990**, 1479-1482.

146) Funakura, S.; Nakatani, K.; Misawa, H.; Kitamura, N.; Masuhara, H. *J. Phys. Chem.* **1994**, 98, 3073-3075.

147) Kim, H.-B.; Hayashi, M.; Nakatani, K.; Kitamura, N.; Sasaki, K.; Hotta, J. I.; Masuhara, H. *Anal. Chem.* **1996**, 68, 409-414.

148) Perkins, T. T.; Quake, S. R.; Smith, D. E.; Chu, S. *Science* **1994**, 264, 822-826.

149) Kim, H.-B.; Yoshida S.; Miura, A.; Kitamura, N. *Chem. Lett.* **1996**, 923-924.

150) Kim, H.-B.; Yoshida, S.; Miura A.; Kitamura, N. *Anal. Chem.* **1998**, 70, 111-116.

151) Kim, H.-B.; Habuchi, S.; Hayashi M.; Kitamura, N. *Anal. Chem.* **1998**, 70, 105-110.

152) Habuchi, S.; Kim H.-B.; Kitamura. N. *Anal. Chem*. **2001**, 73, 366-372.

153) Nakatani, K.; Chikama, K.; Kim H.-B.; Kitamura N. *Chem. Lett*. **1994**, 793-796.

154) Nakatani, K.; Chikama, K.; Kim, H.-B.; Kitamura, N. *Chem. Phys. Lett.* **1995,** 237, 133-136.

155) Zhan W.; Alvarez J.; Crooks R. M. *J. Am. Chem. Soc.* **2002**, 124, 13265-13270.

156) Zhan W.; Alvarez J.; Crooks R. M. *Anal. Chem.* **2003**, 75, 313-318.

157) Zhonghui, H. F.; Harrison, D. J. *Anal. Chem.* **1994**, 66, 177-184.

158) Roberts, M. A.; Rossier, J. S.; Bercier, P. Girault, H. H. *Anal. Chem.* **1997**, 69, 2035 -2042.

159) Pugmire, D. L.; Waddell, E. A.; Haasch, R.; Tarlov, M. J.; Locascio, L. E. *Anal. Chem.* **2002**, 74, 871-878.

160) Locascio, L. E.; Perso, C. E.; Lee, C. S. *J. Chromatogr. A* **1999**, 857, 275-284.

161) Xu, J.; Locascio, L.; Gaitan, M.; Lee, C. S. *Anal. Chem.* **2000**, 72, 1930-1933.

162) Chen, Y.; Chen, S. *Electrophoresis* **2000**, 21, 165-170.

163) Weigl, B. H.; Yager, P. *Science* **1999**, 283, 346-347.

Chapter 2.

Fabrication and Characterization of Polymer Microchannel Chips

2.1 Introduction

The principal aim of the study is to fabricate polymer microchannel chips and to elucidate the characteristics of the chemical reaction processes in the channel. In order to pursue the present study, it needs the establishments of the fabrication method of polymer microchannel chips and characterizations of the fabricated chips. As described in Chapter 1, an imprinting method is a very powerful means to fabricate polymer microchannel chips and, microspectroscopic technique is very suitable for following the reaction processes in the channel. Therefore, a combination of a microchannel solution-flow system with microspectroscopy is the important basis to perform the present study.

On the basis of these concepts, fabrication and characterization of polymer microchannel chips were performed. A glass template for imprinting was fabricated by photolithography and etching techniques and, was applied to fabricate polymer microchannel chips by an imprinting method. The structures of the fabricated channel chip were evaluated by means of a scanning electron microscope (SEM), and the channel chips were then combined with a pressure-driven flow system by using a mechanical syringe pump.

In order to observe phenomena proceeding in a microchannel, the channel chip was set under a microscope equipped with a CCD camera and microspectroscopy measurements were conducted. In the present study, the mixing processes of two solutions in the channel were studied on the basis of space-resolved microspectroscopy

to check the performance of the channel flow - microspectroscopy system. An aqueous alkaline solution and an aqueous acidic solution containing a pH-indicator were introduced independently to the microchannel chip with the same flow velocity. The flow characteristic in the microchannel was then observed by using a CCD camera, and the pH-profile in the channel chip was studied by absorption microspectroscopy. As an another approach, aqueous fluorescence dye solutions with and without a fluorescence quencher are injected simultaneously into the channel chip, and the successive diffusion processes of the quencher in the microchannel were followed by using dynamic fluorescence microspectroscopy. On the basis of these experiments, solution-flow characteristics in the microchannel were discussed.

2.2 Experimental

2.2.1 Materials, Chemicals, and Sample Preparations

A microscope slide glass (Matsunami Glass) was used as a material for a template. A polystyrol substrate with the thickness of 1.7 mm (Tamiya Co., Ltd.) was used as a chip material throughout the study. A positive-type photoresist (OFPR800, Tokyo Ohka Kogyo Co., Ltd.), a developer (NMD-3, Tokyo Ohka Kogyo Co., Ltd.), and a stripper (acetone) were used for photolithography. An etching solution (HF/NH_4F aq, hydrofluoric acid and ammonium fluoride, Wako Pure Chemical Industrial Co., Ltd., GR grade) for an SiO_2 substrate was an HF/40%-NH_4F aqueous solution (1/6, v/v). Water was used after deionization and distillation (GSR-200, Advantec Toyo Co., Ltd.). Sulfuric acid (98%), potassium permanganate, hydrogen peroxide, and 1,1,1,3,3,3-hexamethyldisilazane (HMDS, Wako Pure Chemical Industrial Co., Ltd.,

GR grade) were used for cleaning and surface improvement of a glass substrate.

For microspectroscopic experiments, sample solutions were prepared as follows. Sodium hydroxide (Kanto Chemical Co., Inc. S Grade) and hydroxy naphthol blue (HNB, Dojindo Chemical Laboratory Co., Ltd., GR Grade) as a pH indicator were used for absorption spectroscopy measurements. HNB was used without further purification. The pH of an aqueous sodium hydroxide solution was adjusted to 11. The pH of an aqueous HNB solution (10 mM) was set 4.5. On the other hand, water-soluble uranine (Wako Pure Chemical Industrial Ltd., GR grade) as a derivative of fluorescein was used as a fluorescent dye for dynamic fluorescence spectroscopy. The structural formulas of HNB and uranine are shown in Figure 2-1. Triethanolamine (TEA, Wako Pure Chemical Industrial Ltd., GR grade) was used as a fluorescence quencher of uranin. A phosphate buffer (pH 9.18, Kanto Chemical Co. Inc., S Grade) was used as a medium. Uranin solutions (1.0×10^{-4} M) with and without TEA (0.8 M) were used as samples.

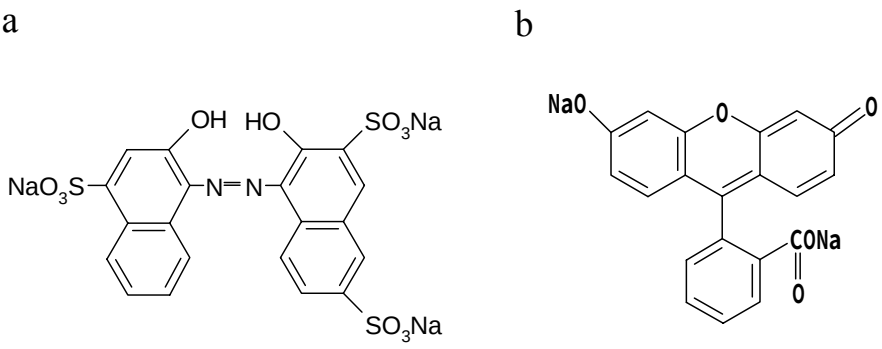

Figure 2-1 The structural formulas of HNB (a) and uranine (b).

2.2.2 *Fabrication and Structures of Polymer Microchannel Chips*

Polymer microchannel chips can be fabricated by two steps. The first step is fabrication of a template and the second step is imprinting of the template onto a polymer substrate and successive bonding with a cover substrate. A glass substrate as a template was fabricated by simple photolithography techniques and chemical etching. Commercially available polystyrol substrates were chosen as a channel substrate, since the substrate was very cheap, transparent in the visible region, and showed a moderate softening temperature (T_g ~108 ºC).[1]

Glass Template

A glass substrate was cleaned in concentrated sulfuric acid containing a small amount of potassium permanganate, and successive rinsing with pure water. The glass substrate was then treated with a concentrated sulfuric acid/hydrogen peroxide solution (1/1, v/v) to modify the surface to hydrophilic. Hydrophobic treatments of the glass substrate were carried out by immersing the substrate in a 2~3% HMDS/toluene solution for 30 min. By the HMDS treatment of SiO_2 (illustrated in Figure 2-2), a photoresist can be coated tightly on the substrate.[2] Particularly, the HMDS treatment can avoid peeling of a resist layer during development and side-etching of the glass substrate.

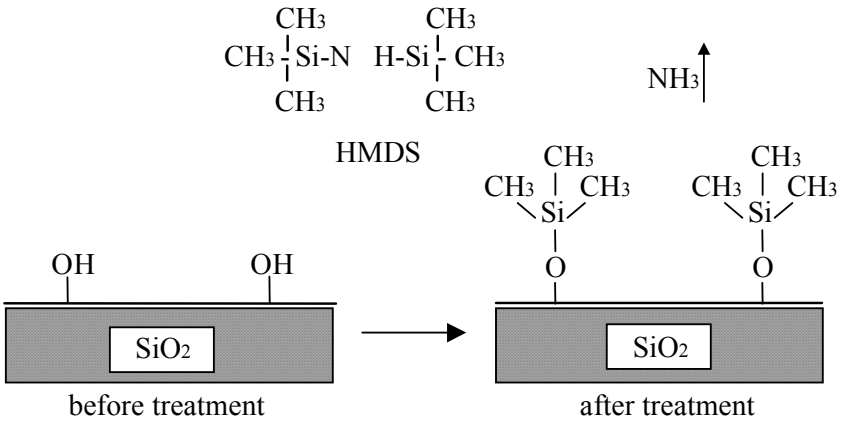

Figure 2-2 Illustration of HMDS treatment of a glass surface.

After the pretreatment of a glass substrate as mentioned above, a photoresist (OFPR800) was spin-coated on the glass substrate at 500 rpm for 5 s and at 3000 rpm for 20 s by using a photoresist spinner (Kyowariken Co., Ltd.). The substrate was pre-baked on a hot plate at 110 ºC for 90 s to prevent peeling of the photoresist layer during development. The substrate was then exposed to a 300 W tungsten lamp for 90 s through a photomask, whose structure was printed on a transparency film. The structural layout of the mask was drawn by using a standard drawing software package (Microgrfx Inc., Windows Draw, or Microsoft Inc., PowerPoint 97) and printed on the film by a 2400 dpi printer. After the resist layer was developed (NMD-3) and rinsed with water, post-bake of the layer was conducted for 5 min at 120 ºC on a hot plate. The glass substrate was then immersed in an etching solution (HF/NH_4F aq) at 30 ºC for 20 min under stirring. After thorough rinsing of the substrate with distilled water, the photoresist layer was removed by a stripper. This embossed structure on the glass plate was used to imprint the image onto a polystyrol substrate. The overall photolithographic processes are illustrated in Figure 2-3.

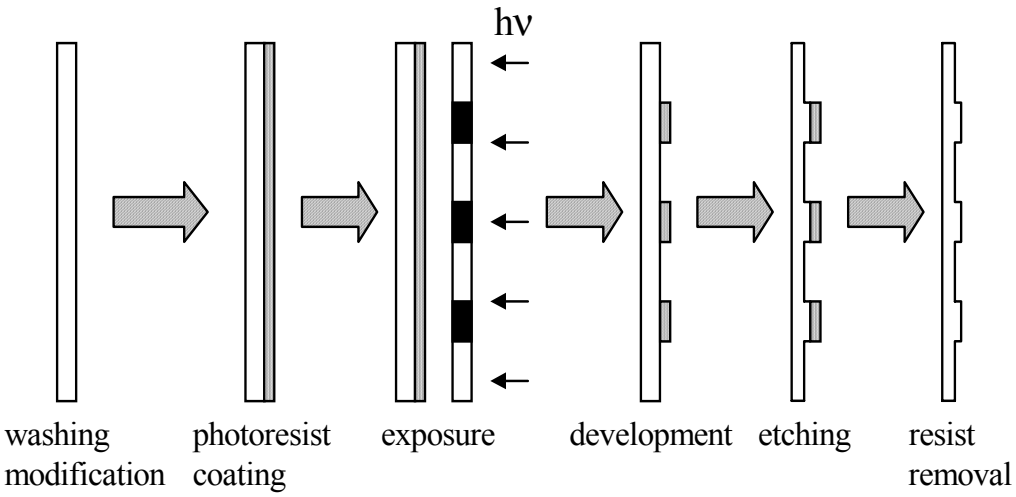

Figure 2-3 The photolithographic processes for a glass substrate.

Imprinting Method

Microchannel chips were fabricated on a polystyrol substrate according to an imprinting method reported by Martynova et al.[3] with some modifications. A polystyrol substrate and the structured-glass template were fastened tightly with two flat glass-plates and heated at 110 ºC for 25 min in a temperature controlled oven (cf. Figure 2-4 (a)).

As a fluidic device, the polymer substrate was covered and bonded with a flat polystyrol substrate by clamping both substrates between two flat glass-plates and heating at 110 ºC for 18 min (cf. Figure 2-4 (b)). Prior to bonding, two holes (ϕ = 0.5 mm) for the drain were drilled on the cover polymer as illustrated in Figure 2-5. On the other hand, for tubing the chip with a syringe pump, two wide and deep channels were fabricated at the inlet positions of the channel by a wire (ϕ = 0.3 mm) imprinting method.

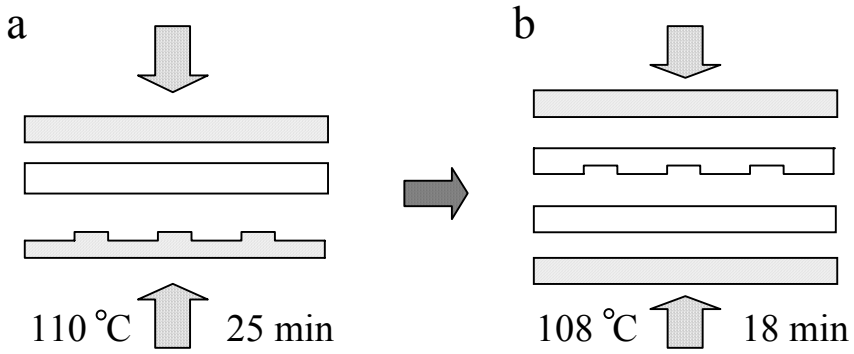

Figure 2-4 Illustration of the fabrication processes of a channel chip by an imprinting method: transfer printing of a template onto a polymer substrate (a) and bonding of the channel substrate with a cover plate (b).

Design of the Polymer Microchannel Chip

A schematic drawing of the microchannel chip design for the present purpose of the study is shown in Figure 2-5. The channel pattern was designed as a double Y style to allow two solutions being introduced from the two channel inlets and confluent in the microchannel.[4,5] The channel width was set 300 μm.

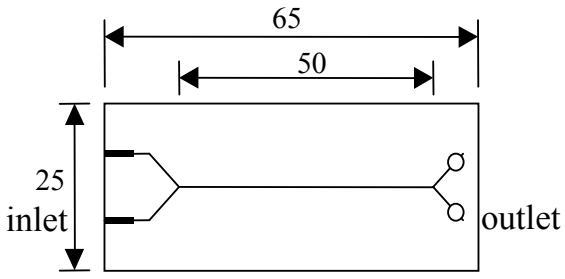

Figure 2-5 Schematic drawing of the microchannel design. The size of the microchannel structures are shown in millimeters. The channel width was set 300 μm.

2.2.3 Experimental Setup

Solution-Flow and Microspectroscopy Systems

A solution-flow system used in this study is shown in Figure 2-6. Two syringes (Hamilton Gastight, TLL-standard type syringes, 250 μl volume), each being filled with a sample solution, were equipped with a programmable dual-syringe pump (Harvard, Model 44). Each syringe was connected with the microchannel *via* a fused silica capillary tube (100 μm i.d.; 200 μm o.d., GL Sciences Co., Ltd.). Connection between the tube and the hole on the channel chip was made by using an epoxy resin.

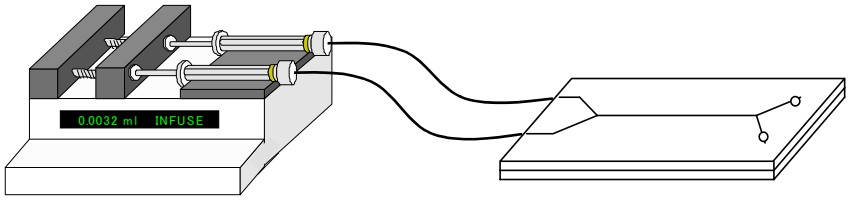

Figure 2-6 Schematic drawing of the microchannel - solution flow system.

Absorption Microspectroscopy System

A block diagram of the absorption microspectroscopy system used in this study is illustrated in Figure 2-7. For absorption spectroscopy, a Xe light beam (C4264, Hamamatsu Photonics Co.) being passed through a pinhole (ϕ = 100 μm) was introduced to an optical microscope (Optiphoto II, Nikon Co.) and irradiated onto a microchannel chip. The diameter and quality of the probe beam are very important to perform precise and accurate absorption microspectroscopy.[6] In the present experiments, the paraxial ray of a microscope objective was used as a quasi-parallel probe beam, and

its diameter was adjusted to ~10 μm. The beam being passed through a sample solution in the channel chip (intensity, *I*) and a condenser lens was reflected by a half mirror set under the microscope stage and led to a multichannel photodetector (PMA-11, Hamamatsu Photonics Co.) via an optical fiber to record an absorption spectrum. The exposure time for the multichannel photodetector is set 250 ms to conduct absorption measurements. The incident light intensity of the Xe beam (I_0) was determined under analogous optical conditions for a solution without a solute.[7,8] Also, the flow characteristics of the dye solution in the microchannel was monitored by a CCD camera (KP-C557, Hitachi Co.) equipped to the microscope. The relevant images were accumulated by a video recorder (SLV-F11, Sony Co.) and then printed by a video printer (CP710, Mitsubishi Co.).

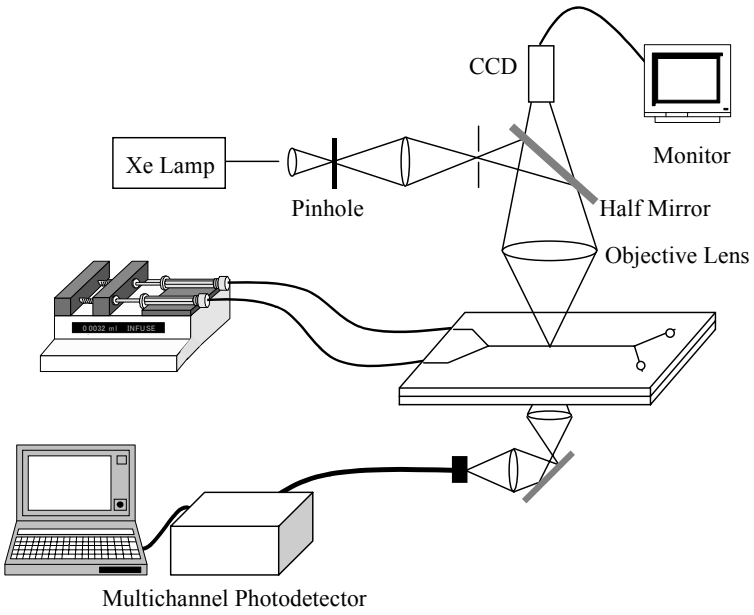

Figure 2-7 A block diagram of the absorption microspectroscopy system.

Dynamic Fluorescence Spectroscopy System

A block diagram of a time-resolved fluorescence microspectroscopy system used in the present study is shown in Figure 2-8. A mode-locked synchronous titanium sapphire laser (Mira900F, Pulse Width ~150 fs, Coherent Co.) pumped by a semiconductor laser (Verdi, Coherent Co.) was used as an oscillator. After the oscillator-pulse intensity was amplified by a regeneration amplification system, the wavelength of the laser beam was adjusted to 500 nm (pulse width 150 fs) by an optical parametric amplifier (OPA).[9-11] The laser beam was used as excitation light. The excitation beam was introduced to a microscope by the similar methods with those in absorption spectroscopy mentioned before and was focused onto the microchannel chip through an objective lens. The spot size of the excitation beam was ~10 μm in diameter. The fluorescence from a sample solution in the channel was passed through a cut filter (λ < 520 nm, Toshiba Co.) and detected with a cooling-type multichannel photomultiplier (R3809U-50, Hamamatsu Photonics Co.) - polychromater system. All measurements were conducted by using a single photon counting system (SPC-300, Edinburgh Instruments Co., Ltd.).

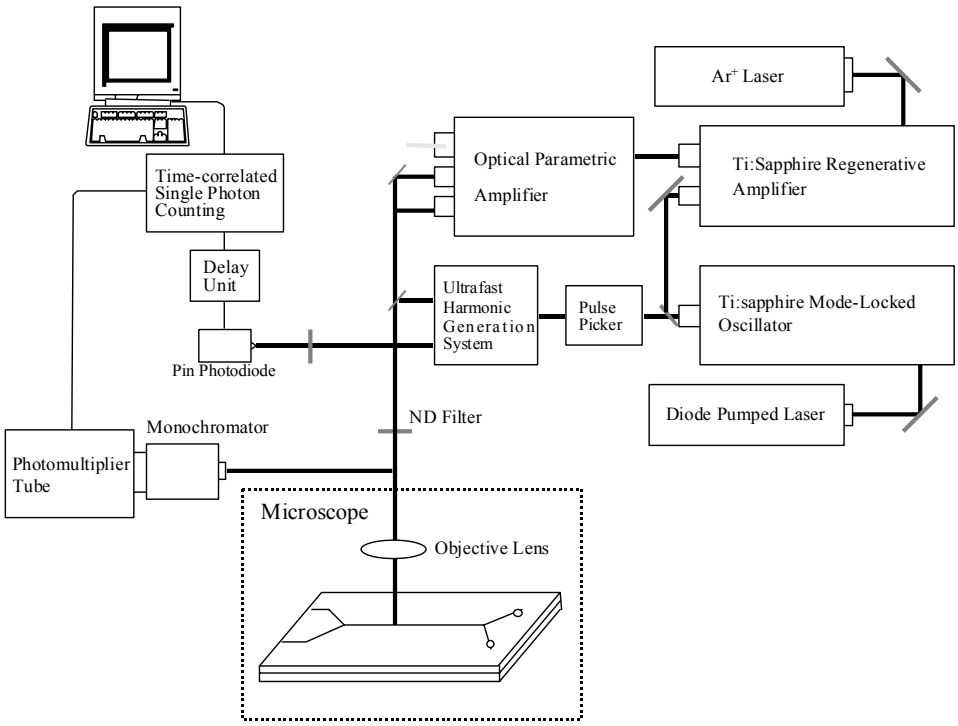

Figure 2-8 A block diagram of a time-resolved fluorescence microspectroscopy system.

2.3 Results and Discussions

2.3.1 Evaluation of the Performances of a Polymer Microchannel Chip and a Solution-Flow System

A scanning electron microscope image of the polystyrol substrate shown in Figure 2-9 indicates that the microchannel is fabricated successfully on the substrate: 180 μm width and 12 μm depth. Although the edge of the channel was not fabricated sharply and somewhat structurally rough, the polymer microchannel chip fabricated by the simple photolithography and imprinting methods was potential enough for conducting the present experiments as described later.

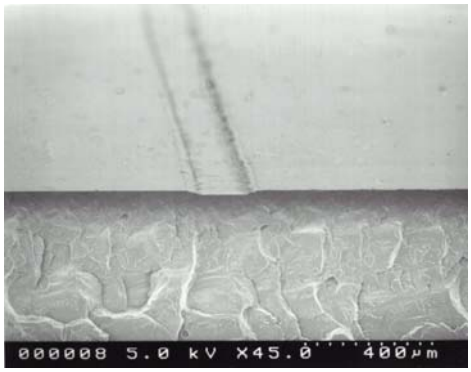

Figure 2-9 Scanning electron microscope (SEM) image of a polystyrol-based microchannel chip (side view).

Connection between the channel chip and the capillary tube was sufficiently robust, and solution leak was not confirmed during fluid-flow. However, boding between the channel substrate and the channel cover was not strong enough, so that the linear flow velocity applicable to the fabricated channel chip was limited below 3 cm s^{-1}.

2.3.2 Absorption Microspectroscopy

HNB and NaOH solutions were introduced separately to the channel chip with the same flow velocity: 2.5 cm s^{-1}. A photograph observed at 0.5 cm (in the downstream side) from the junction of the microchannel is shown schematically in Figure 2-10 (a). The flow characteristics in a microchannel, operated by pressure-driven flow, are described by low Reynolds-number (Re) flow as described in Chapter 1: laminar flow.[12-15] Under the present experimental conditions, Re was 0.3, so that laminar flow was observed certainly as illustrated in Figure 2-10.

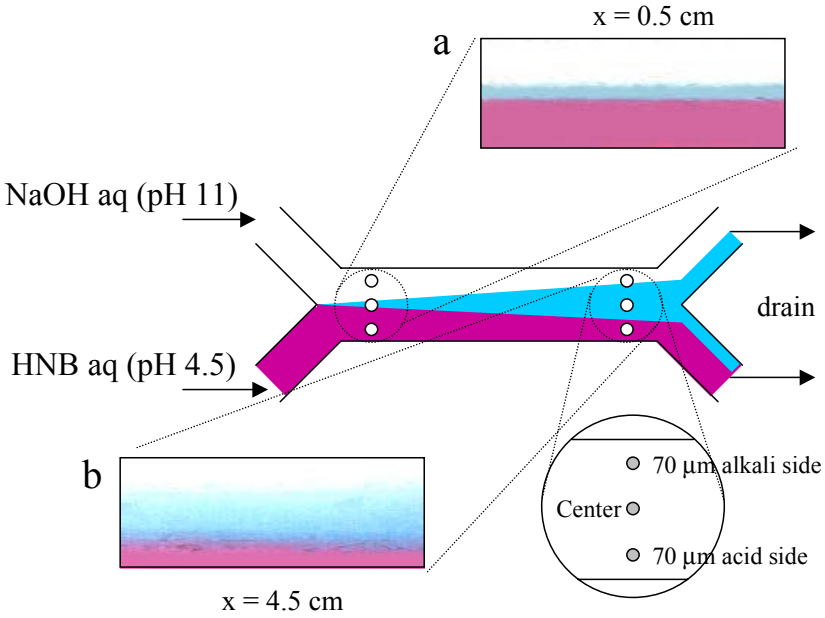

Figure 2-10 The flow characteristics in the microchannel observed at 0.5 (a) and 4.5 cm (b) (to the downstream-side) from the junction.

On the other hand, the photograph observed at 4.5 cm (in the downstream-side) from the junction (x) is included in Figure 2-10 (b). HNB shows a blue color in an alkali solution, while that exhibits magenta in an acid solution. Although the photographs in Figure 2-10 demonstrate that the two solutions run parallel in the microchannel, the width of the blue layer showing a high pH region becomes wider in the downstream side from the junction. This indicates that two solutions are mixed along with solution-flow and neutralization of the two water layers proceeds in the channel chip. In order to confirm this quantitatively, absorption spectroscopy of the solution layer in the microchannel was conducted. Pure water was introduced to the channel and the transmitted light spectrum was measured as a reference (I_0) for absorption measurements. The position-dependence of the absorption spectrum of HNB in the

channel chip was then examined. Corresponding to the photographs in Figure 2-10, absorption spectroscopy of the solution layer was carried out at x = 0.5 and 4.5 (in the downstream-side) from the junction, with the monitoring spot being varied 70 μm from the alkaline to the acidic side, including the center of the two layers. The absorption spectra thus obtained are shown in Figure 2-11.

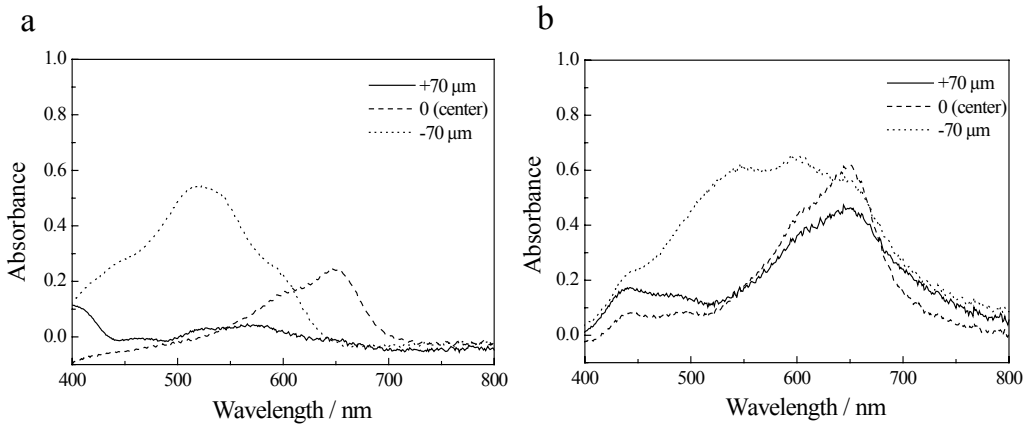

Figure 2-11 Absorption spectra of HNB (a) at x = 0.5 cm and (b) 4.5 cm in the downstream-side from the junction in the microchannel. The plus/minus 70 μm shown in the figures represent the data monitored in the alkaline layer at the 70 μm separated from the center of the two layers and those in the acidic layer, respectively. 0 (center) represents the data monitored at the center of the two solutions.

At x = 0.5 cm, the absorption spectra observed in the alkaline and acidic phases exhibited the maximum at around 520 nm (magenta) and almost no absorption (colorless), respectively, while that at the interface showed the peak at around 650 nm (blue). The results agree with the colors in the photographs in Figure 2-10 (a). This indicates clearly that the neutralization reaction proceeds only in the channel center, because the time after mixing at the junction is too short to mix the two layers (0.2 s).

At x = 4.5 cm, on the other hand, the contribution of the blue color to the overall spectrum is dominant irrespective of the position as shown in Figure 2-11 (b). It is concluded, therefore, that neutralization proceeds along with solution-flow and, at 1.6 seconds after mixing of the two solutions in the microchannel, the two solutions are almost mixed within the 70 μm-width solution layer in each layer. It was confirmed that the channel flow system was operated correctly, and laminar flow characteristic in a microchannel was visualized successfully. Furthermore, it was shown that absorption spectroscopy could be conducted by using a transparent polymer substrate chip.

2.3.3 Dynamic Fluorescence Microspectroscopy

Aqueous uranine and uranine-TEA solutions were introduced to the microchannel chip with the same flow velocity: 0.7 cm s^{-1}. The two solutions run with laminar flow in the microchannel, and mixed by molecular diffusion to the vertical direction of flow, as schematically shown in Figure 2-12. It is expected that the fluorescence lifetime of uranine decreases along with solution-flow in the microchannel, owing to diffusion of TEA as a quencher for the excited state of uranine. Therefore, space-resolved fluorescence lifetime measurements were conducted by using the microchannel. The monitoring position in the uranine-TEA phases was set at x = 4.5 cm in the down-stream side from the junction. The position at 100 μm separated from the center was monitored in addition to the center of the two solutions.

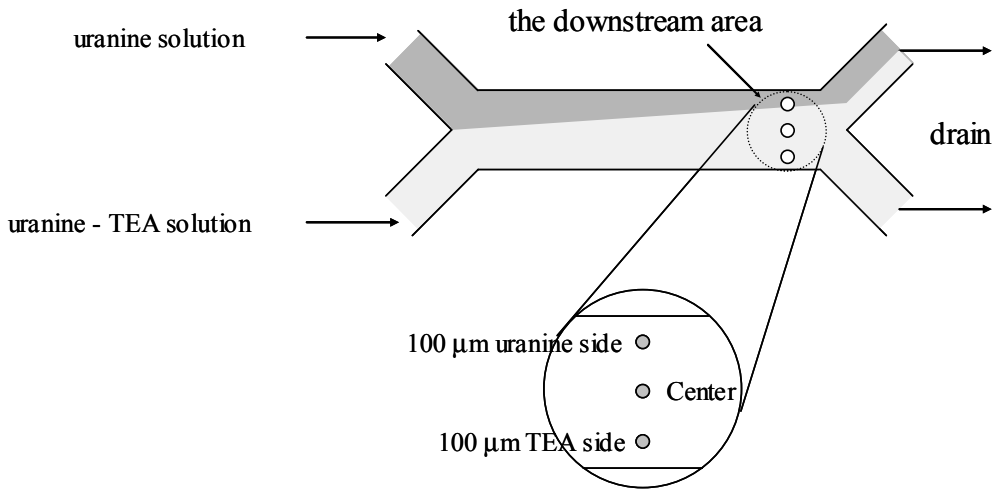

Figure 2-12 Schematic drawing of the experiments.

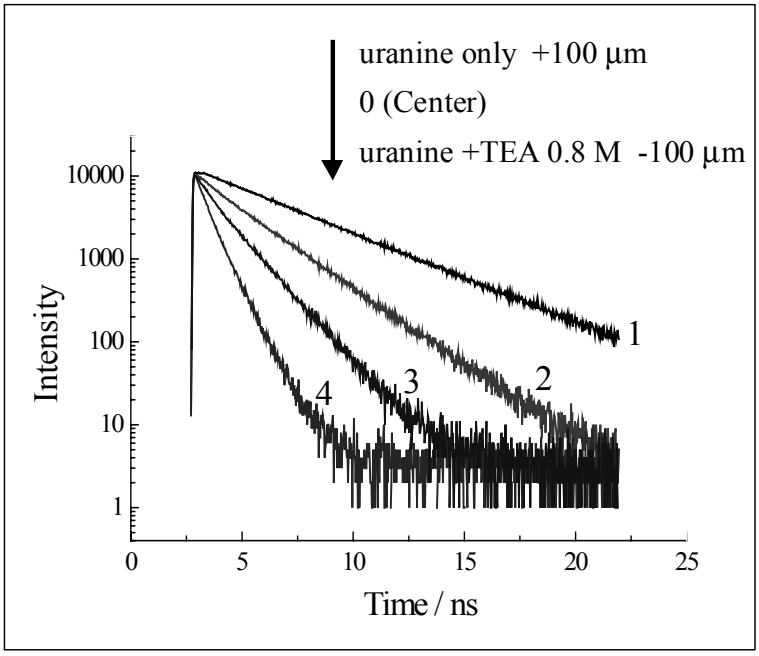

Figure 2-13 The fluorescence decay curves of uranine observed at several positions in the microchannel.

The fluorescence decay curve observed at each position is summarized in Figure 2-13. The fluorescence decay curve shown by ***1*** was measured for the aqueous uranine solution in the microchannel. The fluorescence lifetime was determined to be 4 ns, which was in good agreement with that by bulk measurements. Therefore, it was confirmed that the fluorescence lifetime measurements could be conducted precisely and reliably even by using a microchannel chip. On the other hand, the decay curves shown by ***2*** - ***4*** (separated from +100, 0, -100 μm from the center, respectively) are those measured by flowing both uranine and uranine-TEA solutions in the microchannel. It is understood from the results that the fluorescence lifetime of uranine decreases on going from the uranine layer to the uranine-TEA layer. The change in the fluorescence lifetime is explained by mixing of the two solutions in the downstream-side from the junction of the microchannel, and TEA molecules diffuse to the uranine side (6.4 s after mixing) along with solution-flow. It was confirmed that fluorescence measurements could be conducted even by using a microchannel chip fabricated by the imprinting method, similar to absorption spectrum measurements.

2.4 Conclusion

A new and novel fabrication method for polymer microchannel chips was demonstrated on the basis of a simple photolithographical technique and an imprinting method. The structure of the channel chip fabricated was evaluated by a SEM image of the channel cross section. Although the edge of the channel was not fabricated sharply and somewhat structurally rough, it was confirmed that the channel chip was potential enough for the present experiments. The channel pattern was designed as a double Y style and used in the present study as described in Section 2-3. So far, injection of a

sample solution into a microchannel has been conducted usually by electroosmotic flow or electrophoresis. However, mechanical pump flow was used in the present study by using a syringe pump, which was shown to be capable of controlling the flow velocity very accurately. The solution-flow system developed in the present study was shown to control the flow velocity upto about 2.5 cm s^{-1} without leakage of a solution. Also, a microspectroscopy system combined with the channel flow system was developed. Mixing processes of solutions in the microchannel were studied as an experimental check of the performances of the channel flow-spectroscopy system. It was confirmed that absorption and fluorescence measurements could be done correctly even by using a fabricated polymer microchannel. Therefore, an application of the system to versatile experiments is promising, as the results are described in the following chapters.

2.5 References

1) Rieger, J. *J. Therm. Anal.* **1996**, 46, 965-972.
2) Ojima, S.; Jizaimaru, T.; Omae, S.; Ohmi, T. *J. Electrochem. Soc.* **1997**, 144, 4005-4018.
3) Martynova, L.; Locascio, L. E.; Gaitan, M.; Kramer, G. W.; Christensen, R. G.; MacCrehan, W. A. *Anal. Chem.* **1997**, 69, 4783-4789.
4) Tokeshi, M.; Minagawa, T.; Kitamori, T. *Anal. Chem.* **2000**, 72, 1711-1714.
5) Tokeshi, M.; Minagawa, T.; Kitamori, T. *J. Chromatgr. A* **2000**, 894, 19-23.
6) Kim, H.-B.; Yoshida, S.; Kitamura, N. *Anal. Chem.* **1998**, 70, 51-57.
7) Kitamura, N.; Hayashi, M.; Kim, H.-B.; Nakatani, K. *Anal. Sci.* **1996**, 12, 49-54.
8) Nakatani, K.; Suzuki, T.; Shitara, S.; Kitamura, N. *Langmuir* **1998**, 14, 2286-2290.
9) Ishizaka, S.; Nakatani, K.; Habuchi, S.; Kitamura, N. *Anal. Chem.* **1999**, 71,

419-426.

10) Kim, H.-B.; Habuchi, S.; Kitamura, N. *Anal. Chem.* **1999**, 71, 842-848.

11) Ishizaka, S.; Habuchi, S.; Kim, H.-B.; Kitamura, N. *Anal. Chem.* **1999**, 71, 3382-3389.

12) Kamholz, A. E.; Yager, P. *Biophys. J.* **2001**, 80, 155-160.

13) Thorsen, T.; Roberts, R. W.; Arnold, F. H.; Quake, S. R. *Phys. Rev. Lett.* **2001**, 86, 4163-4166.

14) Costin, C. D.; Synovec, R. E. *Anal. Chem.* **2002**, 74, 4558-4565.

15) Kam, L.; Boxer, S. G. *Langmuir* **2003**, 19, 1624-1631.

Chapter 3.

Spatially-Resolved Fluorescence Spectroscopic Study on Liquid/Liquid Extraction Processes in Polymer Microchannel Chips

3.1 Introduction

As described in Chapter 2, *in-situ* space-resolved microspectroscopy is very powerful means to elucidate solution mixing processes in a microchannel chip. Under laminar flow conditions in a microchannel, two miscible solutions run parallel without turbulence as demonstrated in Chapter 2. On the basis of laminar flow, immiscible oil/water solution-flow in a microchannel is also expected to form the stable oil/water interface without mutual mixing as in the case for water/water solution-flow.

While various chemical reactions and physicochemical processes can be studied by using microsystems, a study on oil/water interfacial mass transfer between two immiscible fluids is very important. Namely, although liquid/liquid extraction is used widely in both preparative and analytical chemistry,[1-4] difficulties arise in the development of automated or continuously-operated extraction devices due to conflicting requirements concerning efficient inter-phase transport of masses and phase separation. When a microchannel chip is used in liquid/liquid extraction experiments, both efficient extraction and clear phase separation of the two fluids will be achieved if rapid inter-phase mass transfer of a solute takes place during fluid flow. Therefore, studies along this line are very important to develop automated- and continuously-operated liquid/liquid extraction devices.

In order to realize such a device, nonetheless, since flow characteristics in a microchannel is governed by several factors such as a channel dimension, channel

geometries, and a flow velocity, a liquid/liquid extraction efficiency should be studied as a function of these factors. Also, an *in-situ* study on mass-transfer processes across the liquid/liquid interface in a microchannel is needed to optimize the necessary conditions to realize an ideal liquid/liquid extraction microdevice. Therefore, a spatially-resolved spectroscopic study on the liquid/liquid extraction processes in microchannel chips was explored.

In the present study, liquid/liquid extraction of an Al^{3+}-DHAB chelate (DHAB = 2,2'-dihydroxyazobenzen) from water to 1-butanol (BuOH) was studied by using several types of a microchip. In the section 3.3.1, fluorescence spectroscopic analyses of the liquid/liquid extraction processes in a microchannel were conducted by using polystyrol-based microchips fabricated by the same method with that described in Chapter 2. For the purpose, two immiscible fluids were brought together into the channel by pressure driven flow at the same flow velocity. Extraction of Al^{3+}-DHAB from water to BuOH was then studied as a fluorescence intensity profile of the complex in the BuOH phase along the flow direction (x-axis) as well as along the channel width direction (y-axis). A numerical simulation of the mass-transfer processes of Al^{3+}-DHAB across the water/BuOH interface in the channel was also performed and the results were compared with the experimental data.

In the section 3.3.2, the performances of the polymer channel - liquid/liquid extraction system were discussed by comparing those by a similar-structured silicon micromachined channel chip. So far, most of the related studies have been conducted by using a silicon or glass channel chip. The performances of polymer microchannel chips are worth to be compared with those of a silicon or glass channel chip. Therefore, both silicon and polystyrol channel chips having the same channel geometry were fabricated,

and their performances were compared on the basis of a spatially-resolved fluorescence microscopic study on the liquid/liquid extraction processes in each channel chip. Characteristic features of the performances of both polymer and silicon channel chips are discussed.

In the section 3.3.3, a solvent dependence of the liquid/liquid extraction dynamics in a silicon channel chip was described. Tributylphosphate (TBP) was used in stead of using BuOH as an oil phase in liquid/liquid extraction. The viscosity of TBP is higher than that of BuOH, so that this might influence extraction dynamics. The characteristics of the water/TBP extraction processes of Al^{3+}-DHAB in a silicon channel chip were discussed on the basis of the results by fluorescence spectroscopy, and compared with those predicted by a numerical simulation.

In the section 3.3.4, channel shape effects on solution-flow characteristics and the liquid/liquid extraction efficiency in a microchip were studied. As one of the most important characteristics of a microchip, the channel geometries can be designed arbitrary by a microfabrication technology. The shape of a channel-side wall is expected to be one of the most important factors governing the solution-flow profile in the microchannel. Besides the shape effects on the solution-flow characteristics, the shape of a microchannel might influence the efficiencies of solution mixing, a chemical reaction, and liquid/liquid extraction. Therefore, symmetrical and unsymmetrical zigzag-side-walled polymer microchannel chips were fabricated on the basis of an imprinting method, and discussed side-wall structure effects on both the solution-flow characteristics and the liquid/liquid extraction efficiency of an aluminium chelate complex.

3.2 Experimental

3.2.1 Materials, Chemicals, and Sample Preparations

For fabrication of a silicon channel chip and a template for imprinting, silicon wafers (crystal plane <110>) were used. Pyrex glass (Corning 7740) was employed as a cover glass plate for a silicon channel chip. A positive type photoresist (HPR-10, Fujifilm Ohrin Co., Ltd.) and the relevant developer (MIF Developer, Fujifilm Ohrin Co., Ltd.) were used for photolithography. An aqueous KOH (Kanto Chemicals Co., Ltd., G Grade) solution was used as an etching solution for the silicon <111> plane.

For liquid/liquid extraction experiments, $Al(NO_3)_3$, 1-butanol (BuOH), 1,4-dioxiane, *n*-tributyl phosphate (TBP) (Wako Pure Chemical Industrial Ltd., GR grade), and 2,2'-dihydroxyazobenzene (DHAB, Dojindo Chemical Laboratory Co., Ltd.) were used without further purification. Water was purified by distillation and deionization prior to use (GSR-200, Advantec Toyo Co., Ltd.). Water and BuOH were saturated with BuOH and water, respectively. The structural formula of DHAB is shown in Figure 3-1. $Al(NO_3)_3$ (0.05 mmol) was dissolved in 50 ml of an HCl-CH_3COONH_4 buffer solution (pH = 6.3). DHAB dissolved in 1,4-dioxane (1 mL, [DHAB] = 50 mM) was added to the aqueous Al^{3+} solution, and insoluble materials were removed by filtration to give an Al^{3+}-DHAB complex (1:1) solution. The concentration of the complex was determined by absorption spectroscopy; [Al^{3+}-DHAB] = 0.6 mM: the molar absorptivity of the complex at 485 nm = 1.6×10^4 $cm^{-1}M^{-1}$.

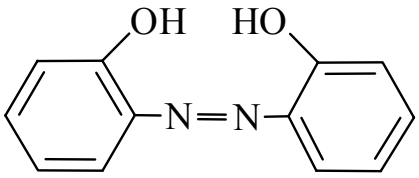

Figure 3-1 The structural formula of DHAB

A main drawback of a polystyrol microchip is low resistibility to an organic solvent as mentioned in Chapter 1. In this study, BuOH was selected as an oil phase for liquid/liquid extraction, since BuOH was inert to polystyrol and the solubility of BuOH in water was rather low: 7.45 wt%. For spectroscopic measurements, furthermore, Al^{3+}-DHAB was used as a probe molecule (i.e., extractant), since the chelate is nonfluorescent in water while it exhibits strong fluorescence in an oil phase.[5-8]

3.2.2 Fabrication and Structures of Microchannel Chips

[1] Polymer Microchannel Chips Used for the Studies in Section 3.3.1

Polymer microchannel chips used for the microspectroscopic studies on the liquid/liquid extraction processes described in the section 3.3.1 were fabricated by the method described in Chapter 2. The structure and dimension of the channel chip are shown in Figure 3-2. The size of the chip was 2.5 cm x 5 cm and, the channel width and depth were set at 180 μm and 12 μm, respectively.

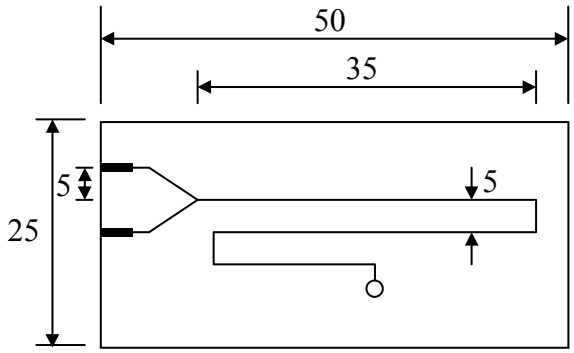

Figure 3-2 Schematic drawing of the microchannel design. The sizes of the microchip structure are shown in millimeter.

[II] Silicon and Polymer Microchannel Chips Used for the Studies in Sections 3.3.2 and 3.3.3

Fabrication of the silicon channel chips used for the studies in the sections 3.3.2 and 3.3.3 was performed as follows. A silicon wafer (1.6 x 3.0 cm) was baked at 1000 °C for 24 h to oxidize the surface of the silicon substrate. The SiO_2 surface layer (thickness about 0.26 μm) of the substrate was employed as a resisting layer during an etching process. A photoresist was spin-coated on the silicon substrate, and pre-baked at 90 °C for 15 min. The substrate was then exposed by a mask aligner through a photomask, which was produced by using a photograph technique. After the resist layer was developed and rinsed with pure water, post-baking of the layer was conducted at 90 °C for 30 min. The silicon substrate was then immersed in an aqueous HF/40% NH_4F solution (1/10, v/v) for 10 min, and the resist layer was removed after rising with pure water. Anisotropic wet etching was performed in a KOH solution, producing the channel pattern on the silicon substrate. As a fluidic device, the substrate was covered

and bonded with a Pyrex glass by an anodic bonding after small holes for an inlet and a drain were fabricated on the glass plate by a Ti : sapphire laser (800 nm).

On the other hand, fabrication of a silicon template for imprinting used for the studies in the section 3.3.2 was performed as follows. Analogous photolithographic processes with those described above were applied to fabricate a silicon template (i.e. resist coating, pre-baking, exposure, development, and post-baking). In the experiments, a photomask possessing an inverse spatial pattern with that used for fabrication of the silicon-channel chip was used. Dry etching of the substrate gave a template. This embossed structure was used to imprint the image onto a polystyrol substrate. Polymer microchannel chips employed for the studies in the section 3.3.2 were then fabricated by the methods described in Chapter 2. Overall fabrication processes of silicon and polymer microchannel chips are illustrated in Figure 3-3.

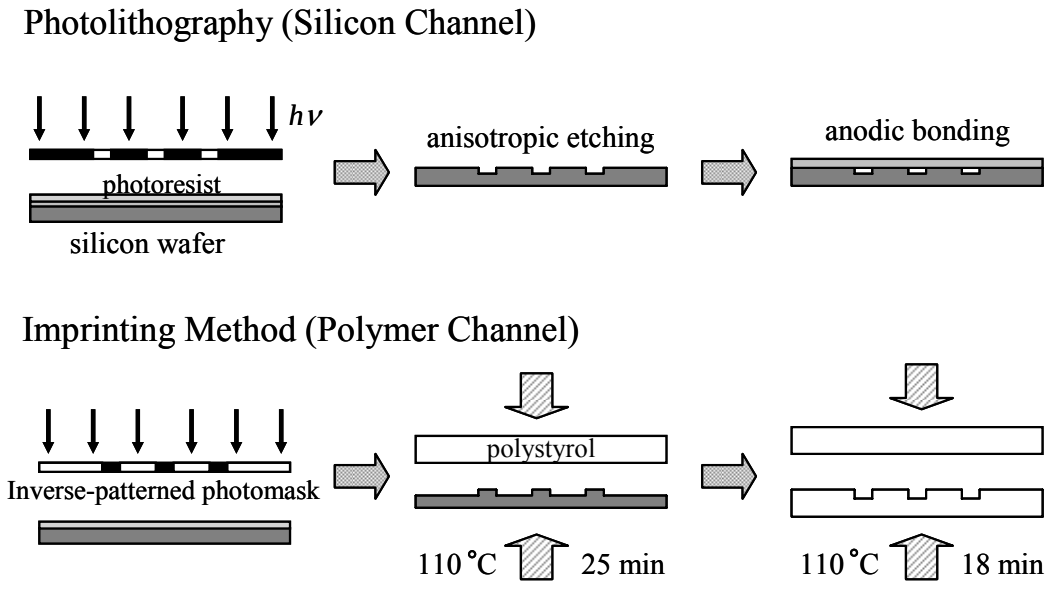

Figure 3-3 Schematic drawing of the fabrication processes of silicon and polymer channel chips.

The spatial patterns of the microchannels employed in the present study are shown in Figure 3-4. The overall sizes of the silicon channel chip and the template were 1.5 cm x 3.0 cm, and the spatial pattern of the microchannel was a double Y style designed for liquid/liquid extraction experiments. The channel corner of the silicon chip was not rectangular as shown in Figure 3-4 (a), owing to the crystal plane of the silicon wafer.

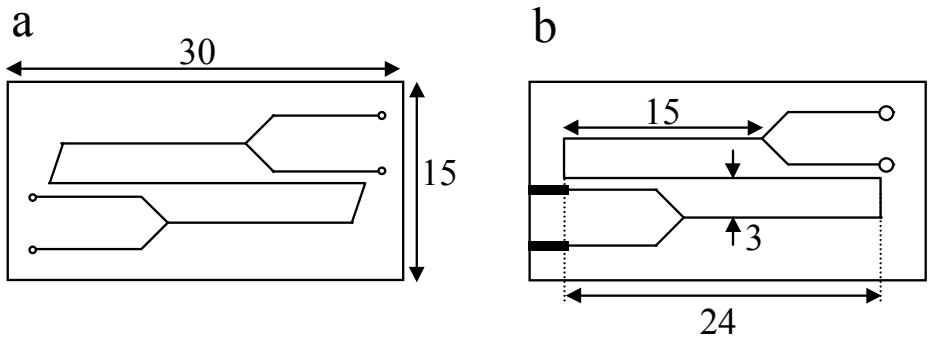

Figure 3-4 Schematic drawing of the microchannel design: silicon (a) and polymer chips (b). The sizes of the microchannel structure are shown in millimeter.

Scanning electron microscope (SEM) images of the cross sections of the silicon channel chip, the silicon template, and the polymer channel chip are shown in Figure 3-5. On the basis of the SEM images, the dimensions of the microchannel were estimated as follows. The width and depth of the silicon channel are 100 μm and 16 μm, respectively. The width and height of the silicon template are 100 μm and 25 μm, respectively. The width and depth of the polymer channel are 100 μm and 20 μm, respectively. The silicon channel was fabricated properly and, the side and edge of the channel were fabricated very sharply by employing anisotropical etching. On the other hand, the polymer channel chip was fabricated precisely as expected from the

dimension of the silicon template and, the side and edge of the channel were not distorted as demonstrated by the SEM image shown in Figure 3-5 (c). This indicates that the imprinting method is very useful to fabricate polymeric microchannel chips, if a template is fabricated accurately. It is worth noting, however, that the depth of the polymer channel is shallower (20 μm) than that expected from the height of the silicon template (25 μm). It is supposed that the polymer (styrol) substrate is elastic, so that the structural relaxation of the polymer material itself proceeds during the fabrication processes: hot embossing and subsequent cooling.

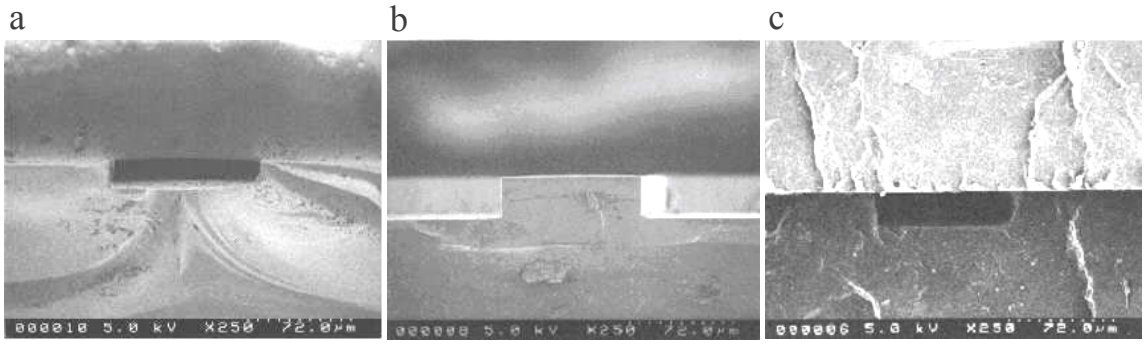

Figure 3-5 Scanning electron microscope (SEM) images of the cross sections of channel chips and a template: a silicon channel chip (a), a silicon template (b), and a polymer channel chip (c).

[III] Zigzag Side-Walled Polymer Channel Chips Used for the Studies in Section 3.3.4

Zigzag side-walled polymer microchannel chips used in studying channel shape effects on the solution-flow characteristics and the liquid/liquid extraction efficiency described in the section 3.3.4 were fabricated by the method shown in Chapter 2. The

microchips having the zigzag-side-walled microchannel, whose structures and dimensions were shown in Figure 3-6, were fabricated for the present purpose of the study. It is noteworthy that the side-walls of the channel in the entrance and exit regions of the chip are fabricated as flat, while those in the middle part are designed as either a symmetrical zigzag or unsymmetrical zigzag structure: abbreviated as *s*- and *us*-channels, respectively. The whole structure of the channel was a double Y style and, the total length of the zigzag channel was designed as 6 cm. The depth of the microchannel was set at 10 μm.

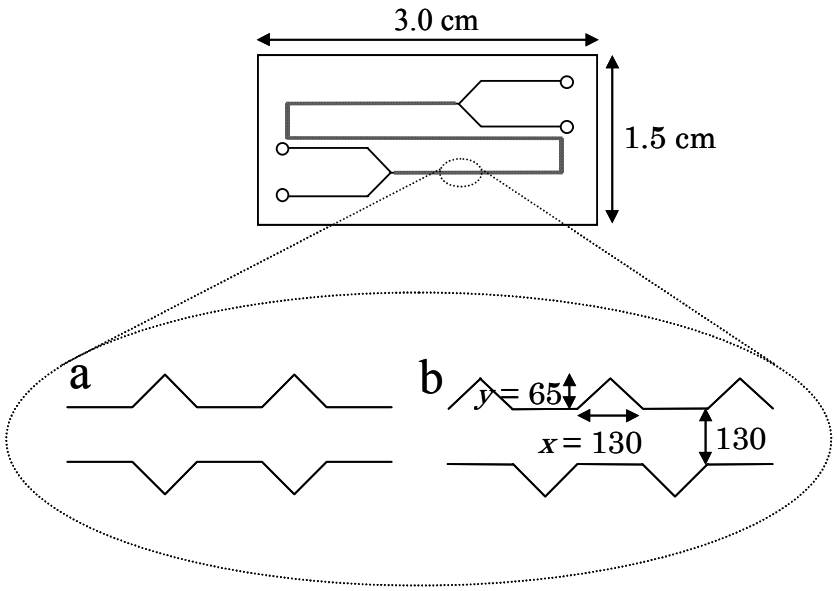

Figure 3-6 Schematic drawing of the structures of symmetrical (a) and unsymmetrical zigzag channel chips (b). The dimensions of the microchannel structures are shown in micrometer.

3.2.3 Experimental Setup

Analogous solution-flow system with that described in Chapter 2 was used in the present study. Two 250 μL volume-syringes, each being filled with BuOH or an aqueous Al^{3+}-DHAB solution, were equipped with a dual-syringe pump. The two fluids were introduced to the channel with the same flow velocity throughout the work. A block diagram of a spatially-resolved fluorescence spectroscopy system used in this study is shown in Figure 3-7.

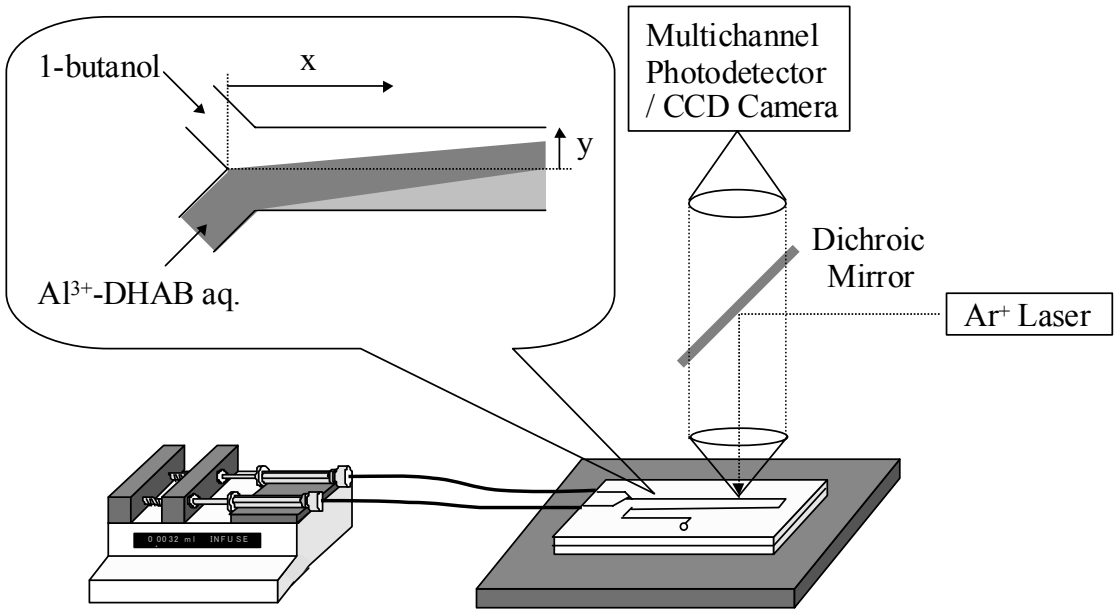

Figure 3-7 A block diagram of the fluorescence microspectroscopy system and a schematic illustration of the flow profile of two solutions in the channel chip.

As an excitation light source, 488 nm-light from an Ar^+ laser was introduced to an optical microscope and focused onto the channel chip set on a microscope 3-D stage

through an objective lens (×100, NA = 0.75, Nikon Co.). The focal spot of the excitation beam (1 μm in diameter at the focal plane) was adjusted to the center of the channel along the z-axis (along the direction of light propagation). Fluorescence from the solution phase was collected by the same objective and led to a polychromator-multichannel photodetector system (PMA-11, Hamamatsu Photonics Co.) through an optical fiber to record fluorescence spectra of Al^{3+}-DHAB at given positions in the channel. By moving the 3-D stage along the x or y axis, position dependent fluorescence spectra of Al^{3+}-DHAB in the microchannel were recorded (Figure 3-7). Since Al^{3+}-DHAB is non-fluorescent in a water phase, only fluorescence from Al^{3+}-DHAB extracted from water to the BuOH phase in the channel can be monitored precisely.

3.3 Results and Discussions

3.3.1 Liquid/Liquid Extraction in Polymer Microchannel Chip

[I] Flow Characteristics in Polymer Microchannels

Flow characteristics in a microchannel is described by low Reynolds-number flow as mentioned in Chapter 2 (Re = 0.03~0.11 in the present experiments). In laminar flow, inertial effects on molecular motions and turbulent mixing of solutions do not play an important role.[9,10] Owing to such flow characteristics, even when two solutions are introduced separately into a single microchannel as shown in Figure 3-7, the two solutions in the channel flow without mutual mixing. On the other hand, when molecular diffusion along the direction of a channel width is important, solute molecules dissolved in one solution phase distribute to the other phase even under

laminar flow. Such behaviors have been confirmed experimentally by several research groups and various applications of the flow characteristics in a microchannel to analytical devices have been also proposed.[11-14]

When two immiscible fluids (i.e., water and BuOH) are brought together into the present polymer microchannel, analogous behaviors with those mentioned above have been observed. BuOH and aqueous Al^{3+}-DHAB solutions were introduced to the microchannel with the same flow velocity as schematically shown in Figure 3-7. The two streams are joined at the junction and flow parallel with each other towards the exit port of the channel. Under an optical microscope, in practice, a clear liquid/liquid interface was observed at the center of the channel along the y-axis and continued to the exit port of the channel without mutual mixing. Furthermore, the interface was not surged even at the corner of the channel. It has been reported that the position of the liquid/liquid interface in a microchannel along the direction of the channel width is governed by the geometry of the channel, a flow velocity, an interfacial tension between two phases, a contact angle at the wall, and so on.[15] For the styrol microchannel used in this study, the stable water/BuOH interface was confirmed with the flow velocity of 0.2 - 1.5 cm s^{-1}. Although the cross section of the polymer channel is not well defined as compared to that of a channel fabricated directly on silicon or glass substrate by photolithography, the flow characteristics in the polymer channel is quite similar to those in silicon or glass-based microchannels.

[II] Liquid/Liquid Extraction in Polymer Microchannels

On the basis of laminar flow in a microchannel, dynamics of liquid/liquid extraction processes can be followed directly. Extraction of Al^{3+}-DHAB from water to

BuOH in the polymer microchannel chip was thus studied. Liquid/liquid extraction of Al^{3+}-DHAB proceeds via three steps: diffusion in the water phase, inter-phase transfer across the interface, and diffusion in the BuOH phase.[16] This indicates that the concentration of Al^{3+}-DHAB extracted to the BuOH phase is dependent on the diffusion rate of the complex in each phase and the distance from the liquid/liquid interface in the BuOH phase (position y). According to the characteristics of laminar flow, furthermore, the distance (i.e., length) from the junction to a given position along the stream (x) corresponds to the contact time between the two fluids (t); t = x / u, where u is a flow velocity. Therefore, the concentration of Al^{3+}-DHAB at a given flow velocity should depend on both x and y in the microchannel. Spatially-resolved spectroscopy of Al^{3+}-DHAB in the microchannel thus affords information about kinetics of the liquid/liquid extraction processes.

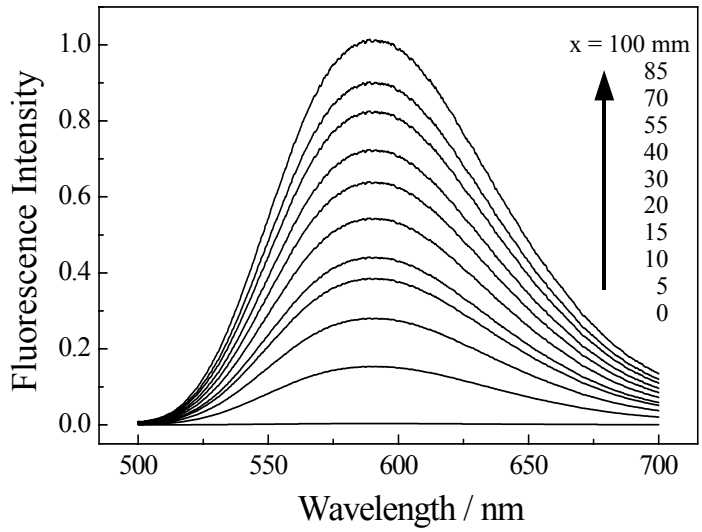

Figure 3-8 Position-dependent fluorescence spectra of Al^{3+}-DHAB along the x-axis (flow direction) in the microchannel; determined at y = 30 μm in the BuOH phase separated from the water/BuOH interface, u = 1.5 cm s^{-1}.

Figure 3-8 shows the fluorescence spectra of Al^{3+}-DHAB observed at various x in the BuOH phase (y = 30 μm) in the channel (u = 1.5 cm s^{-1}). At the junction (x = 0), no fluorescence was observed. At the downstream-side from the junction, a broad fluorescence band (λ_{max} = 583 nm) was observed. The shape of the fluorescence spectrum agreed very well with that of Al^{3+}-DHAB in a homogeneous BuOH, so that the fluorescence observed was ascribed to Al^{3+}-DHAB extracted to the BuOH phase. Extraction of Al^{3+}-DHAB from water to BuOH proceeds along with solution-flow. Thus, the fluorescence intensity, corresponding to the concentration of Al^{3+}-DHAB, increases with x.

Analogous experiments with those shown in Figure 3-8 were performed at several flow velocities. The position (x) dependence of the fluorescence intensity is summarized in Figure 3-9, in which the data are shown relative to the saturated fluorescence intensity (1.0). From a separate experiment, the partition coefficient of Al^{3+}-DHAB between water and BuOH (P) was determined to be 19.0. The fluorescence intensity of 1.0 in the figure thus corresponds to P to be 19.0, and the x dependence of the fluorescence intensity at a given flow velocity provides an information about the liquid/liquid extraction processes in the microchannel. At u = 0.38 cm s^{-1}, the fluorescence intensity increased sharply with x upto x ~ 3 cm and then became constant (unity). These findings imply that extraction of Al^{3+}-DHAB proceeds with an increase in x and the distribution equilibrium is attained at x > 3 cm. At a faster flow velocity, the fluorescence intensity increased gradually with x as compared to that at u = 0.38 cm s^{-1} and the x value necessary for reaching the distribution equilibrium was prolonged.

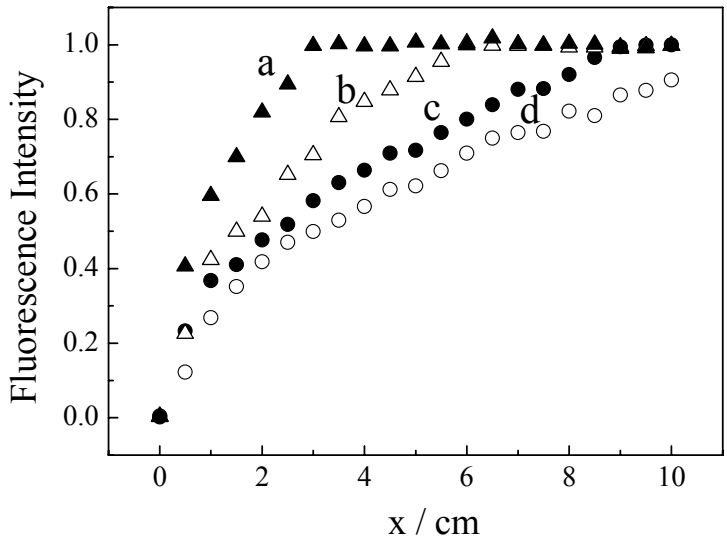

Figure 3-9 Position dependence of the fluorescence intensity of Al^{3+}-DHAB along the x-axis at several flow velocities; u = (a) 0.38, (b) 0.75, (c) 1.13, and (d) 1.5 cm s^{-1}.

At a given flow velocity, the distance from the junction along the solution stream (x) corresponds to the contact time between the two fluids (t) as mentioned before. Therefore, the data in Figure 3-9 can be converted to the contact time dependence of the fluorescence intensity: $t = x/u$. As clearly seen in Figure 3-10, all the data in Figure 3-9 fall on the single curve. The flow velocity dependence of the extraction efficiency at a given x is shown clearly and, it is concluded that extraction of Al^{3+}-DHAB in the channel is governed essentially by the contact time between the two phases.

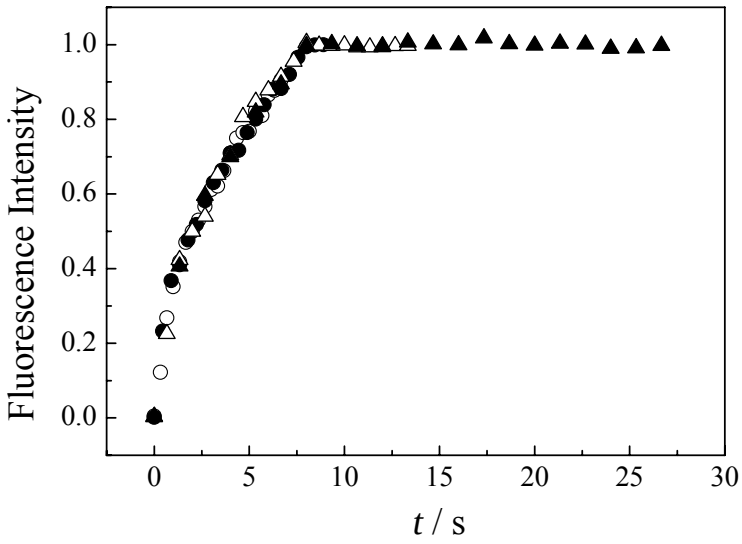

Figure 3-10 Contact time (*t*) dependence of the fluorescence intensity of Al^{3+}-DHAB in the microchannel. The data were taken from Figure 3-9.

In order to study further details on the extraction processes, spatially-resolved fluorescence spectroscopy was conducted as a function of y. The results are summarized as a *t* dependence of the fluorescence intensity in Figure 3-11. The data shown in Figure 3-9 (y = 30 μm) are also included (shown by the closed triangles). As the monitoring position was shifted to far from the liquid/liquid interface from **a** to **d** in Figure 3-11, the fluorescence intensity at a given *t* became weaker and it took more time to reach a constant fluorescence intensity. Near the interface (y = 30 μm), namely, the time necessary to reach a constant fluorescence intensity was about 8 s while the fluorescence intensity monitored at y > 50 μm did not saturate before *t* = 15 s. Furthermore, an induction period was observed at *t* < 2 s when the fluorescence was monitored at y = 90 μm. Phenomenologically, these findings agree very well with that

expected for liquid/liquid extraction in the microchannel, as schematically shown in Figure 3-7.

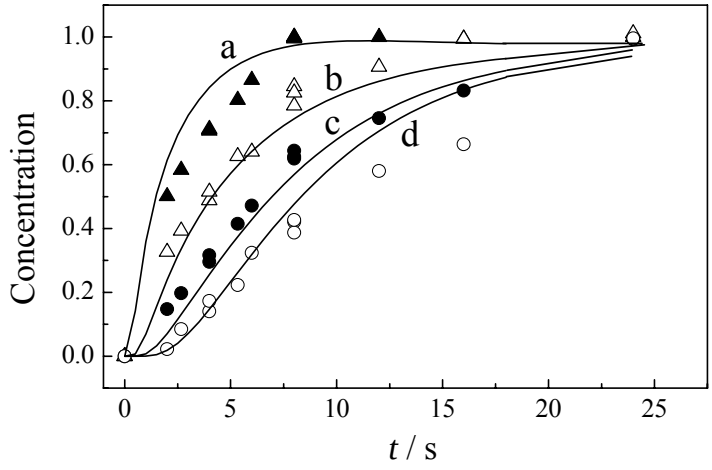

Figure 3-11 Contact time dependence of the fluorescence intensity of Al^{3+}-DHAB determined at various positions from the water/BuOH interface; y = 30 (a), 50 (b), 70 (c), and 90 μm (d). The solid curves represent the results by computer simulations (see the main text).

[III] Simulation of Liquid/Liquid Extraction in a Microchannel

In order to explain the present results and to test the performances of the polymer microchannel, a numerical simulation of the liquid/liquid extraction processes in the channel was performed.[17] Extraction proceeds via three mass-transfer steps as mentioned before, so that the experimental data should be explained along the same context. It is important to note that the fluid characteristics in the channel, particularly, those in a low aspect-ratio rectangular channel (12 μm depth and 180 μm width) must

be considered. In the present case, the two fluids run parallel in the channel without mixing, so that the width of each fluid layer does not vary during solution-flow, which simplifies the numerical simulation for liquid/liquid extraction in the microchannel.

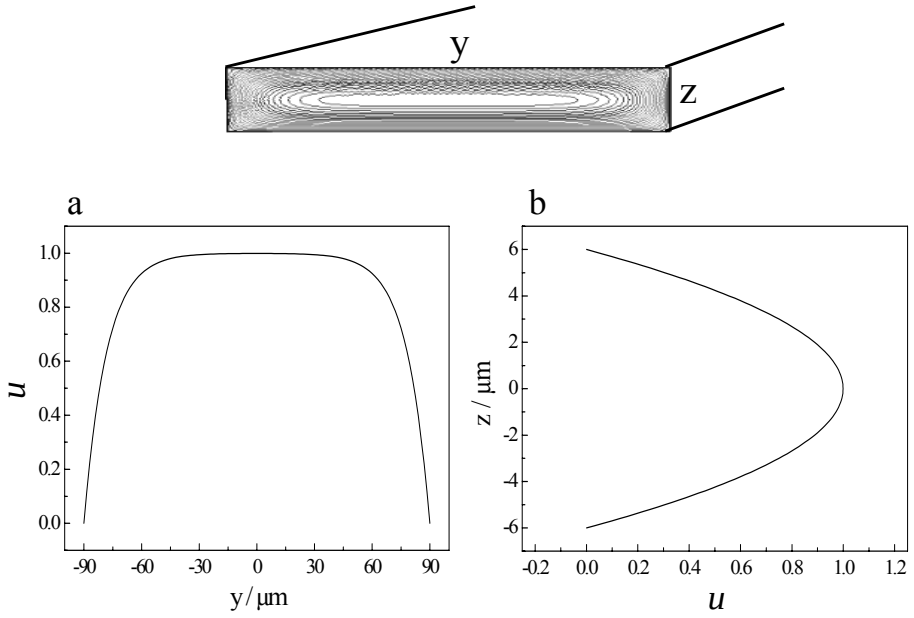

Figure 3-12 Flow profiles predicted by numerical simulations along the width direction (y-axis, (a)) and the depth direction (z-axis, (b)) in the microchannel having the low aspect ratio.

The low aspect ratio of the channel also influences the flow profile in the channel.[18,19] The flow profiles predicted by numerical simulations along the channel-width direction (y-axis) and the depth direction (z-axis) are shown in Figure 3-12. Since the channel is very shallow compared to the width, the flow profile along the depth direction (z-axis) becomes parabolic as shown in Figure 3-12 (b) and the flow velocity depends on the z position in the channel, while the flow profile along the y-axis is plug-like; the flow velocity profile along the *y*-axis is almost constant except for the

edge region of the channel as shown in Figure 3-12 (a). It is well known that a parabolic flow profile is unfavorable for ordinary macro-scale chromatography, because it leads to a concentration gradient of a solute along the flow direction. In a microchannel, on the other hand, self-diffusion of a solute plays an important role. As an example, an ordinary-sized molecule having a diffusion coefficient of ~10^6 cm^2 s^{-1} can diffuse 10 μm within 1 s. In the present channel, therefore, the concentration gradient along the *z*-axis is cancelled by molecular diffusion in a micrometer dimension. This also simplifies the simulation of mass-transfer of Al^{3+}-DHAB across the water/BuOH interface as described below.

On the basis of above discussions, the extraction processes in the channel were modeled as successive one-dimensional mass-transfer steps across the liquid/liquid interface (along *y*-axis). Diffusion of Al^{3+}-DHAB in each phase is thus described by the one-dimensional Fick's law.

$$C_W(y,t) = D_W \frac{\partial C_W(y,t)^2}{\partial t^2} \qquad \text{in water} \quad (y < 0) \qquad (3\text{-}1)$$

$$C_O(y,t) = D_O \frac{\partial C_O(y,t)^2}{\partial t^2} \qquad \text{in BuOH} \quad (y > 0) \qquad (3\text{-}2)$$

In eqs. (3-1) and (3-2), C_w (C_o) and D_w (D_o) represent the concentration and the diffusion coefficient of Al^{3+}-DHAB in water (BuOH), respectively. If interfacial mass transfer of Al^{3+}-DHAB across the two phases is fast enough as compared with diffusion of the complex in each phase, the concentration ratio of the complex in the vicinity of the interface at given *t* should be equal to the equilibrium partition coefficient, *P*.

$$P = \frac{C_O(interface,t)}{C_W(interface,t)} \qquad (3\text{-}3)$$

The D_w and D_o values were calculated to be 6.1×10^{-6} and 2.2×10^{-6} cm^2s^{-1}, respectively, on the basis of the Stokes-Einstein equation. Before contacting two solutions, $C_o(y, 0) = 0$ and $C_w(y, 0) = 1$ are held. Under these conditions, a computer simulation was performed for liquid/liquid extraction of Al^{3+}-DHAB in the microchannel and the results were shown in Figure 3-11 as the solid curves. The calculated curves reproduced roughly the experimental data in spite of the application of the one-dimensional model.

It is worth noting that the induction period observed for extraction at y = 90 μm and $t < 3$ s has been also reproduced by the simulation. This demonstrates that extraction of a solute in a microchannel can be modeled as one-dimensional mass-transfer processes as long as the rate-determining step is diffusion of a solute in each phase. It is worth pointing out, furthermore, that the present simulation does not consider structural factors such as roughness of the edge and bottom surface of the channel. Slight discrepancies between the observed data and simulated ones might be due to such effects. Nonetheless, overall performances of the polymer microchannel chip for liquid/liquid extraction agree with those predicted by the ideal-model simulation.

3.3.2 Characteristics of Silicon and Polymer Microchannel Chips

The performances of both silicon and polymer channel chips were compared and evaluated on the basis of the results of liquid/liquid extraction of Al^{3+}-DHAB. When two immiscible fluids were brought together into a silicon or polymer microchannel chip, analogous behaviors with those described in the previous section were observed. Namely, the two streams were joined at the junction and flow parallel with each other

toward the exit of the channel. It was confirmed that the water/BuOH interface was stable during the experiments. Furthermore, the two parallel fluids were separated at the exit junction of the channels. Therefore, dynamics of liquid/liquid extraction of Al^{3+}-DHAB can be followed by using these channel chips, and the characteristics of both channel chips can be compared.

The fluorescence spectra of Al^{3+}-DHAB observed at various x in the BuOH phase (y = 30 μm) in the silicon channel are shown in Figure 3-13 (u = 1.5 cm s^{-1}). It was confirmed that analogous fluorescence spectrum of Al^{3+}-DHAB with that shown in Figure 3-8 was observed even by using the silicon channel chip. The fluorescence intensity of Al^{3+}-DHAB in the BuOH phase increased gradually as shifting the monitoring position toward the downstream side of the channel, confirming liquid/liquid extraction in the channel chip.

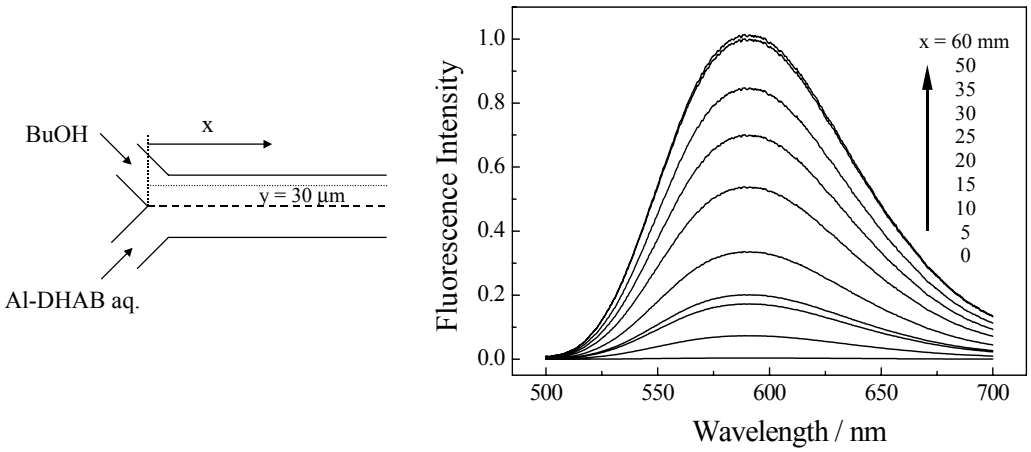

Figure 3-13 The position-dependent fluorescence spectra of Al^{3+}-DHAB along the x-axis in the BuOH phase (y = 30 μm) in the silicon channel chip (u = 1.5 cm s^{-1}).

Analogous experiments with those in Figure 3-13 were conducted at several flow velocities (0.75 - 1.5 cm s^{-1}), and the x dependence (y = 30 μm) of the fluorescence intensity is shown in Figure 3-14 (a). Also, the data in Figure 3-14 (a) were converted to the contact time dependence of the fluorescence intensity: t = x / u in Figure 3-14 (b). As described previously, all the data in Figure 3-14 (b) fall on a single curve. This indicates that liquid/liquid extraction in the silicon channel chip is governed by the contact time between the two phases, similar to that in the polymer channel chip.

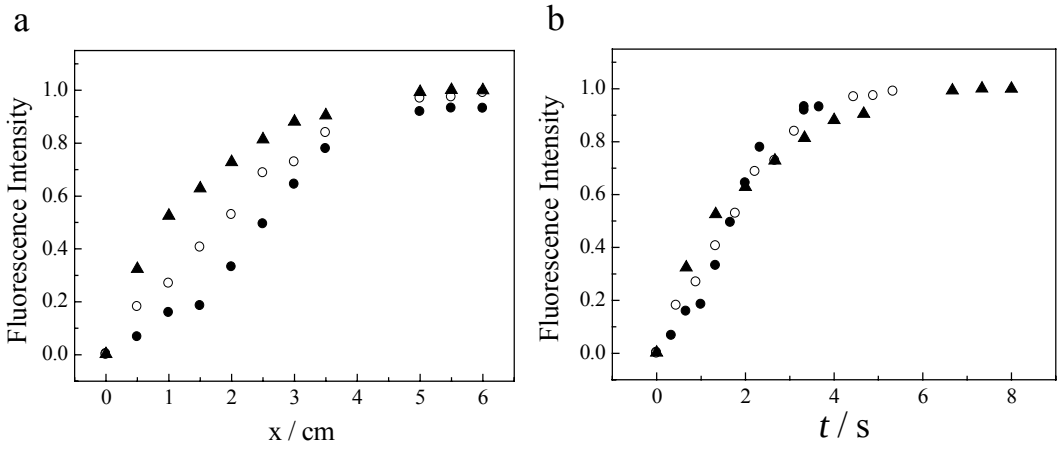

Figure 3-14 (a) The x dependence of the fluorescence intensity of Al^{3+}-DHAB at several flow velocities (y = 30 μm) in the silicon channel chip: 0.75 (▲), 1.125 (○), and 1.5 cm s^{-1} (●). (b) Contact time dependence of the fluorescence intensity in the silicon channel chip: 0.75 (▲), 1.125 (○), and 1.5 cm s^{-1} (●). All of the data were taken from Figure 3-14 (a).

Analogous experiments with those in Figure 3-13 or Figure 3-14 were also performed by using the polymer channel chip, whose spatial pattern was the same with that of the silicon channel chip. Furthermore, a spatially-resolved fluorescence study on

the liquid/liquid extraction processes was conducted as a function of y by using both the silicon and polymer microchannel chips. A *t* dependence of the fluorescence intensity observed by each channel chip is summarized in Figure 3-15.

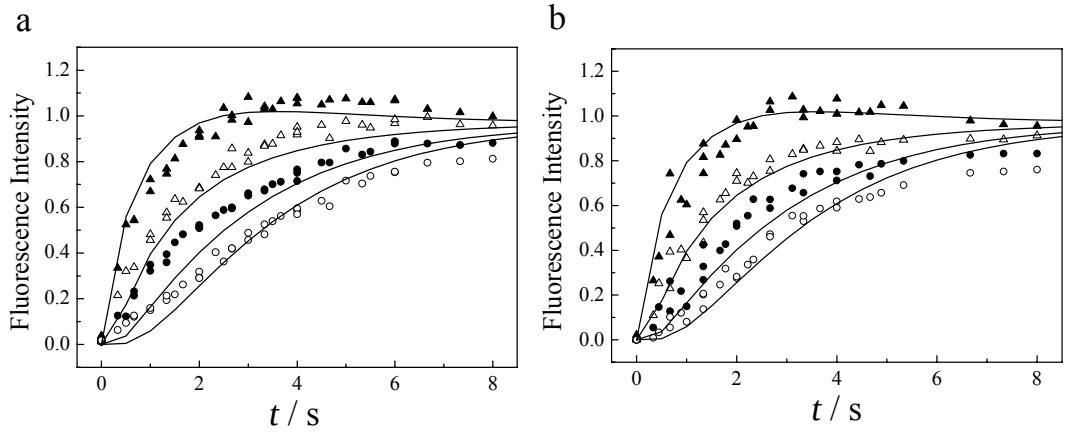

Figure 3-15 Contact time (*t*) dependences of the fluorescence intensity observed by the polymer (a) and the silicon channel chips (b). The solid curves indicate the results by the numerical simulations of liquid/liquid extraction of Al^{3+}-DHAB: y =10 (▲), 20 (△), 30 (●), and 40 μm (○).

As shown in Figure 3-15, analogous results were obtained for both the silicon and polymer channel chips. Near the interface (y = 10 μm), the time necessary to reach a constant fluorescence intensity was about 3 s in both channel chips. However, the fluorescence intensity observed at y = 10 - 40 μm was not saturated even at *t* = 8 s. This indicates that a distribution equilibrium is not reached at a flow velocity of 0.75 - 1.5 cm s^{-1} in the microchannel chip. In addition, a computer simulation was also performed similar to that described in the section 3.3.1, and the results were shown in Figure 3-15 as the solid curves. The simulated curves reproduced roughly the experimental data for

both the silicon and polymer channel chips. It is confirmed that liquid/liquid extraction of Al^{3+}-DHAB in both channel chips proceeds as predicted from the three mass transfer steps as mentioned before. The characteristics of the extraction processes in a microchannel do not change irrespective of a chip material.

A question is arisen about whether the characteristics of the liquid/liquid extraction processes depend on the surface conditions of the substrate (surface charge, surface characteristics, electroosmotic effects, and so forth) or not. Usually, an analysis of a flow profile in a microfluidic channel is conducted on the basis of the Navier-Stokes theory. However, the theory does not consider the surface properties of a substrate. Also, an analysis of a laminar flow profile, which is expected to be influenced by a substrate surface, has been reported, in stead of employing the classical Navier-Stokes theory for a solid/liquid interface.[20] According to these reports, the flow characteristics in a microchannel change by a variation of the viscosity of a fluid in the surface layer of about 10 Å from the channel-wall. Therefore, it is concluded that the characteristics of the liquid/liquid extraction processes of Al^{3+}-DHAB by the hydrophilic silicon and hydrophobic polymer channels accord approximately with each other, since the fluorescence intensity profiles in both channels do not change appreciably.

3.3.3 Solvent Dependence of the Liquid/Liquid Extraction Processes

A solvent dependence of the liquid/liquid extraction dynamics in the silicon channel chip was studied. In the experiments, tributylphosphate (TBP) was used as an oil phase instead of using BuOH. The water and TBP streams were joined at the junction of the channel chip, flow parallel with each other toward the exit junction of the channel, and separated to each phase as confirmed by observation under an optical

microscope. The x dependence of the fluorescence spectrum of Al^{3+}-DHAB in the TBP phase (y = 30 μm) in the channel is shown in Figure 3-16. The fluorescence spectrum of Al^{3+}-DHAB in Figure 3-16 was in accordance with that observed in bulk TBP. The fluorescence intensity (583 nm) increased gradually with proceeding liquid/liquid extraction of Al^{3+}-DHAB along solution-flow.

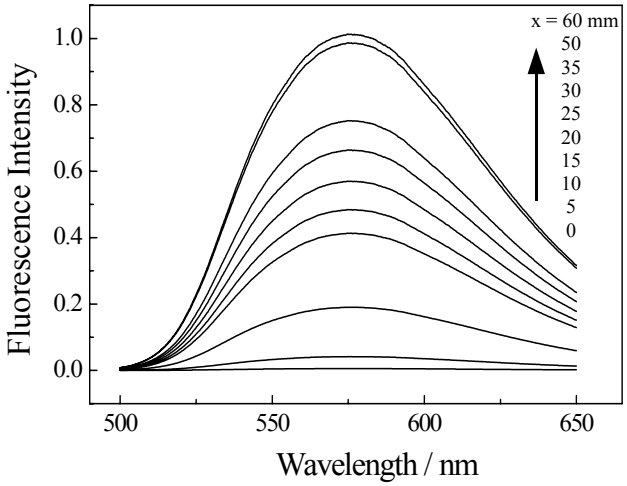

Figure 3-16 The x dependence of the fluorescence spectrum of Al^{3+}-DHAB in the TBP phase (y = 30 μm) in the channel (u = 1.5 cm s^{-1}).

Analogous experiments with those in Figure 3-16 were performed at several flow velocities (1.5-0.75 cm s^{-1}) as a function of y (10, 20, 30, and 40 μm). The results are summarized as a contact time (t = x / u) dependence of the fluorescence intensity as shown in Figure 3-17. The fluorescence spectrum of the TBP solution of Al^{3+}-DHAB equilibrated with water was measured in the microchannel as a reference. The fluorescence intensity at 580 nm is shown relative to the equilibrium value (1.0). At y =

10 μm from the interface, the fluorescence intensity at t = 2 s is stronger than 1.0 and the intensity decreases slowly with time toward the equilibrium value (1.0). This is characteristic to water/TBP extraction and differs from the dynamics of the water/BuOH extraction processes. It is supposed that this is because of a smaller diffusion coefficient of Al^{3+}-DHAB in TBP (1.6 x 10^{-6} cm^2 s^{-1}) relative to that in BuOH (2.2 x 10^{-6} cm^2 s^{-1}), since the viscosity of TBP (3.78 cp at 20 °C) is higher than that of BuOH (2.85 cp at 20 °C). In order to confirm this further, a numerical simulation of the water/TBP extraction processes was performed. The partitioning coefficient of Al^{3+}-DHAB between water and TBP (P) was determined to be 100 from separate experiments. The solid curves shown in Figure 3-17 indicate the results by the numerical simulations of water/TBP extraction of Al^{3+}-DHAB in the microchannel. The simulated curves reproduced very well the experimental data even for the water/TBP extraction processes. It is concluded again that the dynamics of the liquid/liquid extraction processes in the microchannel can be explained by a one-dimensional mass-transfer model along the perpendicular axis to the stream (y-axis). In-situ spatially-resolved fluorescence spectroscopy in the microchannel chip demonstrated explicitly that the dynamics of the water/TBP extraction processes were different from those of the water/BuOH extraction processes.

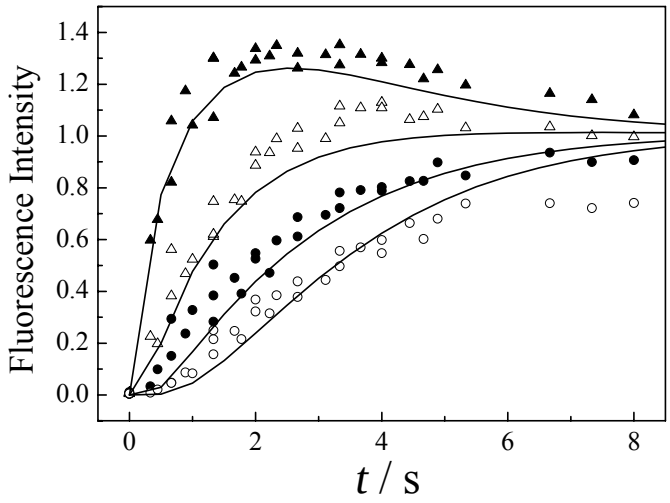

Figure 3-17 Contact time (*t*) dependence of the fluorescence intensity in the silicon channel chip: y =10 (▲), 20 (△), 30 (●), and 40 μm (○). The solid curves indicate the results by the numerical simulation for water/TBP extraction of Al^{3+}-DHAB.

3.3.4 Channel Shape Effects on Solution-Flow Characteristics and the Liquid/Liquid Extraction Efficiency in Polymer Microchannel Chips

[I] Channel Shape Effects on the Solution-Flow Characteristics in Zigzag Microchannels

When water and an oil are introduced separately to a flat-side-walled Y-structured channel chip with the same solution-flow velocity (*u*), both phases run parallel with each other and a flat oil/water interface can be observed under an optical microscope, as described in the section 3.3.1. By using a zigzag-side-walled microchannel chip,

however, solution-flow characteristics were dependent on the shape of the channel side-wall: *s*- or *us*-zigzag channel. The results are shown in Figure 3-18, where two phases were stained by blue (seen as dark, water phase) and red dyes (seen as clear, oil phase) for clarity. In the *s*-channel, the water/BuOH interface was flat as long as an observation was made under an optical microscope, while that in the *us*-channel was sinusoidal, as shown in Figure 3-18. In the entrance and exit regions of the channel chip just before and after the Y-junction, respectively, the channel side-walls were designed to be flat so that the water/oil interface was flat. In the exit region of the channel, furthermore, both phases were well separated even under a solution flow velocity of 1.23 cm s^{-1}.

In the *us*-channel, it is worth noting that analogous sinusoidal oil/water interfacial structures with those in Figure 3-18 (a) are observed irrespective of the flow velocity studied (u = 0.62 - 1.23 cm s^{-1}). On the other hand, a sinusoidal liquid/liquid interface was discernible in a deeper (y/x > 0.5, Figure 3-19 (a)) or shallower unsymmetrical zigzag channel (y/x < 0.5, Figure 3-19 (b)) as compared to the dimension of the fabricated channel (y/x = 0.5, Figure 3-19 (c)). In order to explain such experimental observations, numerical simulations for the solution-flow characteristics in the channels were conducted on the basis of a finite-element method (PdEase-2D, Macsyma Inc.) and the Navier-Stokes equation. The results are shown in Figure 3-19 as vectorial solution-flow profiles, which are shown by the length and direction of each arrow.

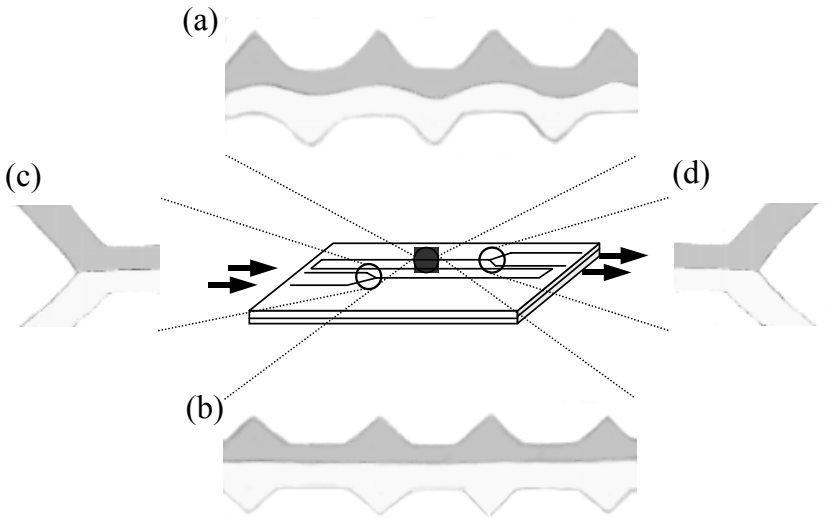

Figure 3-18 Solution-flow characteristics in the unsymmetrical (a) and symmetrical channel chips (b). (c) and (d) are the images at around the entrance and exit Y-junctions, respectively.

In a deeper or shallower *us*-channel compared to the dimension shown in Figure 3-6 (b), stable solution-flow was not attained, in which a relatively high or low *y/x* aspect ratio of the side-wall zigzag structure disturbs formation of a sinusoidal water/oil interface. These results agree very well with those by the experimental observations. A deeper or shallower unsymmetrical zigzag channel compared to the dimension shown in Figure 3-6 does not influence appreciably the water/oil interfacial structure. Therefore, the channel sizes shown in Figure 3-6 are the optimum values to produce a sinusoidal liquid/liquid interface in the microchannel at the solution-flow velocity studied. Although further detailed simulations are needed to elucidate precisely the factors governing the channel-shape effects on the solution-flow characteristics, the channel shape and dimensions are shown to be very important for designing a chemical reaction in a channel chip.

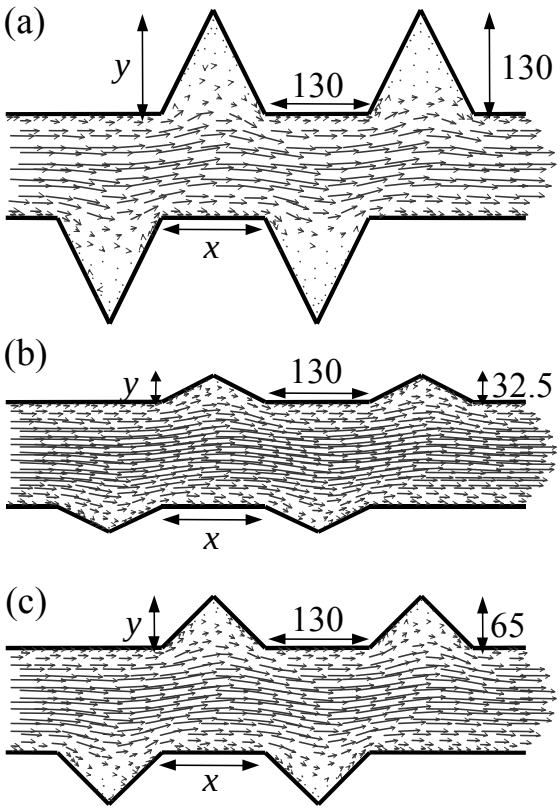

Figure 3-19 Numerical calculations of the flow characteristics (vectorial presentation) in unsymmetrical channels with several channel dimensions. The sizes are shown in micrometer.

[II] Channel Shape Effects on the Liquid/Liquid Extraction Efficiency in Zigzag Microchannels

Water-to-oil extraction of Al^{3+}-DHAB in both *s*- and *us*-channels was studied on the basis of spatially-resolved fluorescence spectroscopy. In water, Al^{3+}-DHAB is almost non-fluorescent, while that in an oil exhibits strong fluorescence. Therefore, when Al^{3+}-DHAB is extracted from water to the oil phase (i.e., BuOH) along the solution-flow direction in the microchannel (x), the extraction processes of the Al^{3+}-DHAB can be followed as described in the section 3.3.1.

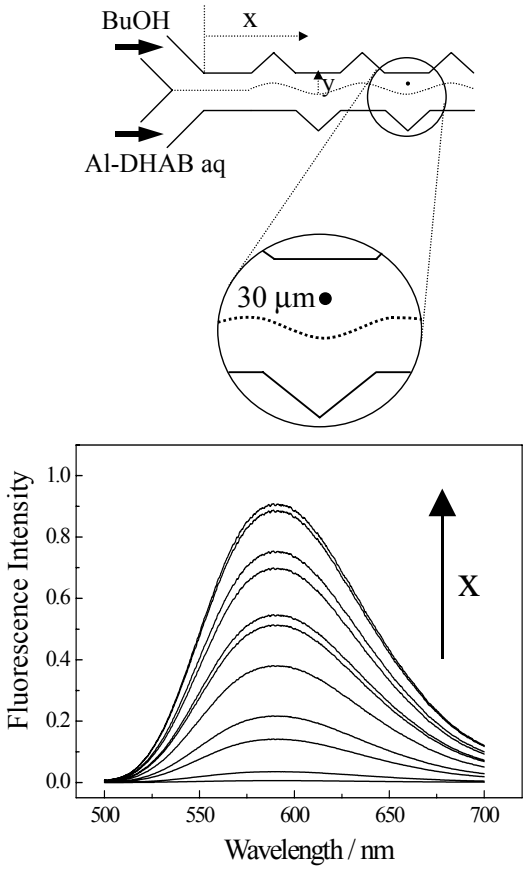

Figure 3-20 Water-to-BuOH extraction of Al^{3+}-DHAB in the *us*-channel. The spectra were measured in the BuOH phase, 30 μm separated from the oil/water interface; u = 1.23 cm s^{-1}. Excitation wavelength: 488 nm.

An aqueous Al^{3+}-DHAB solution and water-saturated BuOH were introduced to the channel chip at u = 1.23 cm s^{-1}. The fluorescence from Al^{3+}-DHAB (excited at 488 nm, spot size ~1 μm) was monitored along x in the BuOH phase, separated by 30 μm from the water/BuOH interface, as the data were shown in Figure 3-20. The fluorescence intensity shown by 1.0 in Figure 3-20 corresponds to the equilibrium partition coefficient of Al^{3+}-DHAB between the two phases (19.0). The fluorescence intensity of Al^{3+}-DHAB increased with an increase in x, demonstrating that

water-to-BuOH extraction of Al^{3+}-DHAB proceeded with solution-flow in the channel. The fluorescence intensity at a given x was dependent on the flow velocity similar to the results described above. Based on the x value at a given *u*, the contact time between water and BuOH in the microchannel (*t*) can be calculated: *t* (s)= x (cm) / *u* (cm s^{-1}). The data obtained at several *u* are summarized in Figure 3-21 as a contact time dependence of the fluorescence intensity. As can be seen in the figure, all of the data fall on a single curve. The results demonstrate clearly that extraction of Al^{3+}-DHAB is governed by the contact time between the two phases in the microchannel.

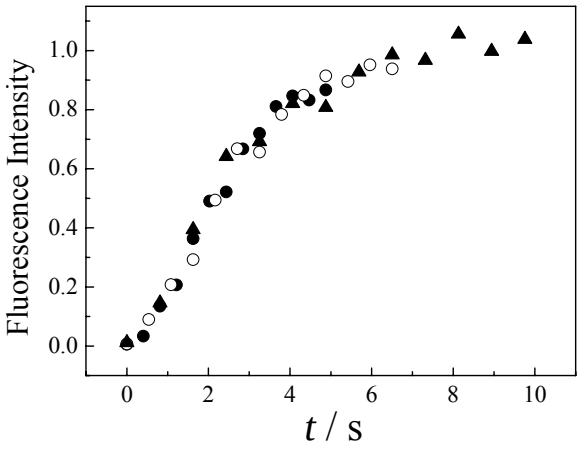

Figure 3-21 Contact time dependence of the fluorescence intensity of Al^{3+}-DHAB in the unsymmetrical zigzag channel, observed in the BuOH phase, separated 30 μm from the water/BuOH interface: *u* = 1.23 (●), 0.92 (○), and 0.62 (▲) cm s^{-1}.

The importance of the contact time between the two phases indicates that mass transfer across the interface governs the extraction efficiency (*P*) in the microchannel. In practice, the fluorescence intensity observed at 50 μm separated from the interface was weaker than that at 30 μm (for a given *t* or x) as shown in Figure 3-22, proving that

the interfacial mass transfer rate of Al^{3+}-DHAB and the diffusion coefficient of the complex in each phase determined the extraction rate for both the *s*- and *us*-zigzag channels. As one of the most important results from the present study, furthermore, a close inspection of the data in Figure 3-22 suggests that the *P* determined at a given *t* or x is higher by the *us*-channel compared with that by the *s*-channel. Namely, the extraction efficiency (i.e., fluorescence intensity) determined at 30 μm from the water/BuOH interface (closed circles) in the *us*-channel reaches almost unity at *t* ~8 s, while that in the *s*-channel levels off at ~0.8 (*t* ~8 s). Nonetheless, a direct comparison of the positional data obtained at 30 or 50 μm separated from the flat (*s*-channel, b) and sinusoidal interfaces (*us*-channel, a) is not necessarily guaranteed.

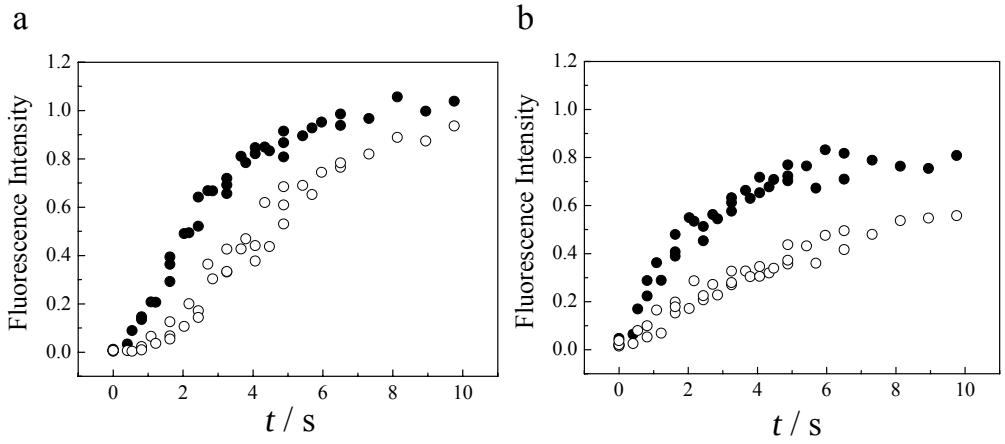

Figure 3-22 Contact time dependence of the fluorescence intensity of Al^{3+}-DHAB determined in the BuOH phase, separated by 30 (●) or 50 μm (○) from the water/BuOH interface: unsymmetrical (a) and symmetrical channels (b).

In order to obtain clearer data, therefore, the oil phase was collected from the exit of the channel chip to determine the water-to-BuOH extraction efficiency of Al^{3+}-DHAB. Knowing the molar extinction coefficient of Al^{3+}-DHAB in BuOH to be 12000 M^{-1} cm^{-1} at 485 nm, *P* was determined to be 0.65 or 0.47 for the *us*- or *s*-channel, respectively, demonstrating more efficient extraction of Al^{3+}-DHAB in the unsymmetrical zigzag channel (u = 1.23 cm s^{-1}). It is worth noting that the contact time between the two phases is determined by the channel length and *u*, so that those in both the *s*- and *us*-channels are essentially the same, which cannot explain the difference in *P* between the two chips. Because the sinusoidal oil/water interfacial area is larger than the interfacial area produced by the *s*-channel (i.e., flat surface), this would be the primary origin of the difference in the *P* values between the two channel chips. Although the roles of the channel geometries concerning the chemical characteristics in a chip have been rarely discussed, the present results demonstrated clearly that the three-dimensional structures of a channel chip were a very important factor governing the chemistry in a microchannel chip.

3.4 Conclusion

The dynamics of the liquid/liquid extraction processes of Al^{3+}-DHAB in the microchannel chips were studied on the basis of spatially-resolved fluorescence spectroscopy. When two immiscible fluids were brought together into the channel chip by pressure-driven flow at the same velocity, a stable parallel stream was observed without mutual mixing of the two phases. Extraction of Al^{3+}-DHAB from water to BuOH was then studied as the fluorescence intensity of Al^{3+}-DHAB in the BuOH phase along the flow direction (x) as well as along the channel-width direction (y). It was

confirmed that extraction proceeded with solution-flow and governed by the contact time (t) between the two phases. A one-dimensional mass-transfer model along the channel direction explained very well the experimental observations. On the basis of the experiments, the mass-transfer processes across the water/oil interface in the microchannel were elucidated in detail.

On the other hand, it is easily expected that the flow characteristics in a microchannel could be governed by several factors such as the channel dimension, the channel geometries, and the solution-flow velocity. Therefore, the liquid/liquid extraction efficiency was studied as a function of these factors. In practice, it was demonstrated that these factors controlled both the solution-flow characteristics and the liquid/liquid extraction processes of Al^{3+}-DHAB. Chemical and physical characteristics of a microchannel chip and the mass-transfer processes in a microchannel play important roles in other chemical/physical processes as discussed in the following chapters.

3.5 References

1) Rossi, T. M.; Shelly, D. C.; Warner, I. M. *Anal. Chem.* **1982**, 54, 2056-2061.

2) Watarai, H.; Cunningham, L.; Freiser, H. *Anal. Chem.* **1982**, 54, 2390-2392.

3) Watarai, H.; Freiser, H. *J. Am. Chem. Soc.* **1983**, 105, 191-194.

4) Freiser, H. *Bull. Chem. Soc. Jpn.* **1988**, 61, 39-45.

5) Freeman, D. C., Jr.; White, C. E. *J. Am. Chem. Soc.* **1956**, 78 2678-82.

6) Olsen, R.; Diehl, H. *Anal. Chem.* **1963**, 35, 1142-1144.

7) Diehl, H.; Olsen, R.; Spielholtz, G. I.; Jensen, R. *Anal. Chem.* **1963**, 35, 1144-1154.

8) Watanabe, K.; Yoshizawa, H.; Kawagaki, K. *Bunseki Kagaku* **1981**, 30, 640-645.

9) Brody, J. P.; Yager, P.; Goldstein, R. E.; Austin, R. H. *Biophys. J.* **1996**, 71, 3430-3441.

10) Faber, T. E. *"Fluid Dynamics for Physicists"* **1995**, Cambridge University Press, Cambridge.

11) Brody, J. P.; Osborn, T. D.; Forster, F. K.; Yager, P. *Sens. Actuat. A: Phys.* **1996**, 54, 704-708.

12) Weigl, B. H.; Yager, P. *Sens. Actuat. B: Chem.* **1997**, 38, 452-457.

13) Brody, J. P.; Yager, P. *Sens. Actuat. A: Phys.* **1997**, 58, 13-18.

14) Kenis, P. J. A.; Ismagilov, R. F.; Whitesides, G. M. *Science* **1999**, 285, 83-85.

15) Shaw, J.; Miller, B.; Turner, C.; Harper, M.; Graham, S. "*Analytical Methods Instrum."* Special Issue μTAS'96, **1996**, 185.

16) Cussler, E. L. *"Diffusion-Mass Transfer in Fluid Systems"* 2nd ed. **1997**, Cambridge University Press, Cambridge.

17) Ferziger, J. H.; Peric, M. *"Computational Methods for Fluid Dynamics"* **1996**, Springer-Verlag, New York.

18) Kim, H.-B.; Kogi, O.; Kitamura, N. *Anal. Chem.* **1999**, 71, 4338-4343.

19) Kamholz, A. E.; Weigl, B. H.; Finlayson, B. A.; Yager, P. *Anal. Chem.* **1999**, 71, 5340-5347.

20) Papautsky, I.; Brazzle, J.; Ameel, T.; Frazier, A. B. *Sens. Actuat. A: Phys.* **1999**, 73, 101-108.

Chapter 4.

Photocyanation of Pyrene at Liquid/Liquid Interface in Polymer Microchannel Chips

4.1 Introduction

As described in Chapter 3, it was demonstrated that liquid/liquid extraction of a solute could be achieved very efficiently along solution-flow in a microchannel and was also shown to be controlled by diffusion of the solute across the liquid/liquid interface in a microchannel, a solution-flow velocity, and channel geometries. Under laminar flow conditions, a stable oil/water interface can be produced and the two-phases are separated even at the exit channel junction of the chip. It is easily expected that, therefore, a liquid/liquid interfacial reaction and subsequent extraction of the reaction product(s), both governed by diffusion of the solute, will be conducted efficiently along solution-flow in a microchannel. If this is the case, such a system can be applied to an automated chemical reactor.

In order to test this idea, photocyanation of pyrene (PyH) across an oil/water interface was explored by using a polymer microchannel chip as an example for an interfacial photoreaction. According to the reports by Kitagawa et al. on the photocyanation reaction of pyrene in oil-in-water emulsion systems,[1-3] namely, it is anticipated that the following photoreaction would proceed in a microchannel (see Scheme 4-1). Under laminar flow of an aqueous NaCN solution and an immiscible oil containing PyH and an electron acceptor (A) in a microchannel, photoinduced electron transfer (PET) between PyH and A takes place in the oil phase.[4-7] The cation radical of PyH would be then subjected to nucleophilic attack by a cyanide ion at the oil/water

interface or in the water phase, producing the cyanated product (PyCN).[1,2] If the solubility of PyCN in water is very poor, PyCN will be distributed to the oil phase along solution-flow in the microchannel (i.e., extraction). In practice, it was demonstrated that the cyanation yield of PyH increased with a decrease in a droplet size through the increase in the surface area/volume ratio of a droplet.[3] This supports explicitly that the overall reaction involves an oil/water interfacial process(es). Since an oil/water interface can be produced easily in a microchannel, analogous interfacial photocyanation reaction of PyH via a PET mechanism with that in the emulsion system is expected to proceed efficiently in a channel chip as illustrated in Scheme 4-1. In the present study, the photoreaction was performed by using two types of a polystyrol microchannel chip: double Y-structured (two-layer channel) and three-layer channel chips (three-layer channel), and effects of a solution-flow velocity and the channel geometry on the reaction yield are discussed.

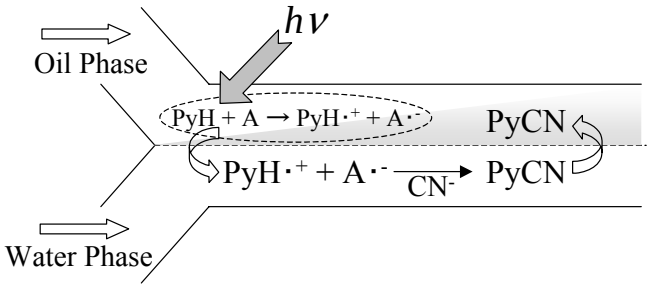

Scheme 4-1 Photocyanation reaction of PyH in a microchannel. A represents 1,4-dicyanobenzene.

4.2 Experimental

4.2.1 Chemicals and Sample Preparations

Pyrene (PyH, Wako Pure Chemical Ind. Ltd.) and 1,4-dicyanobenzene (DCB, Wako Pure Chemical Ind. Ltd.) as an electron acceptor for PET were purified by repeated recrystallizations from ethanol. The structural formulas of PyH and DCB are shown in Figure 4-1. Propylene carbonate (PC, Tokyo Kasei Kogyo Co. Ltd., GR grade) was used as an organic phase for the photoreaction, since PC was inert to a polystyrol substrate and suitable for PET due to its high dielectric constant (ε = 64.9 at 298 K).[8] Water was purified by distillation and deionization prior to use (GSR-200, Advantec Toyo Co.). For photoreaction experiments, water and PC were saturated with PC and water, respectively. The concentrations of PyH and DCB in PC were set at 20 and 40 mM, respectively, while that of NaCN (Wako Pure Chemical Ind. Ltd.) in water was set at 1 M throughout the study.

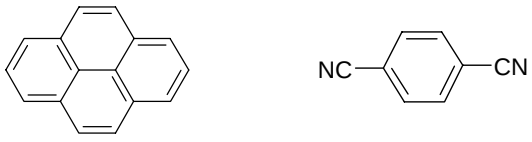

PyH DCB

Figure 4-1 The structural formulas of PyH and DCB.

4.2.2 Experimental Setup

Polymer microchannel chips used in the present study were fabricated by using silicon templates, whose fabrication method was described in Chapter 3. The overall

structural layouts of the microchannel chips used are shown in Figure 4-2. One of the chips allows two-layer (oil/water) flow in the microchannel, whose dimension is set 100 μm width, 20 μm depth, and 350 mm total length (from entrance to exit junction, Figure 4-2 (a)). The other is a three-layer type channel chip, which allows a water/oil/water or oil/water/oil stream in the microchannel (Figure 4-2 (b)). The dimension of the channel was the same with that of the two-layer channel chip. The scanning electron microscope (SEM) image of the silicon template (a) and an optical microscope image of the polystyrol substrate (b) shown in Figure 4-3 indicated that the microchannel was fabricated successfully on the polystyrol substrate.

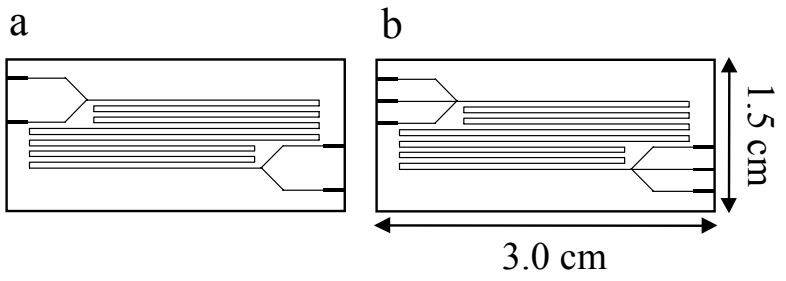

Figure 4-2 Schematic drawings of channel designs: two-layer channel (a) and three-layer channel chips (b).

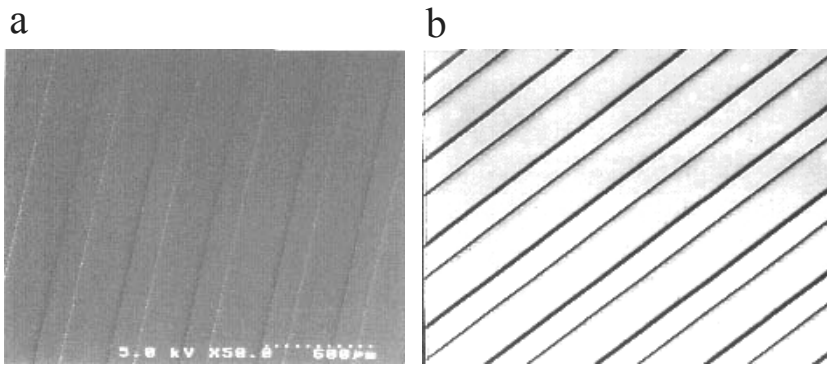

Figure 4-3 Scanning electron microscope image of the silicon template (a) and a microscope image of the polystyrol substrate (b).

Analogous solution-flow system with that described in Chapter 2 was employed in the present experiments. Two 100 μl-volume syringes, one being filled with a PC solution of PyH and DCB and the other with an aqueous NaCN solution, were equipped with a programmable dual-syringe pump. The two fluids were introduced to the channel chip with the same flow velocity throughout the work. For photocyanation of PyH, light from a 300 W high-pressure mercury lamp being passed through a $CuSO_4$ solution filter (> ~330 nm) was irradiated onto the whole of the channel chip after formation of a stable oil/water interface in the channel as confirmed by observation under a microscope (Nikon, Optiphoto-2). For product analysis, the oil phase was collected from the exit of the microchannel and analyzed by GC-MS (Shimadzu Co., QP-5050). The absolute yield of 1-cyanopyrene (PyCN) as the product of the photoreaction was determined on the basis of a calibration curve obtained by GC analysis using an authentic PyCN.

4.3 Results and Discussions

4.3.1 Photocyanation of PyH in Two-Layer Type Polymer Microchannel Chip

An aqueous NaCN solution (1 M) and a PC solution of PyH (20 mM) and DCB (40 mM) were introduced separately to the double Y-type channel chip (Figure 4-2 (a)) with the same flow velocity (u = 0.2 μl min^{-1}), and the whole of the chip was irradiated at > ~330 nm. Figure 4-4 (a) shows the gas chromatograms of the oil phase before (dotted line) and after the photoreaction (solid line), whose samples were collected from the exit of the microchannel. It is seen clearly that a decrease in the peak intensity of

PyH at a retention time (t_r) of 11.8 min upon photoirradiation accompanies an appearance of a new peak at t_r = 13.0 min. The t_r value agreed very well with that of authentic PyCN, and the mass number of the compound at t_r = 13.0 min was 227 (=PyCN), as the spectrum was shown in Figure 4-5 (a). On the other hand, no peak was observed for the chromatogram of the water phase as long as the t_r region studied (Figure 4-4 (b)). Furthermore, it was confirmed that PyCN was not produced in the absence of NaCN in water, indicating that the CN source of the photoreaction was not DCB. On the basis of these results, it is concluded that the photocyanation reaction of PyH proceeds across the PC/water interface in the microchannel as illustrated in Scheme 4-1. It is worth emphasizing, furthermore, that PyCN is obtained exclusively from the oil phase, demonstrating that PyCN is extracted completely to the PC phase during two-phase laminar flow in the microchannel. As long as observation was made under a microscope, in practice, the two-phases were separated completely even at the exit of the microchannel, as the photograph was shown in Figure 4-5 (b). The present microchannel chip can be thus used as an automated photochemical microreactor: photoreaction-extraction system.

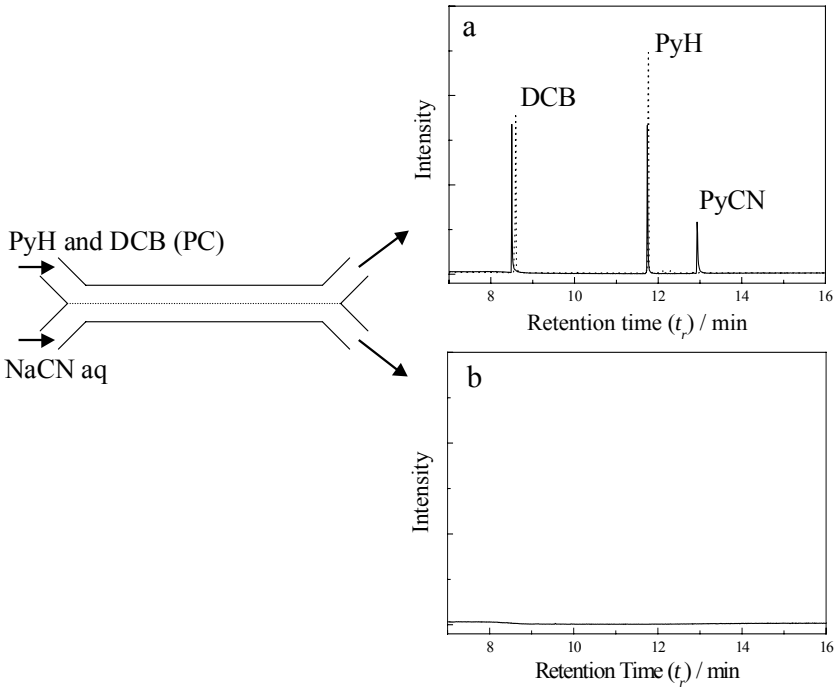

Figure 4-4 Gas chromatograms of the oil phases before (dotted line) and after the photoreaction (solid line, (a)), and that of the water phase after the photoreaction.

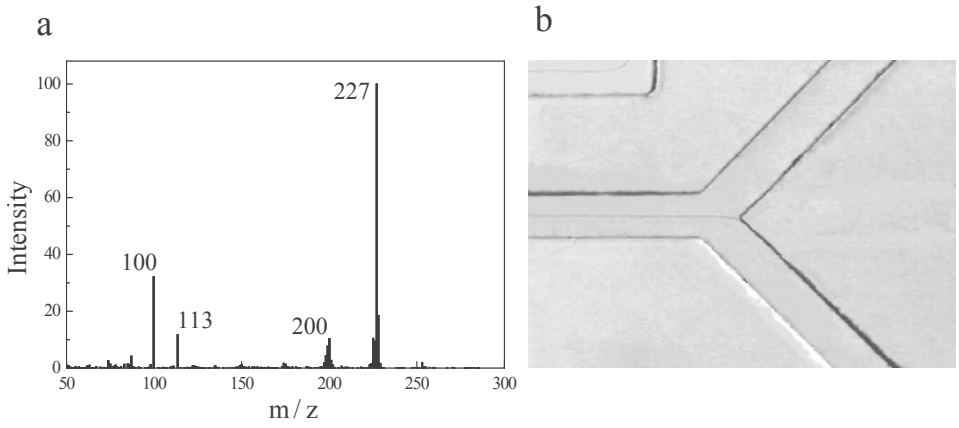

Figure 4-5 (a) The mass spectrum for the gas chromatogram peak at t_r = 13.0 min in Figure 4-4 (a). (b) A microscope image near the exit junction of the microchannel chip.

The calibration curve for PyCN made by a separate experiment indicates that the absolute PyCN yield under the conditions mentioned above is 28%, which is not necessarily high enough. The factors determining the yield should be thus considered. One of the factors is transparency of the polystyrol substrate. The percent transmittance (*T%*) spectrum of a polystyrol substrate is shown in Figure 4-6. The substrate is almost transparent in the wavelength (λ) region longer than 370 nm (*T%*: ~90%), while *T%* of the substrate decreases sharply at $\lambda < 370$ nm. Since PyH shows a strong absorption band (the second singlet excited state) at around 340 nm, incident light flux absorbed by PyH is not necessarily high enough, leading to a low reaction yield. Since the reaction quantum yield has not been determined, further details on this point cannot be discussed, which is a future target of the study.

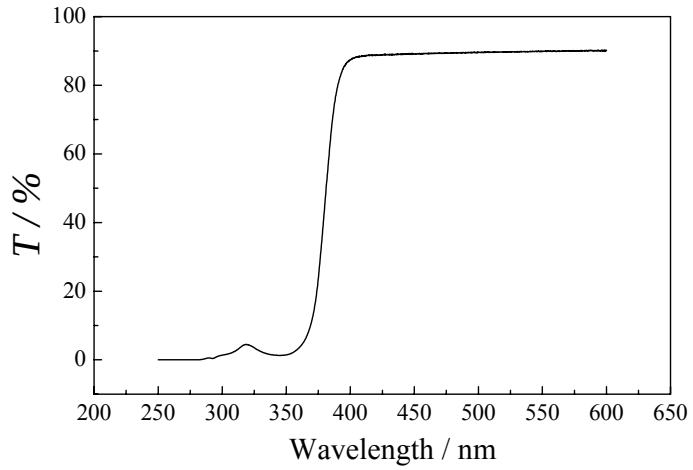

Figure 4-6 The percent transmittance (*T%*) spectrum of a polystyrol substrate.

In the present system, the reaction time is determined by the contact time (*t*) between the two phases in the microchannel; *t* = channel length (*l* = 350 mm) / average

linear flow velocity (u mm s^{-1}). At u = 0.2 μl min^{-1}, t is calculated to be 210 s. Although the reaction yield of 28% is not high enough, the photocyanation reaction proceeds as short as 210 s. Analogous experiments with those shown in Figure 4-4 were also performed at different u to elucidate the relationship between t and the reaction yield. The t dependence of the absolute yield is summarized in Figure 4-7. The results demonstrated clearly that the reaction yield increased linearly from 7 to 28% with t increasing from 70 to 210 s. This implies that the photocyanation reaction of PyH can be controlled by the solution-flow velocity in the microchannel. Also, the results indicate explicitly that diffusion of the reaction intermediate (probably be the cation radical of PyH) toward the oil/water interface governs the cyanation yield. These are the characteristics of the present reaction in a microchannel.

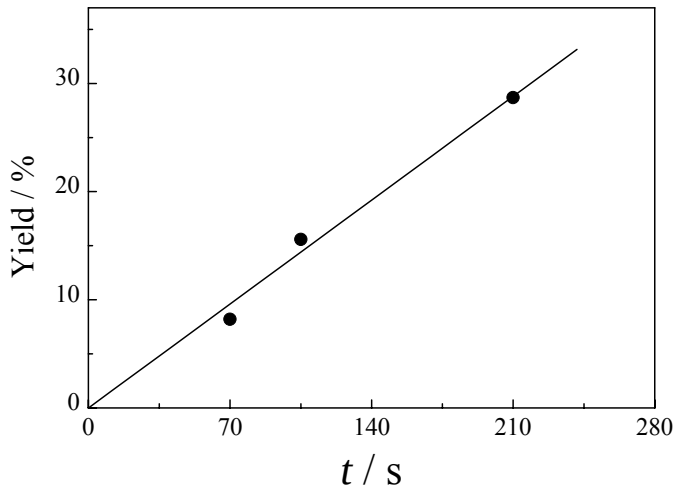

Figure 4-7 Contact time (t) dependence of the absolute PyCN yield observed for the two-layer channel.

The results in Figure 4-7 indicate that an increase in the contact time between the two phases can improve the reaction yield. Therefore, a double-decker type channel chip was also fabricated by laminating two of the two-layer type channel substrate as illustrated in Figure 4-8. The photocyanation yield of PyH in the double-decker type channel chip was determined to be 48% (u = 0.2 μl min^{-1}, t = 420 s), which was less than two times of the value by the two-phase channel chip (28%, u = 0.2 μl min^{-1}, t = 210 s). Since photoirradiation was conducted from the one side of the chip and the polystyrol substrate itself absorb slightly above 365 nm, the lower reaction yield for the integrated chip as expected from the reaction time of 420 s will be due to a lower incident light intensity absorbed by PyH in the channel opposite to the Hg lamp. Optimization of a photoirradiation system could improve further the reaction yield.

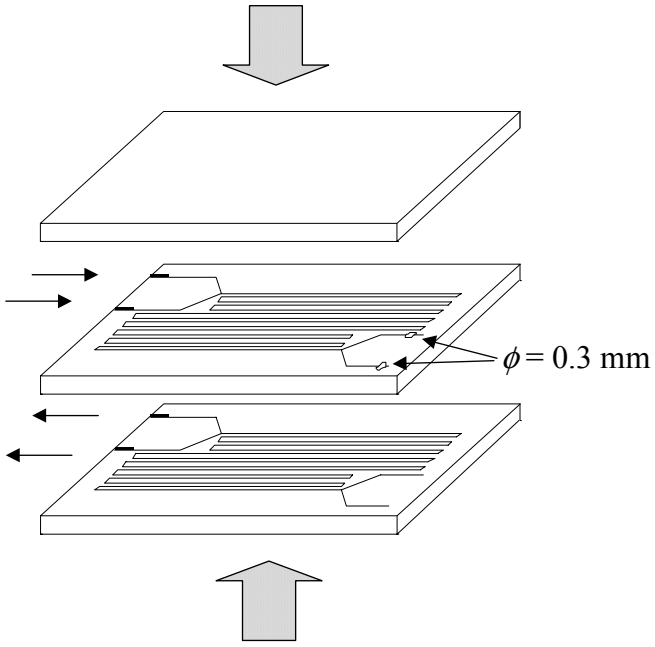

Figure 4-8 Schematic illustration of a double-decker type microchannel chip.

4.3.2 Photocyanation of PyH in Three-layer Type Polymer Microchannel Chip

The results in Figure 4-7 also indicate that the specific interfacial area between the water and PC phases determines the photocyanation yield in the microchannel system. The photocyanation reaction in a water/oil/water three-layer type microchannel chip (Figure 4-2 (b)) would improve further the reaction yield. Therefore, such an experiment was explored to attain a higher photocyanation efficiency. The microscope image of three-layer (water/oil/water) laminar flow observed near the entrance channel junction is shown in Figure 4-9 (a). Three layers produced at the junction were confirmed to run parallel with one another to the channel outlet without turbulence and mutual mixing.

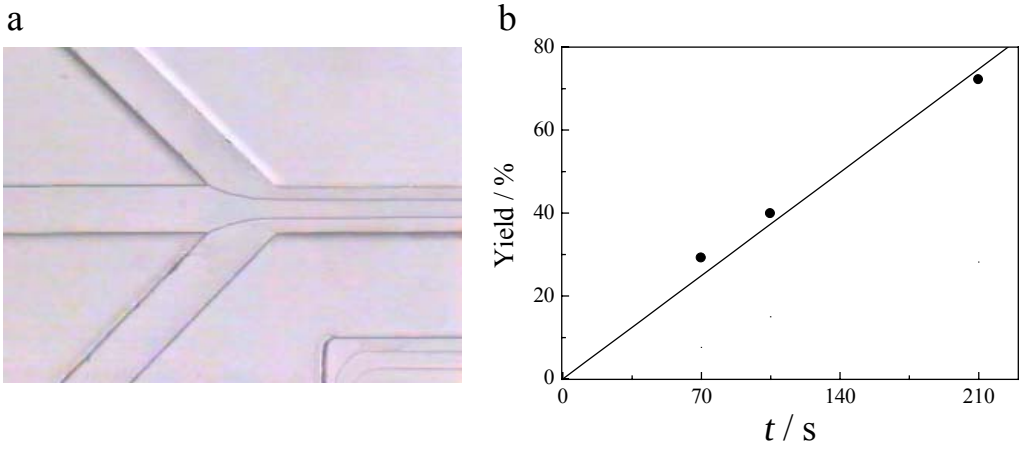

Figure 4-9 Photocyanation reaction of PyH in a three-layer microchannel chip. A microscope image of three-layer laminar flow (water/oil/water) around the entrance channel junction (a) and the contact time (*t*) dependence of the absolute PyCN yield (b).

The results by the three-layer chip are summarized in Figure 4-9 (b), as the contact time (t) dependence of the absolute PyCN yield. As in the case of the two-layer channel chip in Figure 4-7, the yield increased almost linearly with t and the absolute PyCN yield of 73% was attained at u = 0.2 μl min^{-1} and t = 210 s, whereas the relevant value in the two-layer channel chip was 28% (Figure 4-7). The slope values in Figures 4-7 and 4-9 indicate that the yield in the three-layer channel chip is ca. 3.0 times higher than that in the two-layer channel chip at given t. In the case of these microchannel chips with the same geometry (width = 100 μm, depth = 20 μm, and length =350 mm), it is worth noting that the specific interface area (ratio of an oil/water interfacial area to the volume of an oil, A/V) between the oil and water phases in the three-layer channel chip is three times larger than that in the two-layer channel chip. The importance of the A/V ratio was also confirmed by the photoreaction under an oil/water/oil stream in the channel. Although data are not shown here, the PyCN yield by an oil/water/oil stream at a given flow velocity was almost half of the relevant value obtained under the water/oil/water stream in Figure 4-8. This is easily understood by the fact that the volume of the PC phase in the oil/water/oil system is two times larger than that in the water/oil/water stream system. Therefore, the higher reaction yield in the three-layer channel chip compared to that in the two-layer chip is concluded to be due to the larger specific interfacial area in the three-layer chip. In the case of an interfacial reaction, the product yield and the reaction time are manipulated arbitrarily by the channel structures, a flow velocity, and so forth, which is very important characteristics of a synthetic reaction in a microchannel.

4.4 Conclusion

Photocyanation of pyrene across an oil/water interface via a photoinduced electron transfer mechanism was shown to proceed very efficiently in a polymer microchannel chip and, the absolute PyCN yield as high as 73% was attained by the three-layer channel chip with the reaction time of 210 s. As characteristics of an interfacial photoreaction in a microchannel chip, furthermore, it was demonstrated that the yield was proportional to the contact time between the two fluids as shown by the flow velocity dependence of the yield as in the case for the extraction experiments described in Chapter 3. This implies that the reaction yield can be controlled arbitrarily by the flow velocity, the channel geometry, and the channel length. Recovery of unreacted PyH indicates that a slower solution-flow velocity will improve further the reaction yield. Nonetheless, a slower u than 0.2 μl min^{-1} did not produce a stable oil/water stream in the microchannel. It is expected that optimization of the total channel length is another way to improve the reaction yield. Besides the present interfacial photoreaction, polymer microfluidic channel chips can be applied to various reaction systems on the basis of integration of the channel system with microelectrodes, microheaters, and so on as described in the following chapters.

4.5 References

1) Kitagawa, F.; Murase, M.; Kitamura, N. *Chem. Lett.* **2001**, 786-787.

2) Kitagawa, F.; Murase, M.; Kitamura, N. *J. Org. Chem.* **2002**, 67, 2524-2531.

3) Kitagawa, F.; Kitamura, N. *Phys. Chem. Chem. Phys.* **2002**, 4, 4495-4503.

4) Grellmann, K. H.; Watkins, A. R.; Weller, A. *J. Phys. Chem.* **1972**, 76, 469-473.

5) Schombug, H.; Staerk, H.; Weller, A. *Chem. Phys. Lett.* **1973**, 22, 1-4.

6) Majima, T.; Pac, C.; Nakasone, A.; Sakurai, H. *J. Am. Chem. Soc.* **1981**, 103, 4499-4508.

7) Fossum, R. D.; Fox, M. A. *J. Phys. Chem. B* **1997**, 101, 6384-6393.

8) Izutsu, K. *Denki Kagaku* **1980**, 48, 530-544.

Chapter 5.

Characteristic Electrochemical Responses in Polymer Microchannel Chips Integrated with Microband Electrodes

5.1 Introduction

It was shown that channel dimensions and geometries could control both the liquid/liquid extraction efficiency and the interfacial photochemical reaction yield in a microchip as described in Chapter 3 and 4. This implies that mass-transfer of a solute in a microchannel is affected by the presence of the channel wall, the channel size, solution flow characteristics, and the specific surface (interface) area. In Chapter 1, on the other hand, studies on electrochemical reactions in a minute space were overviewed and the characteristics of the responses were described briefly. As an example, the electrochemical responses of an electrode in a microchannel are considered approximately to be similar to those in a thin layer cell, since the channel depth is generally very shallow: ~10 μm. Thin-layer cell type electrochemical behaviors are observed, when the cell walls prevent the lateral expansion of the diffusion field around an electrode and complete depletion of the reactants occurs. It means that the electrochemical responses in a channel are predicted to be different from those in the thin-layer cell behavior despite of a shallow channel depth, since the lateral dimension of a channel along the solution-flow direction is very long in comparison with the diffusion layer of a redox specimen. Therefore, the electrochemical responses of an electrode in a microchannel are worth exploring in detail. In particular, a study on the electrochemical characteristics under solution-flow conditions plays important roles in the development of microchip electrochemical detection devices.

In order to pursue the present study, a microchannel-electrode chip, on which a microband electrode(s) with an arbitrary pattern and size was positioned in a channel, was fabricated and the electrochemical behaviors of the electrode(s) were studied in detail. In this chapter, a new and novel fabrication method of polymer microchannel chips integrated with microband electrodes is described. One of the primary purposes of the study is to demonstrate that the electrochemical responses can be controlled by the channel geometries and a solution-flow velocity. Characteristic and unique electrochemical responses of the fabricated channel-electrode chip are demonstrated by several modes of an electrochemical measurement: cyclic (linear sweep) voltammetry, chronoamperometry, and generation-collection mode experiments. To discuss the electrode responses, furthermore, the experimental results were compared with those predicted by numerical simulations.

5.2 Experimental

5.2.1 Chemicals and Sample Preparation

1-Hydroxyethylferrocene (FeCp-OH, Tokyo Kasei Kogyo Co. Ltd., EP Grade) was used in the present study. The structural formula of FeCp-OH is shown in Figure 5-1. Water was distilled and deionized by a Mili-Q Labo system. Potassium chloride (KCl, Wako Pure Chemical Ind. Ltd., GR grade) was used as a supporting electrolyte. The final concentrations of FeCp-OH and KCl were 1.0×10^{-3} M and 0.1 M, respectively.

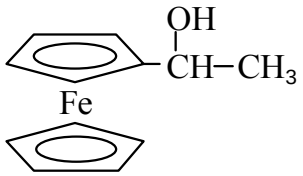

Figure 5-1 The structural formula of FeCp-OH

5.2.2 Fabrication and Structures of Polymer Microchannel-Microelectrode Chips

A fabricated polymer microchannel chip was composed of channel and electrode substrates. Commercially available polystyrol substrates (1.5 x 3.0 cm) were used as a channel-electrode chip material as described in Chapter 2. A template for imprinting was prepared with a glass or silicon substrate on the basis of photolithography. In the present study, a silicon template described in Chapter 3 was used for fabricating a channel substrate. The silicon template and a polystyrol substrate were fastened tightly between two glass plates and heated at 110 °C for 25 min to transfer the embossed structure to the polymer plate. The geometry of the rectangular microchannel was a straight line with the overall length of 6 cm, width of 100 μm, and depth of 20 μm.

On the other hand, an electrode substrate was fabricated as follows. The scheme of the fabrication processes is shown in Figure 5-2. First, a gold thin-film (thickness 100 nm) was vacuum-deposited directly onto a polystyrol substrate (5.0 x 10^{-6} Torr). The Au/polymer substrate was then annealed in an oven at 110 °C for 30 min, in which the annealing temperature was set just above the glass transition temperature of the polymer substrate (~108 °C). Annealing was very important to fabricate a tough Au film on the substrate.

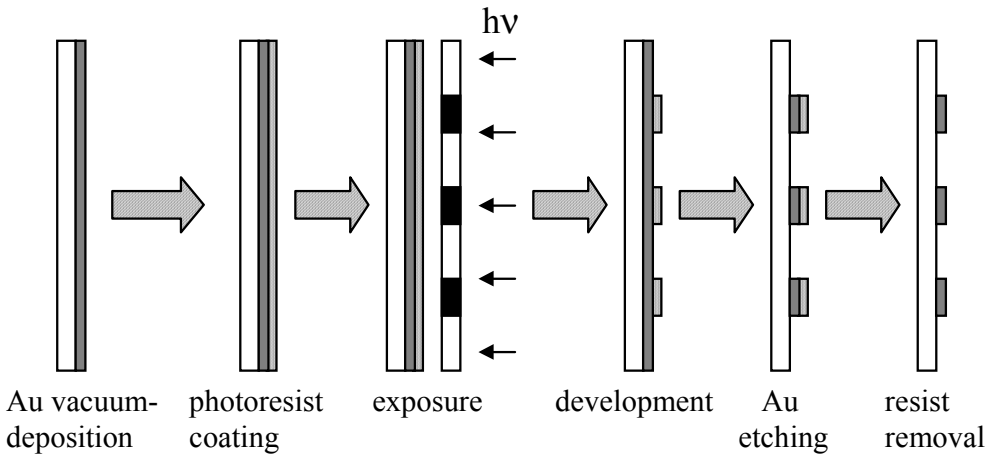

Figure 5-2 The schematic drawing of the fabrication processes of an electrode substrate.

To fabricate microelectrodes, a photoresist employed in Chapter 2 was spin-coated on the Au/polymer substrate. In the present experiment, pre-bake of the resist layer was not carried out because adhesitivity between the photoresist and the substrate was good. The resist layer was exposed to a 300 W tungsten-lamp through a photomask, whose structure was drawn on a transparency film by a computer software package and a 2400 dpi printer. The resist layer was developed by a developer (Tokyo Ohka Co. Ltd., NMD-3). After rinsing with pure water, the exposed Au layer was etched in an aqueous I_2 (1.5 g) / NH_4I (8 g) solution (100 ml) at 50 °C for 5 s. The fabricated Au band microelectrodes were employed as working (WE) and counter electrodes (CE). For integration of a reference electrode (RE, width = 200 μm), a silver thin layer (~100 nm) was vacuum-deposited directly onto the Au electrodes/polymer substrate through a plastic mask as illustrated in Figure 5-3 (a).

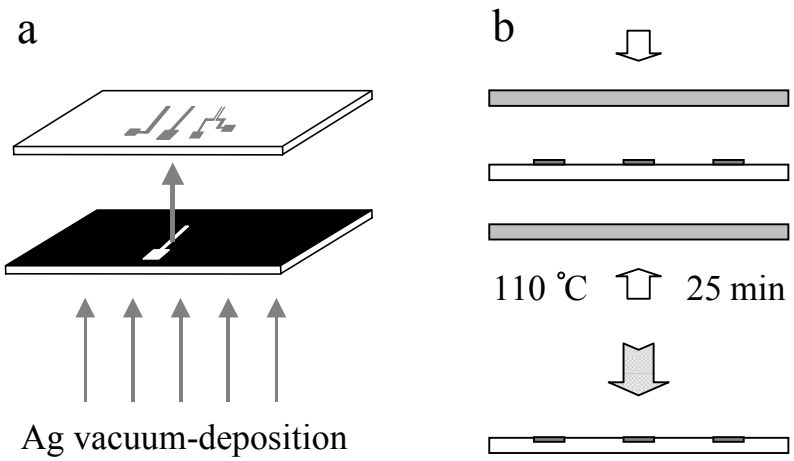

Figure 5-3 (a) Illustration of a fabrication process of a reference electrode (Ag electrode) onto the polymer WE/CE-electrode substrate by vacuum-deposition. (b) The schematic drawing of burying the Au-Ag electrodes into the polymer substrate.

It is worth noting that the ultimate thickness of the Au and Ag electrodes might influence solution-flow characteristics in a microchannel, when the electrode substrate is bonded with the channel substrate. Furthermore, the thickness of the electrode on a substrate makes difficult to bond with a cover substrate. Therefore, the Au-Ag/polymer substrate was clamped between two glass plates and heated at 110 °C for 25 min to bury the electrodes into the polymer substrate to minimize disturbance of solution-flow as well as allow to bonding the two substrates as illustrated in Figure 5-3 (b). Finally, the electrode substrate was covered and bonded with the channel substrate by pressing the two substrates between glass plates at 110 °C for 18 min. The spatial geometries of the electrodes were designed so as to each electrode being positioned perpendicular to the channel direction as illustrated in Figure 5-4.

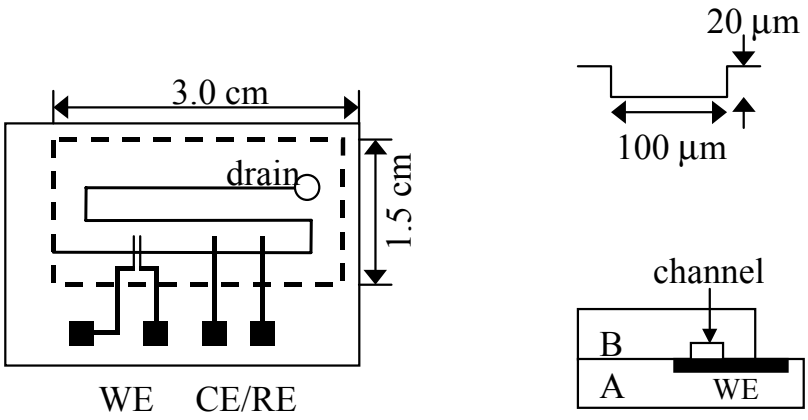

A: electrode-substrate, B: channel-substrate

Figure 5-4 Illustration of a polymer microchannel chip integrated with microband electrodes. WE: working electrode, CE: counter electrode, and RE: reference electrode.

The photographs of the dual-band working electrodes in the polymer microchannel chip are shown in Figure 5-5. As shown in Figure 5-5 (a), bonding pads for connection with an external electrochemical apparatus were also fabricated. It is confirmed from Figure 5-5 (b) that the dual-band electrodes are positioned vertically to the microchannel (the width 100 μm) as mentioned before. The edge of the electrode is not necessarily straight. It is supposed that this is due to the resolution of the photomask used. The width of each working electrode was 47 μm and the distance between the dual-band electrodes was designed as 68 μm. The spatial geometries of the dual-band electrodes were shown schematically in Figure 5-5 (c).

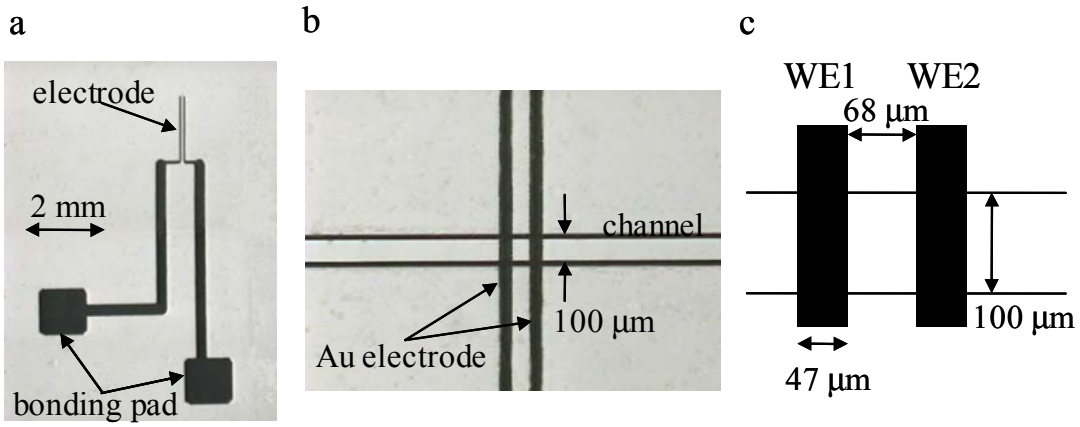

Figure 5-5 The photographs of the working electrodes and the sizes of the dual-band electrodes: The whole image of the working electrode (a), the image of the dual-working electrodes (b), and schematically drawing of the spatial sizes of the dual-electrodes (c).

5.2.3 Experimental Setup

A block diagram of the solution-flow and electrochemical measurement systems used in this study is illustrated in Figure 5-6. Analogous solution-flow system with that described in Chapter 2 was used in the present study. A 50 μL volume-syringe, being filled with an aqueous FeCp-OH solution containing KCl, was equipped with a syringe pump. The channel-electrode chip was connected with an electrochemical analyzer (ALS Co., Ltd., model 701A) through lead wires from the bonding pads as shown in Figure 5-5 (a). A connection between the bonding pad and lead wire was made by a silver paste as an electroconductive adhesive, and they were fixed with an epoxy resin.

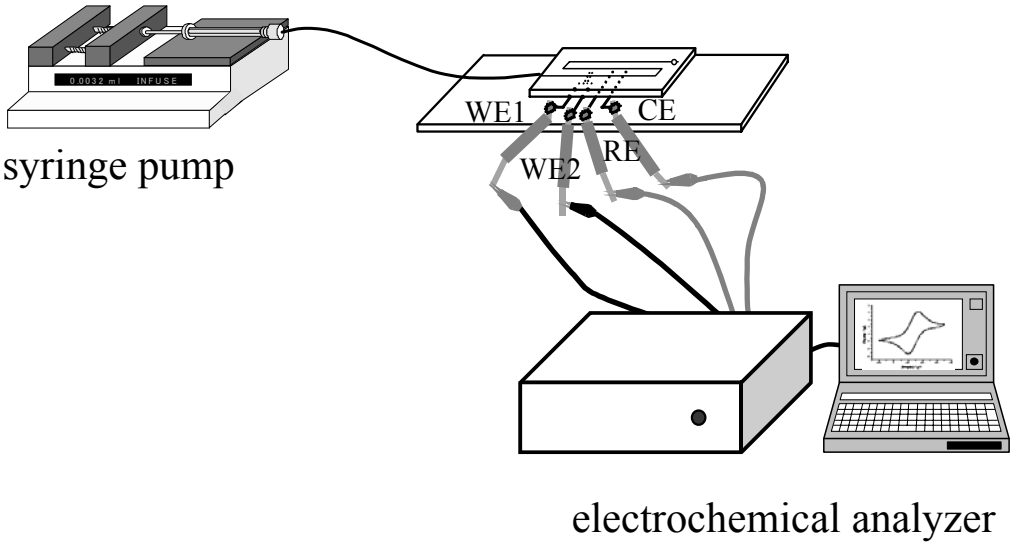

Figure 5-6 A block diagram of the solution-flow and the electrochemical measurement system used in the present study.

5.2.4 Numerical Simulations of Electrochemical Responses

In order to discuss both experimental results and the performances of the microchannel-microelectrode chip, numerical simulations of the electrochemical responses in the chip were performed on the basis of a finite element method (FEM) by using a computer software package (PDEase 2D, Macsyma Inc.). Although three-dimensional analyses of the concentration profile at a microdisk electrode are necessary, two-dimensional analyses have been conducted since the concentration profile along the direction of the electrode-length (equal to the channel width) is identical. Considering a simple redox reaction as in the case for that of ferrocene without migration and convection, the concentration profile of a redox specimen can be calculated on the basis of the Fick's second law: eq. (5-1).[1-5]

$$\frac{\partial C_R}{\partial t} = D_R \nabla^2 C_R \qquad (5\text{-}1)$$

Where ∇^2 is the Laplacian operator, and that for an inlaid band electrode is given by the following equation:

$$\nabla^2 = \frac{\partial^2}{\partial x^2} + \frac{\partial^2}{\partial z^2} \qquad (5\text{-}2)$$

For the calculations, the following initial and boundary conditions were assumed,

Initial Conditions

$$\text{at} \quad t = 0 \quad C_R = C_R{}^0, \quad C_O{}^0 = 0 \qquad (5\text{-}3)$$

Boundary Conditions

$$\text{at} \quad t > 0 \quad \frac{C_R}{C_R{}^0} = \frac{\theta e^{-\gamma}}{1+\theta^{-\gamma}} \quad \text{with} \quad \theta = e^{nF/RT(E_i - E^0)} \quad \gamma = \frac{nF}{RT}\nu \qquad (5\text{-}4)$$

$$\text{at} \quad t > 0 \quad \text{at the channel wall} \quad \left[\frac{\partial C_R}{\partial N}\right]_{wall} = 0 \qquad (5\text{-}5)$$

where C_R and C_O are the concentrations of reduced (R, $C_R{}^0$ = 1.0 x 10^{-6} mol dm^{-3}) and oxidized species (O), respectively. D_R and D_O are the diffusion coefficients of R and O (D_R = D_O = 2.8 x 10^{-6} cm^2 s^{-1}), respectively. E_i and E^0 are the initial and formal potentials, respectively, and t is a time. F, R, T, and ν are the number of an electron transferred (n = 1 in the present case), the Faraday constant (C mol^{-1}), the gas constant (J mol^{-1} K^{-1}), a temperature (298 K), and a potential sweep rate (V s^{-1}), respectively. N is the length from the channel wall and taken as normal to the wall. A current at an electrode (i (t)) was then simulated as time-dependent flux of FeCp-OH at the electrode

as given by eq. (5-6).

$$i(t) = nFD_R\left[\frac{\partial C_R(x,t)}{\partial x}\right]_{x=0} \qquad (5\text{-}6)$$

Under solution-flow conditions, on the other hand, the flow profile along the direction of the channel depth (*z*-axis) is parabolic, while that along the channel width (*y*-axis) is plug-like, since the aspect ratio of the present microchannel is small: z (20 μm)/y (100 μm) as described in Chapter 3. Therefore, the flow velocity along the *y*-axis is assumed to be almost constant, while that along the *z*-axis depends on the depth-position in the microchannel. Consequently, the numerical simulation can be simplified and conducted by a two-dimensional approximation, since the flow profile along the *y*-axis is not a parameter. The flow profile along the *z*-axis was then simulated by the Navier-Stokes equation, which was considered to simulate $i(t)$ under solution-flow conditions in the microchannel.

5.3 Results and Discussions

5.3.1 Electrochemical Responses of the Microelectrode in Polymer Microchannel Chip

Cyclic voltammograms (CV) of FeCp-OH observed in the microchannel at several sweep rates are shown in Figure 5-7. The CV was measured without solution-flow. In the experiments, one of the dual Au electrodes was used as WE. It is well known that the electrochemical response of a microband electrode is best characterized by hemi-cylindrical diffusion and, in practice, the quasi-steady state currents were observed in the voltammograms.[6-10] In the case of a band electrode, furthermore, the shape of a

voltammogram is governed by the electrode width and, when the electrode width is small compared to the thickness of a diffusion layer and ν is very slow, the voltammongram becomes a sigmoidal shape. Nonetheless, the CV measured in the microchannel is not sigmoidal, but exhibits a peak potential similar to that obtained by an ordinary millimeter-sized electrode. Therefore, the electrochemical response of the band electrode in the microchannel was characterized by a semi-infinite diffusion. For the experiments, voltammetry was conducted under aerated conditions. Therefore, the anodic current by O_2 reduction was observed in the potential region negative than 0 V. Since this is not a main issue of the present study, the anodic current is neglected in the following discussions.

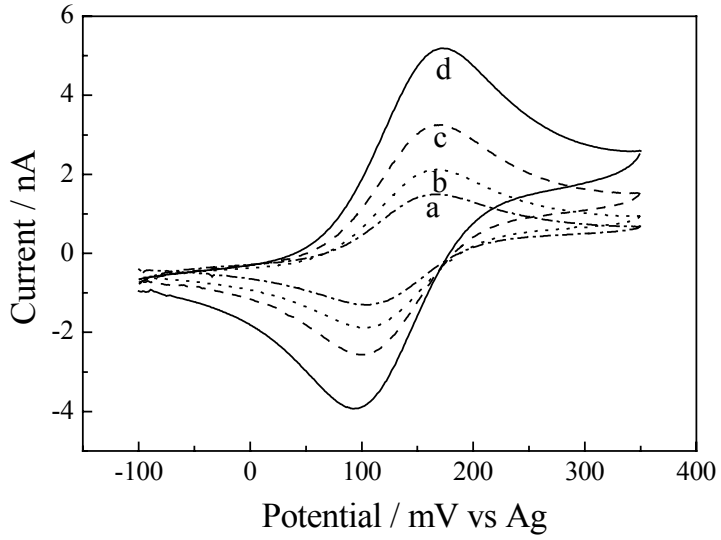

Figure 5-7 Potential sweep rate (ν) dependence of the cyclic voltammogaram of FeCp-OH (vs. Ag); ν = 5 (a), 10 (b), 20 (c), and 50 mV s^{-1} (d).

The potential sweep rate dependence of the peak current is shown in Figure 5-8. The peak current (i_p) increased linearly with $\nu^{1/2}$, indicating one-dimensional linear diffusion response of the electrode in the channel, as given by the following classical equation,[11]

$$i_p = 0.4463\ nFAC_R^0(nF/RT)^{1/2}n^{1/2}D_R^{1/2} \qquad (5\text{-}7)$$

where A is the electrode surface area. Since the channel depth is 20 μm, a thin layer cell type response might be expected ($i_p \sim \nu$) as mentioned in Chapter 1. However, this was not the case in the present experiments, since the lateral dimension of the channel was very large in comparison with the band-electrode width. Thus, a semi-infinite diffusion field in the direction of channel is dominant. This is general characteristics of a band-electrode in a microchannel.

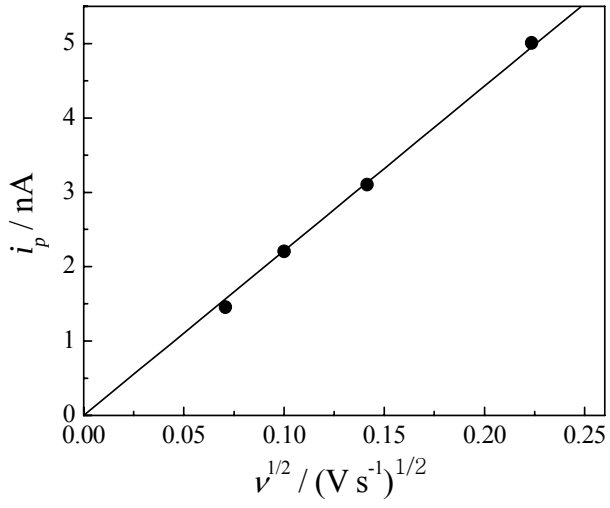

Figure 5-8 The potential sweep rate (ν) dependence of the peak current (i_p).

The electrode area calculated by the slope of the plot in Figure 5-8 and the equation 5-7 (4.9 x 10^{-5} cm^2) agreed very well with that determined from the electrode dimension (4.7 x 10^{-5} cm^2) shown in Figure 5-5 (c). This demonstrates that one-dimensional diffusion model can be applied to the electrode response in the microchannel, and the correct response of the fabricated electrode was confirmed.

On the other hand, linear sweep voltammograms of FeCp-OH at several potential sweep rates were measured with the microchannel chip and the electrode substrate (without a channel cover) under non solution-flow conditions, and the results were shown in Figure 5-9. The oxidation potentials of FeCp-OH determined by the channel chip (Figure 5-9 (a)) and the electrode substrate (Figure 5-9 (b)) were 164 and 161 mV (vs. Ag), respectively, which agreed very well with the value determined by a conventional disk electrode; 163 mV (vs. Ag). In the case of the electrode substrate (Figure 5-9 (b)) at ν = 5 mV s^{-1}, the sigmoidal voltammogram demonstrates that the thickness of the diffusion layer is large compared to the electrode width. Even at the same sweep rate, on the other hand, the shape of voltammogram observed by the channel chip (Figure 5-9 (a)) was different from that in Figure 5-9 (b) and the voltammogram showed a clear peak irrespective of ν. These behaviors are very similar to a current-potential curve observed for one-dimensional linear diffusion as mentioned above. Clearly, the presence of the microchannel wall above the electrode influences the diffusion profile and, thus, the electrode responses. In order to understand these results in more detail, numerical simulations of the responses were conducted.

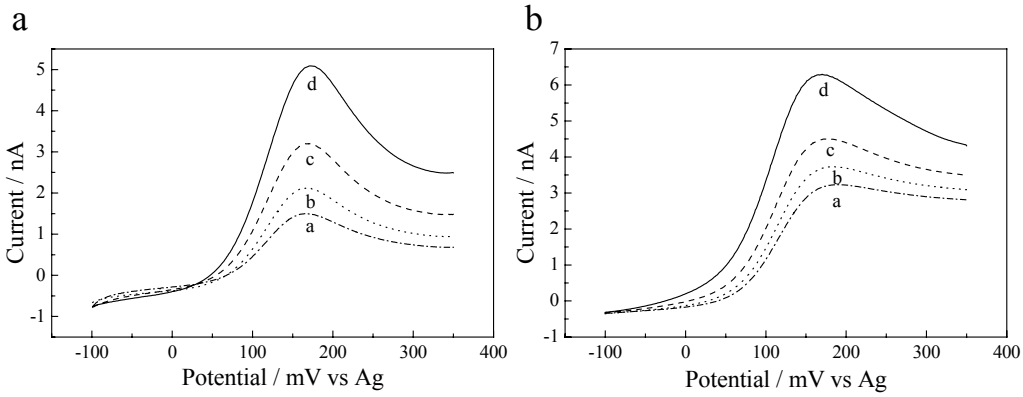

Figure 5-9　Linear sweep voltammograms of FeCp-OH observed by the channel chip (a) and the electrode substrate (without a channel cover, b) at ν = 5 (a), 10 (b), 20 (c), or 50 mV s^{-1} (d).

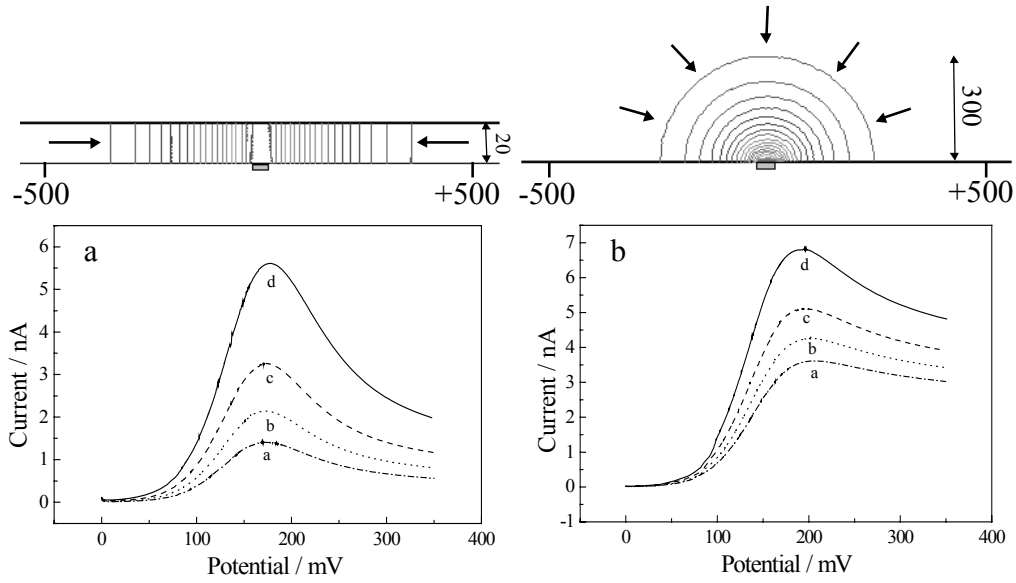

Figure 5-10　Simulated linear sweep voltammograms and the relevant concentration profiles (upper traces) of FeCp-OH predicted for the microchannel (a) and the electrode substrate (b). For the voltammograms, the sweep rate was 5 (a), 10 (b), 20 (c), or 50 mV s^{-1} (d). The concentration profiles are the results at 90 s after the start of the potential sweep (ν = 5 mV s^{-1}) from 0 to 450 mV.

The simulated voltammograms and the relevant concentration profiles of the FeCp-OH cation generated at the electrode in the channel chip (a) or on the substrate (b) are shown in Figure 5-10. The concentration profiles shown by the contour lines or curves are the results at 90 s after the start of the potential sweep (ν = 5 mV s^{-1}) from 0 to 450 mV. In the case of the electrode substrate (Figure 5-10 (b)), hemi-cylindrical diffusion of the FeCp-OH cation takes place at the electrode and this gives the voltammograms in the lower panel, which reproduces very well the observed ones in Figure 5-9 (b). For the microchannel chip, on the other hand, the simulations predict one-dimensional linear diffusion since the diffusion space at around the electrode is restricted by the presence of the microchannel (channel depth = 20 μm) and the channel length is infinite (total length = 6 cm) as compared to the thickness of the diffusion layer. The simulations also reproduced almost satisfactorily the observed voltammograms in Figure 5-9 (a). It is concluded, therefore, that the electrochemical responses in the microchannel chip are best characterized by one-dimensional diffusion along the channel length and governed by the spatial geometry around the electrode.

5.3.2 Generation-Collection Mode Experiments under Non-Solution-Flow Conditions

To elucidate further the electrochemical characteristics of the channel-electrode chip, generation-collection mode (GC) experiments were explored. In the GC mode, a solute is electrolyzed at one electrode (generator, ***G***) and the electrolyzed solute is oxidized or reduced at the adjacent electrode (collector, ***C***).[12-14] In the present experiments, WE1 and WE2 in Figure 5-5 (c) were used as ***G*** and ***C***, respectively, and

the potential at ***G*** was swept from 0 to 450 mV while that at ***C*** was kept 0 V. Therefore, the ratio of the peak current at ***G*** (i_p (***G***)) to that at ***C*** (i_p (***C***)) is a measure of a collection efficiency of the cation as defined by the following equation,

$$\eta = \frac{i_c}{i_g} \qquad (5\text{-}8)$$

where η is the collection efficiency. A typical example of the cyclic volammogram observed by the GC mode experiments at ν = 5 mV s^{-1} is shown in Figure 5-11. The collection efficiency (η) was then determined to be 45%.

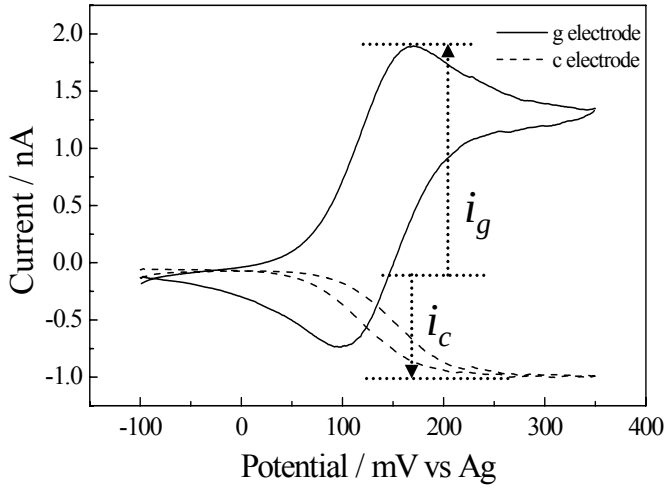

Figure 5-11 Cyclic votmmograms of FeCp-OH observed at generator (solid curve) and collector electrodes (broken curve) at ν = 5 mV s^{-1}.

The results on η at several ν determined with the microchannel chip (closed circles) and the electrode substrate (without a channel plate, closed triangles) under non-solution-flow conditions are summarized in Figure 5-12. It is worth emphasizing that the η value observed by the channel chip is almost two-times larger than that by the

electrode substrate irrespective of ν. At $\nu = 5$ mV s^{-1}, as an example, the η value by the channel chip was as high as 45% even for the edge-to-edge ***GC*** distance of 68 μm as shown in Figure 5-11. Since the FeCp-OH cation generated at ***G*** diffuses to both side of the electrode along the channel-length direction, η should be 50% as a maximum value. The observed η value thus implies almost complete collection of the cation at ***C***. In the case of dual band microelectrodes without a cover substrate, such a high collection efficiency cannot be realized with an interelectrode distance larger than 10 μm. Therefore, the presence of the microchannel wall above ***G*** and ***C*** provides extraordinary effects on η. The open circles and triangles in Figure 5-12 represent the simulated collection efficiencies for the microchannel chip and the electrode substrate, respectively. Although the observed collection efficiency is slightly larger than the relevant simulated value for the channel chip, the results almost agreed well with each other. One-dimensional linear diffusion along the channel length is the primary reason for the high collection efficiency in the chip.

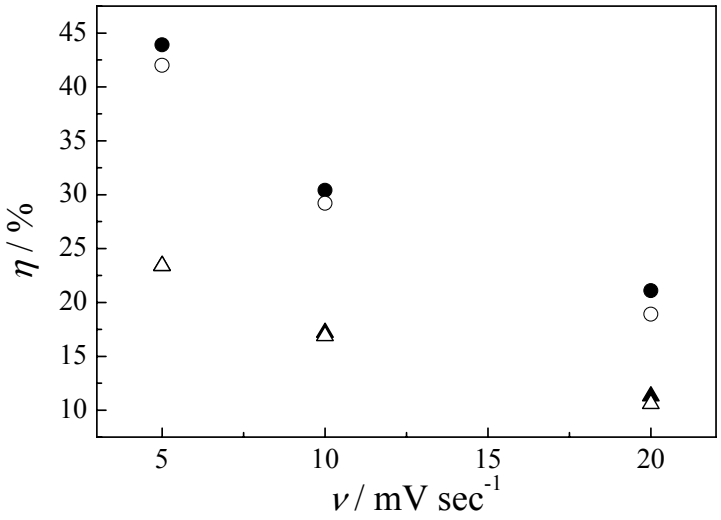

Figure 5-12 The potential sweep rate (ν) dependence of the collection efficiency (η). The closed circles and triangles are the data obtained by the microchannel chip and the electrode substrate, respectively. The open circles and triangles represent the results obtained by numerical simulations for the channel chip and the electrode substrate, respectively.

5.3.3 Generation-Collection Mode Experiments under Solution-Flow Conditions

GC mode experiments were also conducted under solution-flow conditions by using the microchannel chip, with WE1 (upstream side) and WE2 (down-stream side) being used as ***G*** and ***C***, respectively. A typical example of the voltammograms recorded at ***G*** and ***C*** (ν = 20 mV s^{-1}) is shown in Figure 5-13 (a) (linear flow velocity (u) = 8.3 mm s^{-1}). It is worth noting that the voltammograms observed under the solution-flow conditions are sigmoidal, which is in marked contrast to those in Figure 5-7. This is due

to the fact that efficient mass transport of FeCp-OH or the cation to ***G*** or ***C***, respectively, takes place by both diffusion and solution-flow. Further information on this point is obtained by the ν dependence of the η value. As shown in Figure 5-13 (b) (closed circles), the η value was almost constant at 28% irrespective of ν (u = 8.3 mm s^{-1}). It is interesting to note that, without solution-flow, the η value increases from 23 to 45% with a decrease in ν from 20 to 5 mV s^{-1} (Figure 5-12). The results indicate clearly that the electrode reaction is fast enough and mass-transport of FeCp-OH or the cation to the electrode is governed essentially by solution-flow. Therefore, the collection efficiency does not depend on the sweep rate at such a fast flow velocity. The η values obtained by the simulations shown by the open circles in Figure 5-13 (b) agreed very well with the observed one, which supported the above discussion as well.

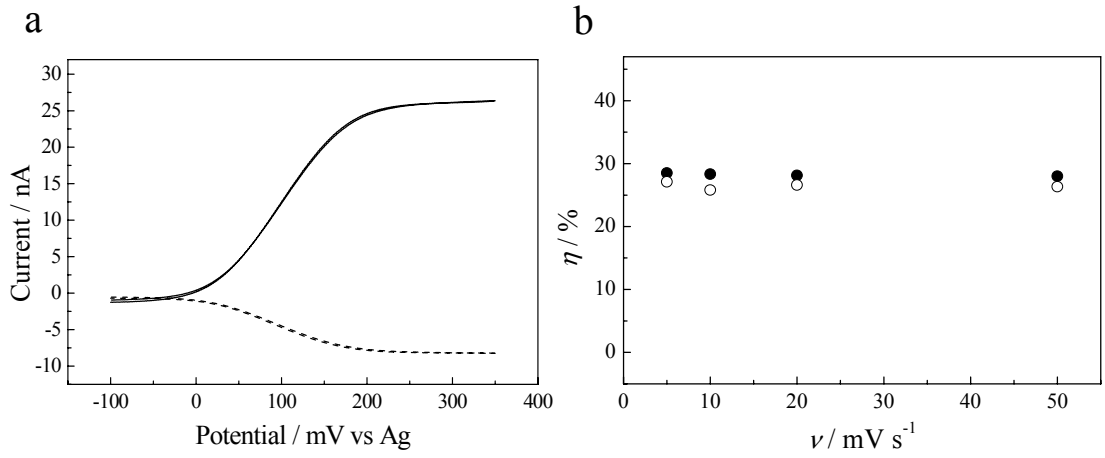

Figure 5-13 Cyclic voltammograms (ν = 20 mV s^{-1}) of FeCp-OH observed at ***G*** (solid curve) and ***C*** (broken curve) in the microchannel (a). A potential sweep rate (ν) dependence of the collection efficiency (b). The closed and open circles are the data obtained by the experiments and the numerical simulation, respectively. The linear flow velocity (u) was set 8.3 mm s^{-1} throughout the experiments.

The above discussion indicates that the η value should depend on the solution-flow velocity (u). Furthermore, the absence of the ν dependence of η at ν = 50 ~ 5 mV s^{-1} and u = 8.3 mm s^{-1} in Figure 5-13 demonstrates that a slower flow velocity and much faster potential sweep rate are necessary to study the u dependence of η. Therefore, chronoamperometry was conducted to study a u dependence of η. In the actual experiments, the time profiles of i_g and i_c were determined by stepping the potential at ***G*** from 0 to 350 mV, while ***C*** was set 0 V. A typical example of the results at u = 1200 (a) and 120 μm s^{-1} (b) is shown in Figure 5-14. Since the cation of FeCp-OH generated at ***G*** is transported compulsorily to ***C*** by solution-flow, the anodic current observed at ***C*** increased with time. On the basis of the results in Figure 5-14, the time necessary to reach the saturated i_c value was determined to be 0.1 or 0.4 s at u=1200 or 120 μm s^{-1}, respectively.

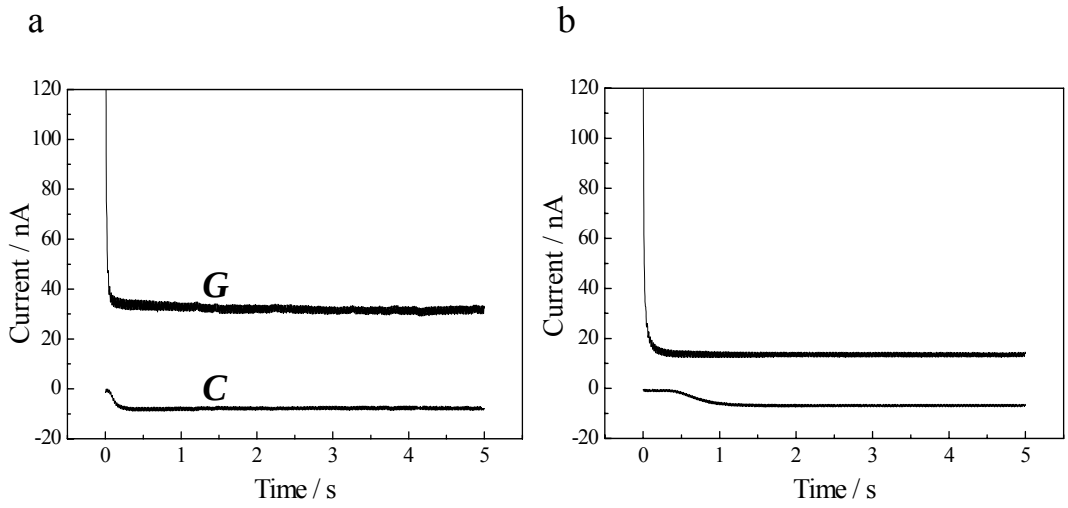

Figure 5-14 Time profiles of the currents observed at ***G*** and ***C*** in the channel chip at u = 1200 (a) and 120 μm s^{-1} (b).

Analogous experiments with those in Figure 5-14 were conducted at several u and, the steady-state i_g or i_c value in each time profile was plotted against u as shown in Figure 5-15 (a). The currents at ***G*** (closed circles) and ***C*** (open circles) increased to the positive and negative directions, respectively, with an increase in u, and saturated at almost constant values above a certain u value. The results on i_g indicate that FeCp-OH provided to ***G*** by solution-flow is oxidized almost completely at a low u value (solid line in Figure 15 (a)), while an increase in u resulted in over-feed of FeCp-OH to ***G*** and, therefore, the current is limited by the charge transfer rate at ***G***: leveling-off i_g. On the other hand, since the flow velocity is very fast, the most of the FeCp-OH cation produced at ***G*** is flow away to the downstream side of ***C*** without the electrode reaction. At a given u, therefore, i_c is saturated at a slower flow velocity than that at ***G***. Depending on the time scales of solution-flow and self-diffusion of FeCp-OH/FeCp-OH cation, therefore, the collection efficiency shows a maximum value at a certain u. In the present case, the η value of 87% was attained at u = 30 μm s^{-1} as shown in Figure 5-15 (b). The solid curve in the figure represents the results by the numerical simulations, which reproduces very well the experimental observations. Therefore, the results in Figure 5-15 (a) are reasonably explained along the context described above.

It is worth emphasizing that the collection efficiency at u = 30 μm s^{-1} was as high as 87% even for the edge-to-edge ***GC*** distance of 68 μm. In the case of ordinary dual-band electrodes, such a high collection efficiency is realized only with an interelectrode distance of several micrometers. Therefore, solution-flow in the microchannel provides extraordinary effects on η. Although the collection efficiency is almost constant at u > 500 μm s^{-1}, that is strongly dependent on u at u < 500 μm s^{-1} as the results of the relationship between the time scales of mass feed to ***G***/***C*** and the

charge transfer rate. The data in Figure 5-15 (a) demonstrate that the current value increases in proportion to the cubic root of u, which is in accordance with the results predicted by hydrodynamic voltammetry with channel electrodes under convective diffusion rate-limiting conditions.[15-17]

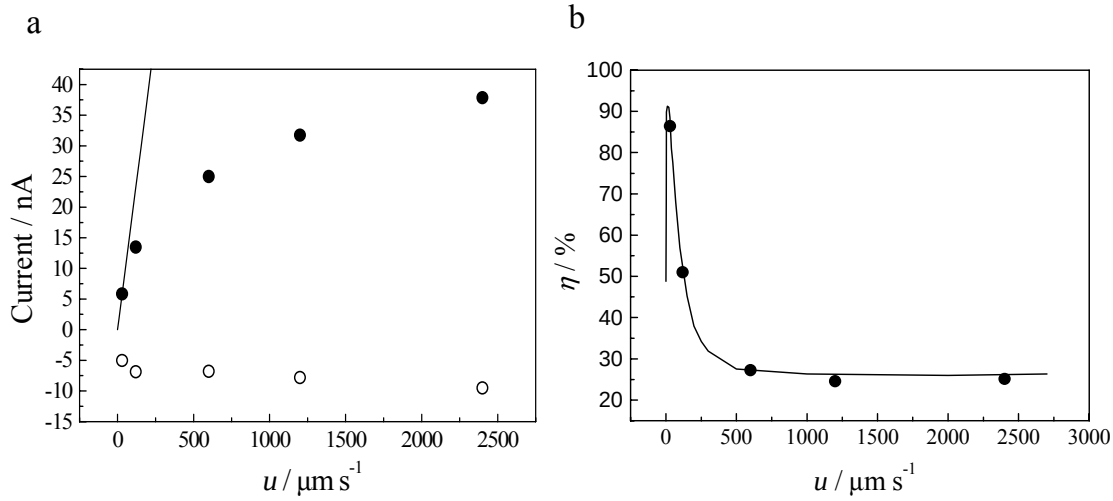

Figure 5-15 (a) The flow velocity dependencies of the steady-state currents observed at ***G*** and ***C***. The closed and open circles exhibit the data at ***G*** and ***C***, respectively. The solid line represents the predicted values when all FeCp-OH provided to ***G*** is oxidized completely at the electrode. (b) The flow velocity dependence of the collection efficiency (closed circles) calculated by the data in Figur5-15 (a). The solid curve represents the results by the numerical simulations.

5.4 Conclusion

A new and novel fabrication method of the polymer microchannel chip integrated with dual-band microelectrodes was established on the basis of photolithography and a

polymer imprinting method. Cyclic (linear sweep) voltammetry and generation-collection mode experiments were explored to elucidate characteristic responses of the electrodes in the fabricated microchannel chip. The voltammogram obtained by the channel chip was different from that by the electrode substrate without a channel plate, owing to a restricted space around the electrode in the microchannel chip. Reflecting such characteristics, the collection efficiency observed in the microchannel chip was almost two times larger than that in the absence of a channel substrate. Furthermore, the solution-flow velocity dependence of the collection efficiency in the channel chip demonstrated that the collection efficiency depended highly on the flow velocity, and the collection efficiency as high as ~90% was realized at an optimum solution-flow velocity. This is another interesting characteristic of the microelectrodes integrated in a microchannel chip. Polymer microdevices integrated with electrodes could be thus very promising as a high-efficient detection device, and can be applied to versatile microchip experiments as demonstrated in the following chapters.

5.5 References

1) Aoki, K.; Tanaka, M. *J. Electroanal. Chem.* **1989**, 266, 11-20.
2) Ferrigno, R.; Brevet, P.-F.; Girault, H. H. *J. Electroanal. Chem.* **1997**, 430, 235-242.
3) Harriman, K.; Gavaghan, D. J.; Houston, P.; Kay, D.; Suli, E. *Electrochem. Commun.* **2000**, 2, 576-585.
4) Henley, I. E.; Yunus, K.; Fisher, A. C. *J. Phys. Chem. B* **2003**, 107, 3878-3884.
5) Bard, A. J., Faulkner, L. R., Eds. *"Electrochemical Methods: Fundamentals and Applications"* 2nd ed. **1980,** John Willey & Sons: New York, 148-153, 168-190.

6) Shea, T. V.; Bard, A. J. *Anal. Chem.* **1987**, 59, 2101-2111.

7) Aoki, K.; Tokuda, K.; Matsuda, H. *J. Electroanal. Chem.* **1987**, 230, 61-67.

8) Aoki, K.; Tokuda, K. *J. Electroanal. Chem.* **1987**, 237, 163-170.

9) Alden, J. A.; Compton, R. G. *J. Phys. Chem. B* **1997**, 101, 8941-8954.

10) Slowinska, K.; Feldberg, S. W.; Majda, M. *J. Electroanal. Chem.* **2003**, 554, 61-69.

11) Bard, A. J., Faulkner, L. R., Eds. *"Electrochemical Methods: Fundamentals and Applications"* 2nd ed. **1980,** John Willey & Sons: New York, 231-232.

12) White, H. S.; Kittlesen, G. P.; Wrighton, M. S. *J. Am. Chem. Soc.* **1984**, 106, 5375-5377.

13) Bard, A. J.; Crayston, J. A.; Kittlesen, G. P.; Sher, T. V.; Wrighton, M. S. *Anal. Chem.* **1986**, 58, 2321-2331.

14) Niwa, O.; Morita, M.; Tabei, H. *Anal. Chem.* **1990**, 62, 447-452.

15) Matsuda, H. *J. Electroanal. Chem.* **1968**, 16, 153-164.

16) Matsuda, H. *J. Electroanal. Chem.* **1969**, 22, 413-421.

17) Compton, R. G.; Fisher, A. C.; Wellington, R. G. *J. Phys. Chem.* **1993**, 97, 10410-10415.

Chapter 6.

A Spectroelectrochemical Study on Perylene Cation Radical in Polymer Microchannel-Microelectrode Chips

6.1 Introduction

Characteristic electrochemical responses in the microchannel-electrode chips were elucidated in detail (Chapter 5). On the basis of the results, it was demonstrated that an electrochemically-generated specimen produced at the electrode in a channel chip was detected successfully by an adjacent electrode very efficiently. This indicates that efficient mass-transport of an electrochemically-generated specimen can be achieved in a microchannel. Namely, since a channel length is usually much longer than the width and depth of the channel, the electrode responses are characterized by one-dimensional linear diffusion along the channel length and, solution-flow makes molecular transport to the electrode very efficiently in the microchannel. Beside this, the channel wall above the electrode also influences extraordinary the electrode responses, as described in Chapter 5. For further extension of the study, such characteristics of the channel-electrode chip should be applied to other mode of experiments.

As another experimental mode by using a microchannel-electrode chip, absorption spectroscopy of a short-lived electrochemical intermediate including its dynamics was conducted in the present study. Generally, a spectroelectrochemical study has been conducted by using an optically-transparent thin layer electrode.[1-7] A channel flow cell and a stopped-flow electrolysis cell, capable of rapid electrolysis of a solute and simultaneous spectroscopic monitoring of electrochemical intermediates, has been also proposed.[8-12] Compared to the experiments with an optically-transparent thin-layer

electrode, the use of a microchannel-microelectrode chip will be advantageous. Furthermore, chip experiments are certainly more convenient as compared with the stopped-flow electrolysis cell experiments.

In the present study, the spatially-resolved absorption spectroscopy on the perylene (Pe) cation radical generated at the electrode in a microchannel-electrode chip was performed. It is easily expected that electrochemical intermediates generated at the electrode in the channel are governed by various factors. Therefore, a systematic spectroelectrochemical study on Pe as a function of an applied potential, the electrode-width, and a solution-flow velocity was conducted. Furthermore, the formation and disappearance processes of the transient electrochemical species of Pe in the channel were discussed on the basis of both flow velocity and position dependences of the absorption spectra of the Pe cation radical.

6.2 Experimental

6.2.1 Chemicals

Ethyl viologen dibromide (EV^{2+}) and perylene (Pe), both supplied from Aldrich Chemical Co., Inc. (99+%), were purified by repeated recrystallizations from ethanol and toluene, respectively. The structural formulas of EV^{2+} and Pe are shown in Figure 6-1. Propylene carbonate (PC, Tokyo Kasei Kogyo Co., Ltd., GR grade) was purified by vacuum distillation in the presence of CaH_2. Tetra-*n*-butylammonium perchlorate (TBAP, Tokyo Kasei Kogyo Co., Ltd., GR grade) was purified by repeated recrystallizations from acetone/diethyl ether and used as a supporting electrolyte throughout the study. Water was purified by distillation and deionization prior to use

(GSR-200, Advantec Toyo Co., Ltd.). Sample solutions were deaerated thoroughly by purging with an Ar gas stream for 20 min prior to experiments.

a b

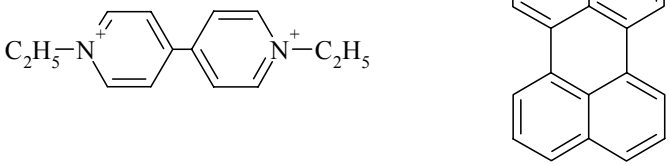

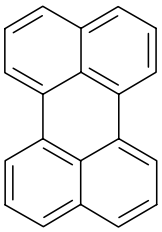

Figure 6-1 The structural formulas of EV^{2+} (a) and Pe (b).

6.2.2 Experimental Setup

Polymer microchannel-microelectrode chips were fabricated by the method described in Chapter 5. The whole structure of the channel chip fabricated in the present study is illustrated in Figure 6-2. In the present study, the width, depth and total length of the microchannel were set at 100 μm, 20 μm, and 60 mm, respectively. The Au band electrodes were used as working (WE) and counter electrodes (CE), and the integrated Ag band electrode was employed as a reference electrode (RE). The working electrode with the width of 50, 250, or 500 μm was fabricated perpendicularly to the direction of the channel length as shown in Figure 6-2, so that the length of the electrode was equal to the channel width: 100 μm.

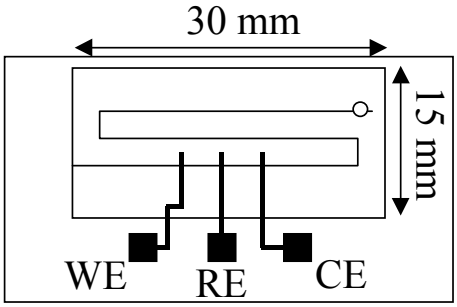

Figure 6-2 Structural layout of the microchannel chip integrated with band electrodes.

An experimental setup for a spectroelectrochemical study is illustrated in Figure 6-3. For absorption spectroscopy, analogous absorption microspectroscopy system with that described in Chapter 2 was employed. The diameter and quality of a probe beam are very important to perform precise and accurate absorption microspectroscopy. In the present experiments, the paraxial ray of a microscope objective (x 100, NA = 0.75) was used as a quasi-parallel probe beam, and its diameter was adjusted to ~2 μm. A solution-flow system analogous to that mentioned in Chapter 2 was employed. The actual flow velocity in the microchannel was evaluated by measuring the flow velocity dependence of a steady-state current of a standard sample (EV^{2+}) at the WE, since the current value depended highly on the flow velocity. A connection between the channel-electrode chip and an electrochemical analyzer (ALS, model 701A) via lead wires was made by a silver paste as an electroconductive adhesive as described in Chapter 5, and they were fixed with an epoxy resin. A bulk absorption spectroscopy was conducted by using a Hitachi U-3300 spectrometer and optically-transparent thin-layer electrode experiments were conducted according to Imabayashi et al.[13]

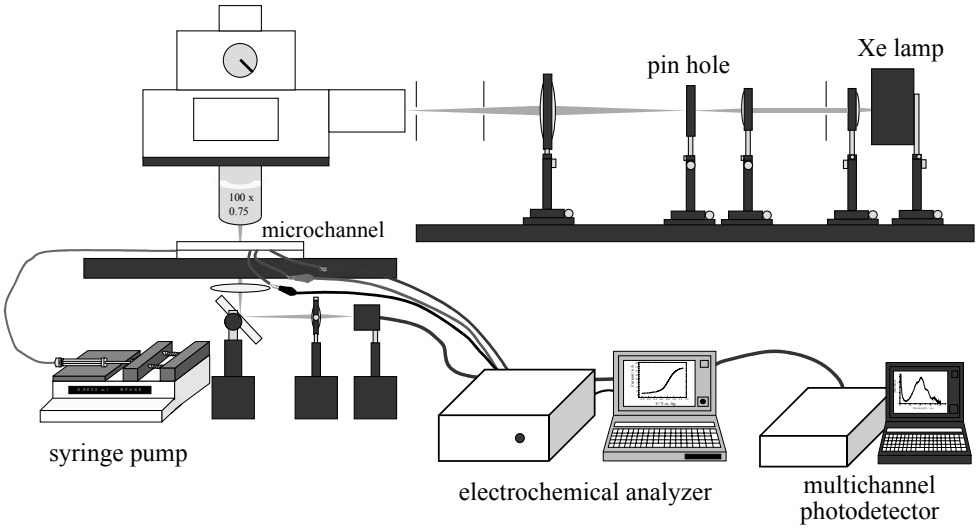

Figure 6-3 Schematic drawing of the spectroelectrochemical setup combined with a channel solution-flow system. WE, CE, and RE represent working, counter, and reference electrodes, respectively.

6.3 Results and Discussions

6.3.1 Absorption Microspectroscopy of EV^{2+} Cation Radical

An experimental check of the performances of the chip and the spectroelectrochemical system developed in this study was conducted by using EV^{2+} as a standard sample, since both electrochemical and spectroscopic properties of EV^{2+} and its cation radical are well known.[13] A PC solution of EV^{2+} (10, 15, or 20 mM) containing TBAP (0.1 M) was brought into the microchip with a flow velocity (u) of 0.33 mm s^{-1} and a potential (-0.4 V vs. Ag) was applied to the WE (electrode width = 500 μm). After the electrode current (i) reaches a steady state value, the absorption spectrum of the solution was measured at 30 μm separated from the WE in the downstream side: distance from the edge of WE (x) = 30 μm. The electrolyzed solution exhibited

characteristic absorption around 600 nm as shown in Figure 6-4. The absorption spectral band shape agreed very well with that of the EV^{2+} cation radical reported by Imabayashi et al.[14] At $[EV^{2+}]$ = 10 mM, the absorbance at the maximum wavelength (λ_{max} = 603 nm) was in good accordance with that predicted from the total electric charge flow at the electrode, as calculated by the relevant *i-t* (electrolysis time) curve. Therefore, it is concluded that EV^{2+} reduced at the electrode is followed quantitatively by absorption microspectroscopy even under the solution-flow conditions in the microchannel. Furthermore, the absorbance at λ_{max} increased linearly with the concentration of EV^{2+}. Assuming that the optical pathlength for absorption measurements is equal to the channel depth, the molar extinction coefficient (ε) at 603 nm determined by the concentration dependence of the absorbance shown in Figure 6-4 was 11900 $M^{-1}cm^{-1}$, which agreed very well with the literature value: 12300 $M^{-1}cm^{-1}$.[14] This also demonstrates that the channel depth is fabricated correctly by the imprinting method. These results also prove that correct and precise absorption spectroscopy of an electrochemical intermediate is attained on the basis of the present chip and the spectroelectrochemical system.

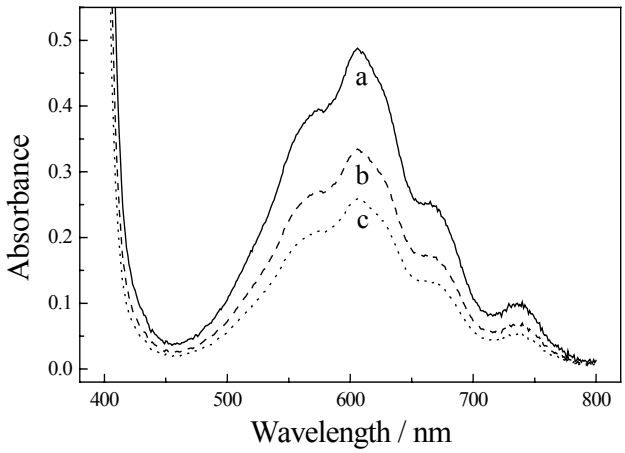

Figure 6-4 Absorption spectra of the EV^{2+} cation radical observed at 30 μm separated from the WE (500 μm-width) in the downstream side of the channel (x = 30 μm) at u = 0.33 mm s^{-1}. The concentration of EV^{2+} was set at 20 (a), 10 (b), or 5 mM (c).

6.3.2 Absorption Microspectroscopy of Perylene Cation Radical

Analogous experiments with those in Figure 6-4 were conducted for a PC solution of Pe. A PC solution of Pe (3 mM) containing TBAP (0.1 M) was introduced to the polymer chip at u = 0.83 mm s^{-1}, and the absorption spectrum of the solution phase was measured at x = 30 μm. At V = 0 V as shown in Figure 6-5, Pe exhibited the absorption spectrum shorter than 450 nm, and the spectrum possessing well-resolved peaks at λ = 390, 417, and 438 nm was observed (shown by the solid curve). Furthermore, the ε value at 438 nm (43000 $M^{-1}cm^{-1}$) agreed well with that obtained by bulk experiments: 41500 $M^{-1}cm^{-1}$. On the other hand, electrolysis of Pe was conducted at the oxidation potential of Pe in PC (1.1 V vs. Ag) by using the chip having the WE-width of 50, 250, or 500 μm. In the case of the 50 μm-wide WE, no change in the absorption spectrum

was observed. Since the electrode width is short and u is fast, electrolysis of Pe takes place very inefficiently. On the other hand, electrolysis of Pe proceeds efficiently by using the wider WE and, the absorbance of Pe at 438 nm decreased with increasing the electrode-width from 50 to 250 or 500 μm as shown in Figure 6-5. It is worth noting that the decreased amount of Pe determined by the absorbance change at 438 nm agrees very well with that expected from the total electric charge flowing at the electrode, as in the case for the experiments in Figure 6-4. At a given current density, Pe is electrolyzed quantitatively by using the 250 or 500 μm-wide WE, even under the solution-flow conditions: u = 0.83 mm s^{-1}.

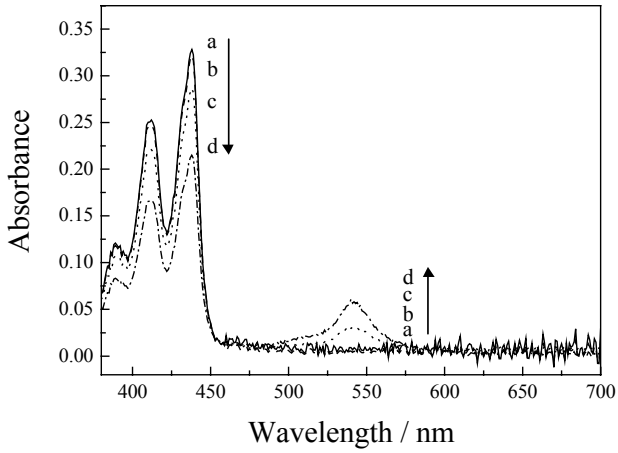

Figure 6-5 Absorption spectra of a PC solution of Pe (3 mM) observed at x = 30 μm under the conditions of without (a) and with the applied voltage (V = 1.1 V) to the 50- (b), 250- (c), and 500-width WE (d). The flow velocity was set at u = 0. 83 mm s^{-1}.

Very importantly, furthermore, the decrease in the absorbance at 438 nm accompanied the appearance of the new absorption in the wavelength region of 500-570 nm and, the absorbance of the new band observed by using the 500 μm-wide WE was larger than that by the 250 μm-wide WE. Spectroelectrochemical studies on Pe, including those on ECL (electrochemically-generated luminescence), have been sometimes reported.[12] Laser photolysis experiments have been also done for Pe in polar solvents.[15-17] According to these studies, the new absorption band observed in 500-570 nm is assigned confidently to the cation radical of Pe.

Absorption spectroscopy of the electrochemically-generated Pe cation radical was successful in the microchannel-microelectrode chip. However, the electrode-width dependence of the absorbance of the cation radical in Figure 6-5 indicates that the efficiency of the Pe electrolysis in the chip should be dependent also on the solution-flow velocity for a given electrode width and, this might influence observed phenomena. For quantitative discussions on the results, furthermore, V dependences of the absorbance of Pe (438 nm) and its cation radical (maximum wavelength = 538 nm) should be known. By using the 500 μm-wide WE, therefore, analogous experiments with those in Figure 6-5 were conducted at a slower flow velocity: u = 0.33 mm s^{-1}. The results on V dependences of the absorbance at 438 (Pe) and 538 nm (cation radical) monitored at x = 30 μm are summarized in Figure 6-6(a).

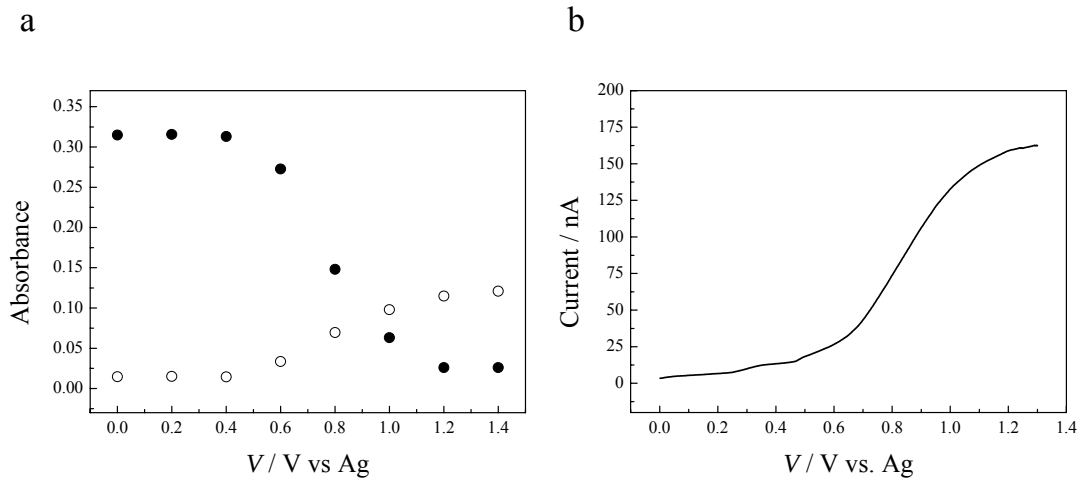

Figure 6-6 (a) Applied potential (V) dependences of the absorbance of Pe (438 nm, closed circles) and the cation radical of Pe (538 nm, open circles) observed under the conditions of [Pe] = 3 mM, x = 30 μm, and u = 0.33 mm s^{-1}. (b) A voltammogram of Pe observed in the microchannel-electrode chip at a sweep rate of 50 mV s^{-1}.

With increasing the applied voltage to the WE, the absorbance of Pe decreased gradually at V > 0.6 V and became almost zero at V = 1.1 V, demonstrating that almost of all Pe molecules within the diffusion distance of the electrode were oxidized at this potential. This is very reasonable, since the relevant i-V curve (i.e., voltammogram, scan rate = 50 mV s^{-1}) shows analogous V dependence of i as shown in Figure 6-6 (b). This demonstrates, again, that correct spectroelectrochemical experiments have been done by the present experimental setup. Reflecting such the V dependence of the Pe absorbance, the absorbance of the Pe cation radical increased gradually from V = 0.6 to 1.1 V, indicating one-to-one correspondence of the absorbance at 438 and 538 nm. The results demonstrate clearly that the cation radical of Pe produced at the WE is detected successfully by absorption microspectroscopy. It is worth emphasizing, furthermore,

that the absorbance change of the Pe cation radical (Figure 6-6 (a)) is proportional to the current change in the voltammogram. The *V* dependences of the absorbance in Figure 6-6 (a) can thus be well explained by the voltammogram in Figure 6-6 (b).

6.3.3 Spectroscopic Evidence of Formation of Perylene Dimer Cation Radical

The ε value of Pe at 438 nm is 41500 $M^{-1}cm^{-1}$, while that of the cation radical at 538 nm has been reported to be 48000 M^{-1} cm^{-1}.[18] Therefore, the increased amount of the absorbance at 538 nm should be larger by a 1.16-fold as compared to the decreased amount of the absorbance at 438 nm. As the results in Figure 6-6 (a) shows, however, the absorbance at 538 nm at a given *V* (> 0.6 V) is almost one-third of the value predicted from the decreased amount of Pe. In order to check such observations, a concentration dependence of the absorption spectrum of the Pe cation radical was studied on the basis of using an optically-transparent thin-layer electrode cell. Although the absorption spectrum of the cation radical observed by the thin-layer cell (*V* = 1.1 V) at a low Pe concentration (0.2 mM) agreed very well with that by the 250 μm-wide WE in Figure 6-5, the absorbance at 538 nm was not proportional to the concentration of Pe, but a new peak appeared at around 510 nm at high Pe concentrations (> 0.6 mM). Furthermore, its absorbance increased with increasing in the Pe concentration (0.6 ~ 2.0 mM, data are not shown here).

So far, the absorption spectra of the reduced and oxidized species of Pe have been studied in terms of ECL[12] and photoinduced electron transfer reactions in polar solvents.[18] According to these studies, the cation radical of Pe can react with a neutral Pe molecule in polar solvents, and this produces a face-to-face Pe dimer cation radical.[19]

At a relatively high Pe concentration, in practice, Kimura et al. reported that a new absorption band appeared in the shorter wavelength region of the absorption spectrum of the Pe cation radical, owing to formation of the perylene dimer cation radical.[20] Such spectral characteristics reported by Kimura et al. are quite analogous to the absorption spectrum observed by the present thin-layer electrode cell experiments. Therefore, it is supposed that the smaller absorbance change of the Pe cation radical, as compared to that predicted from the decreased amount of Pe in Figure 6-6 (a), will be ascribed to formation of the perylene dimer cation radical ($Pe^{+\cdot}$-Pe) in the present system.

In order to obtain clearer evidence for formation of the Pe dimer cation radical, a solution-flow velocity dependence of the absorption spectrum was studied under the electrolytic conditions of V = 1.1 V and the electrode-width of 500 μm. The results are summarized in Figure 6-7. At u = 1.0 mm s^{-1}, the absorption bands of both Pe (438 nm) and the Pe cation radical (538 nm) are observed analogous to those in Figure 6-5. A close inspection of the spectrum indicated, however, that a weak absorption band was discernible at around 510 nm. Furthermore, the absorption intensity at 510 nm became stronger with decreasing the flow velocity and, the ratio of the absorbance at 510 nm to that at 538 nm increased from 0.63 to 0.88 with the decrease in u from 1.0 to 0.17 mm s^{-1}. The spectral characteristics agreed very well with those observed by the thin-layer cell experiments at a high perylene concentration as well as with the report by Kimura et al.[20] Therefore, it is concluded that the new absorption peak at 510 nm is ascribed to that of the Pe dimer cation radical. At a low solution-flow velocity, Pe is oxidized at the electrode very efficiently. Therefore, the formation efficiency of the Pe dimer cation radical becomes higher at a lower u.

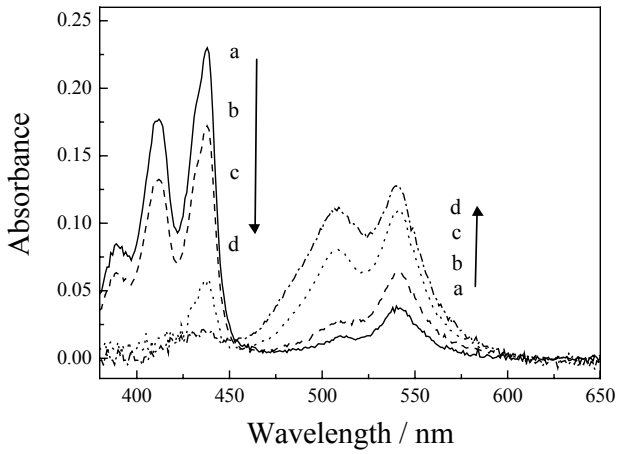

Figure 6-7 Absorption spectra (V = 1.1 V and x = 30 μm) observed at several flow velocities: u = 1.00 (a), 0.67 (b), 0.33 (c), and 0.17 mm s^{-1} (d).

6.3.4 Evaluation of the Lifetimes of the Monomer and Dimer Cation Radicals of Perylene

One of the important aspects into the present study is that the microchannel-microelectrode chip experiments under solution-flow conditions enable one to produce steadily a relatively short-lived, redox intermediate(s) along the flow direction. In different from thin-layer electrode experiments, furthermore, one can observe always a fresh electrolyzed solution by the channel experiments. Combining the microchip technique with space-resolved absorption spectroscopy, the lifetimes of the monomer and dimer cation radicals of Pe could be evaluated. Therefore, absorption microspectroscopy of an electrolyzed Pe solution along the solution-flow direction was conducted: x dependence of the absorbance.

A PC solution of Pe (3 mM) was introduced to the chip at u = 0.33 mm s^{-1} and

electrolyzed at the 500 μm-wide WE (V = 1.1 V). The results are summarized in Figure 6-8 as the x dependences of the absorbance of Pe (438 nm), the cation radical (538 nm), and the dimer cation radical (510 nm). Although the data are somewhat scattered, the absorbance at 438 nm (Pe) was almost constant around 0.06 irrespective of x. This indicates that, once Pe is oxidized at the electrode, that is not regenerated in the observed region of x (30 ~ 450 μm). For the cation radical or dimer cation radical in the x range of 30 - 150 μm, on the other hand, the absorbance was almost constant at around 0.10 ~ 0.11 or 0.07 ~ 0.08, respectively. Since the electrolyzed solution is provided to each position from the upstream side of the channel, the concentrations of the cation radicals will be in the steady-state, in which mass (i.e., cation radical) feed is balanced with the decay of them.

At x > 150 μm, however, the absorbance of the cation radicals decreased gradually with x. Since the flow velocity (u) is fixed at constant, the positional (x) data in Figure 6-8 can be converted very easily to the temporal (t) data ($t = x/u$), as the temporal scale is included in the figure. The data demonstrate that the absorbance of the monomer or dimer cation radical decreased gradually in the t range of 0.6-1.2 or 0.4-0.8 s, respectively. In principle, the absorbance should decrease single exponentially with time. However, since the electrode-width (500 μm) is comparable to the x range studied, the absorbance does not decay single exponentially, which prevents exact determination of the lifetimes of the cation radicals. Nevertheless, Figure 6-8 demonstrates that the lifetimes of the monomer and dimer cation radicals of Pe are in the order of several hundreds of milliseconds. The different decay rate constant between the absorbance at 538 and 510 nm also indicates that the absorption peak at 510 nm is not ascribed to that of the monomer cation radical of Pe.

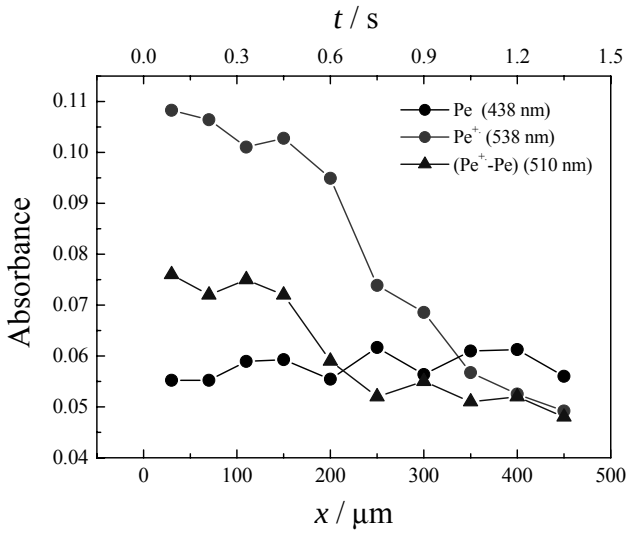

Figure 6-8 Position (x) and time (t) dependences of the absorbance of Pe (438 nm, circles), the Pe dimer cation radical (510 nm), and the Pe cation radical (538 nm) at u = 0.33 mm s^{-1} and V = 1.1 V.

It has been reported that the lifetime of an electrochemically-generated Pe cation radical in acetonitrile (0.5 mM) is in the order of several tens of seconds.[21] Therefore, the lifetime value evaluated in this study is very short. However, it is also true that the lifetime of a cation radical is highly dependent on the concentration of a solute and, nature and the purities of a solvent and an electrolyte used.[22] In the present study, the concentration of Pe is very high (3 mM) and propylene carbonate is used as the medium, which might be somewhat unconventional for electrochemical studies as compared with the use of acetonitrile as a solvent. Owing to the high concentration conditions, furthermore, the dimer cation radical of Pe is produced efficiently and this reduces the lifetime of the monomer cation radical. It is supposed that these factors are the primary reasons for the short-lifetime of the Pe cation radical in the present experiments.

The monomer and dimer cation radicals of Pe will be in an equilibrium, so that the lifetimes with analogous time constant evaluated in the present experiments will be reasonable, although the stability of each cation radical is different, leading to different decay time constants of the cation radicals. The formation and disappearance processes of the transient electrochemical species were followed successfully by the present microspectroscopy-electrochemical techniques.

6.4 Conclusion

A spectroelectrochemical study on the perylene cation radical was conducted on the basis of potential applications of the fabricated microchannel-microelectrode chip and space-resolved absorption spectroscopy. Electrochemical detection techniques combined with spectroscopy was shown to be powerful means to elucidate electrochemical species produced in a given system. In practice, it was demonstrated explicitly formation of the Pe dimer cation radical, which could not be identified by electrochemical measurements alone. Furthermore, spatially-resolved absorption spectroscopy was successful to evaluate the lifetimes of both monomer and dimer cation radicals of Pe. This can be done very easily by using a fluid manifold. On the basis of such a mode of experiments, dynamics of various electrochemical intermediates at a wide range of a time constant (> ~10 ms) will be followed directly. An electrochemical cyanation reaction of pyrene proceeded very efficiently along water/oil flow in a microchannel-microelectrode chip as described in the next chapter. For elucidation of such reaction mechanisms, the present technique will also play important roles.

6.5 References

1) Heineman, W. R.; DeAngelis, T. P.; Goelz, J. F. *Anal. Chem.* **1975**, 47, 1364-1369.

2) Kenyhercz, T. M.; DeAngelis, T. P.; Norris, B. J.; Heineman, W. R.; Mark, H. B., Jr. *J. Am. Chem. Soc.* **1976**, 98, 2469-2477.

3) Blubaugh, E. A.; Yacynych, A. M.; Heineman, W. R. *Anal. Chem.* **1979**, 51, 561-565.

4) Baumgartner, C. E.; Marks, G. T.; Aikens, D. A.; Richtol, H. H. *Anal. Chem.* **1980**, 52, 267-270.

5) Pinkerton, T. C.; Hajizadeh, K.; Deutsch, E.; Heineman, W. R. *Anal. Chem.* **1980**, 52, 1542-1544.

6) Rhodes, R. K.; Kadish, K. M. *Anal. Chem.* **1981**, 53, 1539-1541.

7) Bowden, E. F.; Cohen, D. J.; Hawkridge, F. M. *Anal. Chem.* **1982**, 54, 1005-1008.

8) Wang, Z.; Zhao, M.; Scherson, D. A. *Anal. Chem.* **1994**, 66, 4560-4563.

9) Wang, R. L.; Tam, K. Y.; Marken, F. *Electroanal.* **1997**, 9, 284-287.

10) Tam, K. Y.; Wang, R. L.; Lee, C. W. *Electroanal.* **1997**, 9, 219-224.

11) Oyama, M.; Nozaki K.; Okazaki, S. *Anal. Chem.* **1991**, 63, 1387-1392.

12) Oyama, M.; Mitani, M.; Okazaki, S. *Electrochem. Commn.*, **2000**, 2, 363-366.

13) Imabayashi, S.; Kitamura, N.; Tokuda K.; Tazuke, S. *Chem. Lett.* **1987**, 455-458.

14) Imabayashi, S.; Kitamura, N; Tazuke, S.; Tokuda, K. *J. Electroanal. Chem.* **1988**, 239, 397-403.

15) Kawai, K.; Yamamoto, N.; Tsubomura, H. *Bull. Chem. Soc. Jpn.* **1970**, 43, 2266-2268.

16) Grellmann, K. H.; Watkins, A. R. *Chem. Phys. Lett.* **1971**, 9, 439-443.

17) Shkrob, L. A.; Sauer, M. C. Jr; Trifunac, A. D. *J. Phys. Chem.* **1996**, 100,

7237–7245.

18) Konuk, R.; Cornelisse J.; McGlynn, S. P. *J. Chem. Phys.* **1985**, 82, 3929–3932.

19) Oyama, M.; Mitani, M.; Washida, M.; Masuda T.; Okazaki, S. *J. Electroanal. Chem.* **1999**, 473, 166–172.

20) Kimura, K. Yamazaki T. Katsumata, S. *J. Phys. Chem.* **1971**, 75, 1768–1774.

21) Mueller, J.; Kersten D.; Heckner, K. H. *Z. Phys. Chemie Leipzig* **1973**, 254, 387–392.

22) Bard A. J. ed. *"Electroanalytical Chemistry"* **1967**, l-II, 1, Marcel Dekker, New York.

Chapter 7.

One-Step Electrochemical Cyanation Reaction of Pyrene in Polymer Microchannel-Electrode Chips

7.1 Introduction

As described in Chapter 4, it was demonstrated that an oil/water interfacial photocyanation reaction of pyrene (PyH) proceeded via a photoinduced electron transfer (PET) mechanism in a microchannel. The PyH cation radical produced by PET with an electron acceptor is reacted with a cyanated ion presented in the system, producing 1-cyanopyrene. In the case of an electrochemical reaction, if the pyrene cation radical generated at an electrode is subjected to a nucleophilic attack by a cyanide ion, it is expected that an electrochemical cyanation reaction of PyH would proceed along solution-flow in a microchannel-electrode chip. Among various synthetic reactions, electroorganic synthesis will be one of the most appropriate chemical reactions applied to a microsystem, since a reactant in a microchannel device integrated with an electrode(s) is electrolyzed very efficiently as compared to that in a bulk system, owing to confinement of the solute to the minute space in the vicinity of the electrode in the channel as shown in Chapter 5. It is also considered that subsequent side reaction of an electrolyzed specimen will be reduced by one-directional solution-flow in a microchannel and this has a possibility to control the product selectivity.[1] On the basis of these characteristics, therefore, the research relevant to an electroorganic synthesis in a microchannel chip is worth exploring in detail.

In the present study, electrochemical cyanation of PyH in a microchannel-electrode chip was performed, and the reaction mechanism was discussed. The pyrene cation

radical generated at the electrode in a channel chip reacts with a cyanide ion at an oil/water interface along the solution-flow as illustrated in Scheme 7-1. As demonstrated in Chapter 6, furthermore, an electrochemical intermediate such as a perylene cation radical can be easily followed spectroscopically in a microchannel chip. In this study, the pyrene cation radical as the intermediate of the electrochemical cyanation reaction was monitored by *in-situ* microspectroscopy to elucidate the reaction mechanism. It is also expected that the product yield and selectivity will be governed by various factors, so that a systematic study on the present synthetic reaction was conducted as a function of a solution-flow velocity and channel-electrode geometries. To discuss the electrochemical reaction, the experimental results of the product yield and selectivity were evaluated on the basis of a space-resolved absorption spectroscopy and the results by numerical simulations of the mass-transfer processes in the channel chip were compared with the experimental observations.

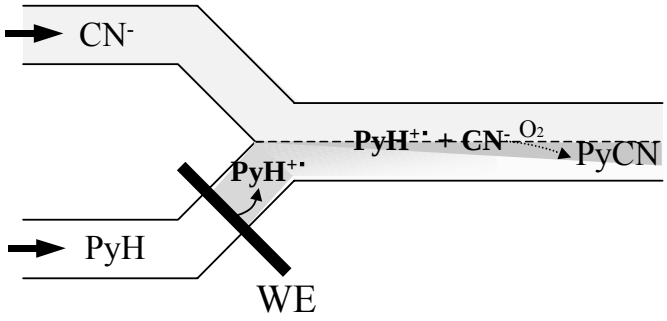

Scheme 7-1 Electrochemical cyanation reaction of PyH in a microchannel (Chip B)

7.2 Experimental

7.2.1 Chemicals

Pyrene (PyH) and propylene carbonate (PC) were the same samples with those described in Chapter 4. Acetonitrile (AN, Dojindo Laboratories, 99+%) was used without further purification. Tetra-*n*-butylammonium perchlorate (TBAP, Tokyo Kasei Kogyo Co., Ltd., GR Grade) was purified by repeated recrystallizations from acetone/diethyl ether, and was used as a supporting electrolyte throughout the study. Water was purified by distillation and deionization prior to use (GSR-200, Advantec Toyo Co., Ltd.). Sample solutions were dearerated thoroughly by purging with an Ar gas stream for 20 min prior to experiments.

7.2.2 Fabrication of Polymer Microchannel-Electrode Chips

Polymer microchannel-electrode chips were fabricated by the method described in Chapter 5 with some modifications. Although the use of a polymer substrate is very versatile, one of the disadvantages is a low resistibility to organic solvents. In order to improve such characteristics, therefore, an amorphous fluorocarbon resin (Cytop, Asahi Glass Co., Ltd.) was spin-coated onto a polystyrol substrate for fluorination of the surface prior to use. A silicon template for imprinting was fabricated by photolithography and dry etching techniques as described in Chapter 3. For fabrication of a channel substrate, the silicon template and the fluorinated polystyrol substrate (15 $\times$30 mm) were fastened tightly between two pieces of a glass plate and heated at 110 °C for 25 min to transfer the embossed structure of the template to the polymer plate. In the present study, the width, depth, and total length of the fabricated double

Y-structured microchannel were set at 100 μm, 20 μm, and 60 mm, respectively.

On the other hand, an electrode substrate was fabricated by an imprinting method. In the present experiments, a Pt or Ag foil with the thickness of 100 μm was used as an electrode material. The foil with the width of 500 μm and the length of 10.0 mm was cut and, the two pieces of the Pt foil (as working (WE) and counter electrodes (CE)) and one piece of the Ag foil (as a reference electrode (RE)) were put at appropriate positions on a fluorinated polystyrol substrate (26×30 mm). The three metal pieces and the fluorinated polystyrol substrate were then fastened tightly between two pieces of a glass plate and heated at 110 °C for 25 min to bury the electrodes into the polymer substrate. Introduction of the electrodes into the polymer and their positions on the substrate were confirmed by observation under an optical microscope (Nikon Co., Optiphoto-2). Finally, the electrode substrate was covered and bonded with the channel substrate by pressing the two substrates between two glass plates at 110 °C for 18 min. The electrodes with the width of 500 μm were fabricated perpendicularly to the direction of the channel length and, thus, the lengths of the electrodes were equal to the channel width: 100 μm.

In the experiments, two types of the microchannel-electrode chip was fabricated: one for homogeneous electrochemical cyanation of PyH (Figure 7-1 (a), Chip A) and the other for water/oil interfacial electrochemical cyanation of PyH (Figure 7-1 (b), Chip B). In the case of Chip A, the WE was set at 10 mm in the downstream-side of the channel junction (x = 10 mm), while that in Chip B was integrated into the oil-phase channel in the upstream-side of the channel junction. The position of the WE in the channel (x) was varied as illustrated in Figure 7-1(b).

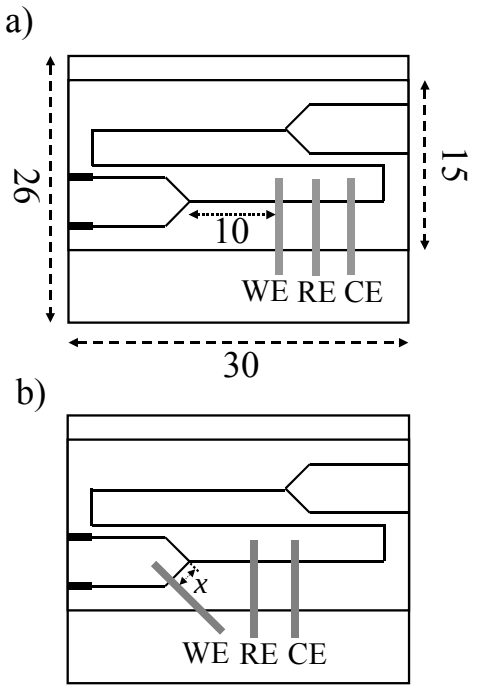

Figure 7-1 Structural layouts of the microchannel chip integrated with electrodes. WE, CE, and RE represent working, counter, and reference electrodes, respectively. The sizes in the figure are shown in millimeter. *x* in b) represents the distance between the channel junction and the position of the WE edge.

7.2.3 Experimental Setup

A solution flow system analogous to that described in Chapter 2 was employed in the present study. The connections between the electrodes and an electrochemical analyzer via lead wires were made by a silver paste as an electroconductive adhesive, and they were fixed with an epoxy resin as mentioned in Chapter 5. For an electrochemical reaction, a potential was applied to the WE by using an electrochemical analyzer (ALS Co., Ltd., Model 701A). For product analysis, the sample solutions

collected from the exits of the microchannel chip were analyzed by GC-MS (Shimadzu Co., QP-5050). The absolute yields of 1-cyanopyrene (PyCN) and 1,3-dicyanopyrene ($Py(CN)_2$) as the products of the electrochemical reaction were determined on the basis of the calibration curves obtained by GC analysis of the relevant authentic sample. For large-scale electrochemical experiments, a Pt electrode with the surface area of 480 cm^2 was used as WE, while Pt and Ag wires were employed as CE and RE, respectively. The sample solution in a beaker (300 ml) was stirred by using a magnetic stirrer during the reaction. Spectroelectrochemical measurements for monitoring the PyH cation radical produced at the WE integrated in the chip were conducted by using the absorption microspectroscopy system described in Chapter 6.

7.3 Results and Discussions

7.3.1 Electrochemical Cyanation Reaction of PyH: Large-Scale Experiments

An aqueous AN solution (25/25 ml) containing PyH (1.5 mM), NaCN (0.5 M), and TBAP (0.05 M) was electrolyzed at 1.5 V (vs. Ag) for 1 h. Figure 7-2 shows the gas chromatograms of the reaction mixtures extracted with chloroform before (solid line) and after the electrochemical reaction (dotted line). It is seen clearly that a disappearance of the peak responsible for PyH at the retention time (t_r) of 11.8 min upon electrolysis accompanies an appearance of two new peaks at t_r = 13.0 and 14.0 min. The t_r values agreed very well with those of authentic PyCN and $Py(CN)_2$, and the mass numbers of the compounds at t_r = 13.0 and 14.0 min were 227 (PyCN) and 252 ($Py(CN)_2$), respectively. The calibration curves for PyCN and $Py(CN)_2$ made by

separate experiments indicate that the absolute PyCN and $Py(CN)_2$ yields under the conditions mentioned above are 41 and 14%, respectively. On the basis of these results, it is concluded that one-step electrochemical cyanation reaction of PyH proceeds in moderate yields.

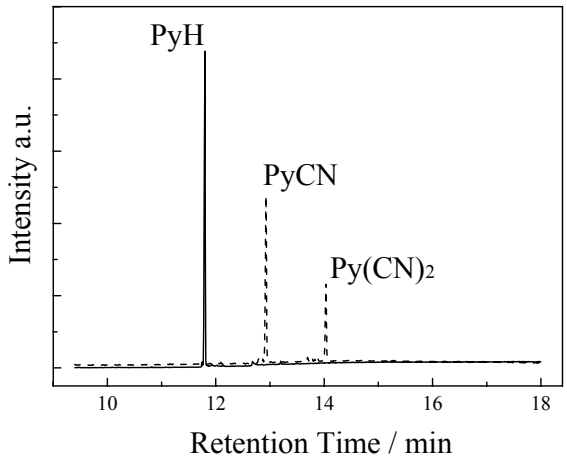

Figure 7-2　Gas chromatograms of the reaction mixtures before (solid line) and after the electrochemical reaction (dotted line).

In Chapter 4, it was demonstrated that one-pot and efficient cyanation of PyH was attained by a photoinduced electron transfer (PET) mechanism, in which the PyH cation radical produced by PET between the excited singlet-state of PyH and an electron acceptor in a polar medium was subjected to a nucleophilic attack by a cyanide ion, and the subsequent oxidation of the cyanated pyrenyl radical gave PyCN. Under the present experimental conditions, the oxidation potential of PyH in an aqueous AN solution is determined to be 1.4 V (vs. Ag). At the applied voltage to the WE (*V*) of 1.5 V, therefore, PyH should be oxidized efficiently, producing the cation radical of PyH. Under

analogous conditions, furthermore, formation of the PyH cation radical was confirmed as shown by a spectroelectrochemical study as described later. Therefore, it is concluded that the PyH cation radical produced at the WE is subjected to a nucleophilic attack by a cyanide ion and subsequent oxidation of the radical gives PyCN, similar to the photocyanation reaction of PyH as mentioned above.

On the other hand, $Py(CN)_2$ is produced by the electrochemical reaction, while that has not been confirmed by the photoreaction. One possible reason for formation of $Py(CN)_2$ in the present experiments might be participation of a CN radical and/or dicyan (cyanogen, $(CN)_2$) produced by direct oxidation of a cyanide ion at the WE. When the CN radical and/or $(CN)_2$ are produced, these species would attack PyH via a radical mechanism, producing $Py(CN)_2$. Under the present conditions, however, a cyanide ion is not electrolyzed since no current has been observed at the WE during electrolysis (V = 1.5V) of an aqueous NaCN solution. Therefore, the contribution of the CN radical and/or dicyan to $Py(CN)_2$ formation is denied.

Another possible origin of formation of $Py(CN)_2$ will be two-electron oxidation of PyH and/or one-electron oxidation of PyCN, giving the dication of PyH (PyH^{2+}) and/or the radical cation of PyCN ($PyCN^{+}$), respectively. In practice, the electrode potentials of E (PyH/PyH^{2+}) and E ($PyCN/PyCN^{+}$) were 1.55 and 1.51 V (vs. Ag), respectively, as estimated by cyclic voltammetry. At V = 1.5 V, therefore, both PyH^{2+} and $PyCN^{+}$ are likely to produce simultaneously during the electrolysis, and subsequent nucleophilic attack by a cyanide ion(s) will afford $Py(CN)_2$.

7.3.2 Electrochemical Cyanation Reaction of PyH in Polymer Microchannel-Electrode Chip

Since one-step electrochemical cyanation of PyH was successfully performed by bulk experiments, the reaction system was applied to the microchannel-electrode chip. An aqueous NaCN solution (1 M) and an AN solution containing PyH (3 mM) and TBAP (0.1 M) were introduced separately to the double Y-type microchannel-electrode chip (Chip A, see also Figure 7-1 (a)) with the same flow velocity (u = 0.05 μl min^{-1}), and the potential (V = 1.5 V) was applied to the WE (x = 10 mm). It is worth pointing out that, in a microchannel, two miscible solutions are not mixed simultaneously at the channel junction owing to the solution-flow characteristics in a microchannel: laminar flow.[2-7] In order to allow mixing two solutions and subsequent electrochemical oxidation of PyH, therefore, the WE was set at 10 mm in the downstream-side of the channel junction.

Figure 7-3 shows the gas chromatograms of the reaction mixtures before (solid line) and after the reaction (dotted line), where the later solution was collected from the exit of the microchannel. As in the case for the large-scale experiments, it was confirmed that the decrease in the PyH peak intensity resulted in an appearance of the PyCN and $Py(CN)_2$ peaks. The absolute PyCN and $Py(CN)_2$ yields were 61 and 4%, respectively. For the chip experiments, the reaction time (t) is determined by the residence time of the reactant solution in the microchannel; residence time = channel length (60 mm) / average linear flow velocity (mm s^{-1}). At u = 0.05 μl min^{-1}, as an example, t is calculated to be 140 s. It is worth emphasizing that, although the PyCN yield is 41% for the large-scale experiments with the reaction time of 1 h (Figure 7-2), that of 61% has been attained by the microchannel chip with the reaction time as short

as 140 s. Although the data are not shown here, the PyCN yield increased from 17 to 61% with decreasing the solution-flow velocity from 0.15 to 0.05 μl min^{-1}. The slower is the flow velocity, the more is the number of PyH oxidized at the WE. Therefore, the yield increases with decreasing the flow velocity. Furthermore, electrolysis of PyH at the WE in the microchannel proceeds more efficiently as compared to that in a bulk system. In a microchip, namely, the diffusion length of a solute is limited by the presence of the channel wall above the WE, leading to very efficient mass feed to the electrode. On the other hand, mass feed to the WE in a bulk system is governed essentially by the mass transport rate of PyH and its diffusion length around the WE is much longer than that in a microchip. Therefore, the superior PyCN yield observed by the chip over that by the bulk experiments is the reasonable consequence, and this is one of the important aspects into the electrochemical reaction in a microchip.

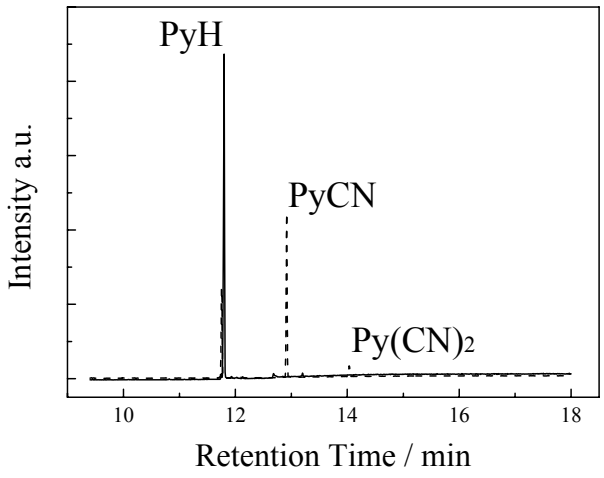

Figure 7-3 Gas chromatograms of the reaction mixtures before (solid line) and after the reaction (dotted line). The reaction mixture was collected from the exit of the microchannel-electrode chip (Chip A).

Another important result in the chip experiments is the lower $Py(CN)_2$ yield (4% at 0.05 μl min^{-1}) as compared to that in the bulk system: 14%. This is very important characteristics of the present reaction in the microchannel, and the product selectivity has been shown to be improved extraordinary by the use of the microchannel: the ratio of the PyCN yield to the $Py(CN)_2$ yield in the chip or bulk experiments is 15.3 or 2.9, respectively. Also, the results provide information about the reaction mechanisms. In bulk electrolysis, namely, PyCN once produced has many chances to be oxidized again producing $PyCN^{+\cdot}$. Therefore, $Py(CN)_2$ is likely to be produced by the reaction between $PyCN^{+\cdot}$ and a cyanide ion. However, the probability of reoxidation of PyCN is very low in the microchip, since the electrolyzed solution is driven away to the downstream-side of the WE. The lower $Py(CN)_2$ yield by the chip experiments compared to that by the bulk electrolysis thus suggests that the mechanistic origin of formation of $Py(CN)_2$ is cyanation of the PyCN radical cation, though the conclusive evidence has not been obtained yet. These results and discussions demonstrate that both the reaction yield and the product selectivity can be controlled by the solution-flow velocity in the microchannel-electrode chip, which cannot be realized by bulk electrolysis.

7.3.3 Electrochemical Cyanation Reaction of PyH at the Oil/Water Interface in Polymer Microchannel-Electrode Chip

For further demonstration of the characteristics of the microchip chemistry, an oil/water interfacial electrochemical cyanation reaction of PyH in a microchip was conducted. In the oil/water reaction system, the following processes would proceed in a

microchannel (see Scheme 7-1). Under laminar flow of an aqueous NaCN solution and an immiscible oil containing PyH and TBAP in a microchannel, electrolysis of PyH is conducted in the oil phase. In order to achieve this, Chip B (Figure 7-1 (b)) was used, in which the WE was set in the upstream-side of the channel junction. The cation radical of PyH generated at the WE is driven to the water/oil interface at the junction by pressure-driven flow and would be subjected to a nucleophilic attack by a cyanide ion at the interface, producing PyCN. Since the solubility of PyCN in water is very poor, PyCN will be distributed to the oil phase along solution-flow in the microchannel (i.e., extraction).

Experimentally, an aqueous NaCN solution (1 M) and a propylene carbonate (PC) solution of PyH (3 mM)/TBAP (0.1 M) were introduced separately to the Y-structured microchannel-electrode chip with the same flow velocity (u = 0.2 μl min^{-1}). After confirmation of formation of a stable oil/water interface in the channel, a potential (V = 1.5 V (vs. Ag)) was applied to the WE set at the channel junction (x = 0 mm) as shown in Figure 7-1 (b), where x is defined as the distance from the junction to an arbitrary position in the oil phase channel in the upstream-side. In the experiments, the solution-flow velocity (u) was set faster than 0.2 μl min^{-1} to construct stable and parallel oil/water streams in the microchannel (i.e., in the microchannel between the entrance and exit junctions).

Figure 7-4 shows the gas chromatograms of the water (a) and oil phases (b), which were collected from the exits of the microchip. It is seen clearly that PyCN is obtained exclusively from the oil phase, demonstrating that PyCN produced electrochemically is extracted to the PC phase during two-phase laminar flow in the microchannel. In practice, the two phases were separated completely even at the exit of the microchannel

as confirmed by observation under a microscope. The chromatogram in Figure 7-4 (b) also demonstrates that PyCN is produced selectively without formation of $Py(CN)_2$, though the PyCN yield of 13.5% is lower than that obtained by Chip A: Figure 7-3. Since the electrode is set at $x = 0$ before confluence of the two solutions, a PyH cation radical alone is generated at the electrode and this is subjected to a cyanation reaction at the interface. In the case of the homogenous electrochemical cyanation by using Chip A (Figure 7-3), the cation radical of PyCN would be more or less oxidized again producing $Py(CN)_2$ (4%), as discussed before. However, such a possibility is absent in the case of Chip B. Therefore, PyCN is produced exclusively by using Chip B. It is worth noting, furthermore, that u is set at 0.2 μl min^{-1} for the experiments in Figure 7-4, whose value is faster than those in Figure 7-3. One of the primary reasons for the lower PyCN yield as compared to that by Chip A is a faster solution-flow velocity and, this can be improved by the dimensions of the channel structures. On the basis of these discussions, it is concluded that the electrochemical cyanation reaction of PyH proceeds successfully at the PC/water interface in the microchannel as illustrated in Scheme 7-1.

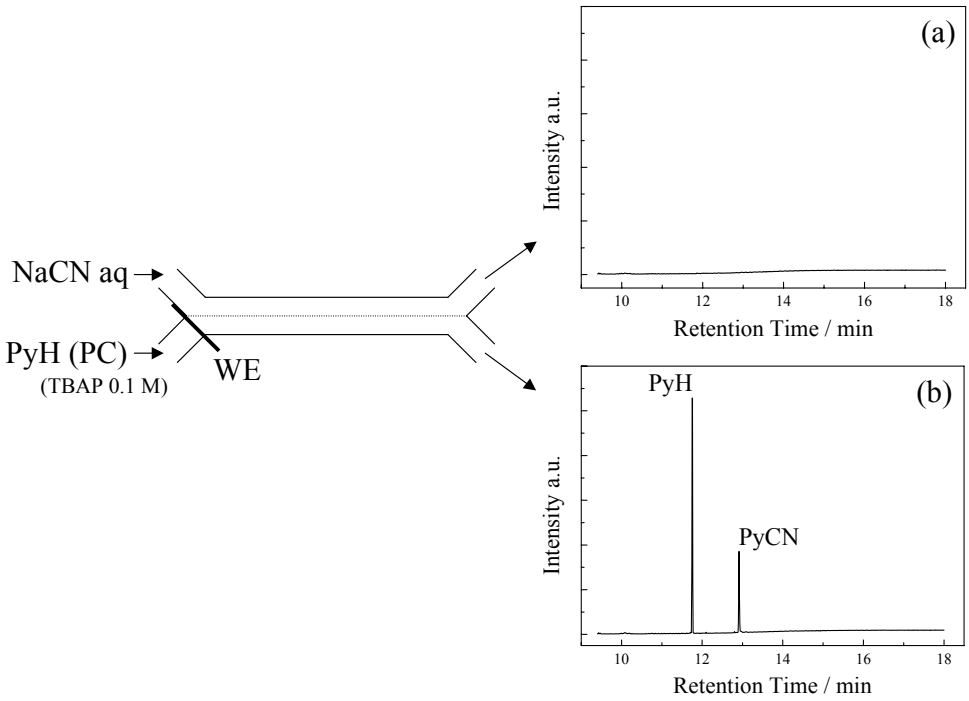

Figure 7-4. Gas chromatograms of the water (a) and oil phases (b) after the electrochemical reaction in the microchannel-electrode chip (Chip B).

Analogous experiments with those in Figure 7-4 were also performed at different *u* to elucidate the relationship between *u* and the PyCN yield. The *u* dependence of the absolute PyCN yield is summarized in Figure 7-5 (a). The results demonstrate clearly that the reaction yield increases from 4.2 to 13.5% with decreasing in *u* from 0.6 to 0.2 μl min^{-1}. This indicates that the electrochemical cyanation reaction of PyH can be controlled by the solution-flow velocity in the microchannel. Furthermore, it is supposed that the relationship between *u* and the PyCN yield should be related closely to the electric charge flowing at the electrode. The *u* dependence of the steady-state current at the WE was then studied by chronoamperometry. As shown in Figure 7-5 (b),

the steady-state current observed at the WE exhibited a very small *u* dependence. The results indicate that the *u* values studied are too fast and, this results in over-feed of PyH to the WE. Therefore, the current is limited by the charge transfer rate of PyH at the WE, demonstrating that the efficiency of the PyH electrolysis at each *u* is almost constant in a unit time. The amount of the PyH cation radical generated at the WE per unit volume thus decreases in proportion to the inverse of *u*, leading to the *u* dependence of the PyCN yield in Figure 7-5 (a). It is concluded that the *u* dependence of the PyCN yield is explained very well by the amount of PyH oxidized at the WE.

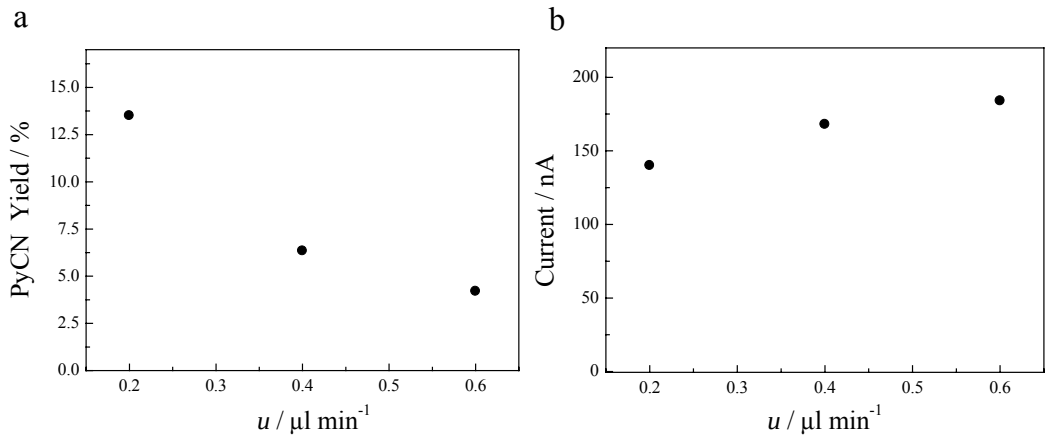

Figure 7-5　Solution-flow velocity dependences of the absolute PyCN yield (a) and the steady-state current observed at the WE (b) in the microchannel-electrode chip (Chip B).

7.3.4　Spatial Modulation of the PyCN Yield and It's Mechanistic Analyses

One of the important aspects into the present polymer microchannel-electrode chip is the fact that arbitrary-designed polymer channel-electrode chips can be fabricated

very easily. As an example, when the spatial position of the WE in the microchannel is modulated arbitrary, this might influence the PyCN yield. If this is the case, one can control the reaction yield by spatial arrangements of both the WE and the microchannel. In order to test such an idea, several channel-electrode chips were fabricated with the position of the WE in the oil phase being varied by x: x = 0.0 ~ -2.0 as shown in Figure 7-1 (b). Then, a WE position dependence of the PyCN yield was studied as the results were shown in Figure 7-6. It is seen clearly from the figure that the PyCN yield decreases with shifting the WE position toward the upstream-side (i.e, x from 0 to -2 mm), and the electrochemical cyanation reaction does not proceed at x = -2.0 mm. This is readily understood by the fact that the PyH cation radical generated at the WE is deactivated more or less before it reacts with a cyanide ion at the oil/water interface in the microchannel. Clearly, the efficiency of the cation radical reaching to the interface becomes lower with shifting the WE to the more negative direction in x: toward upstream-side of the junction.

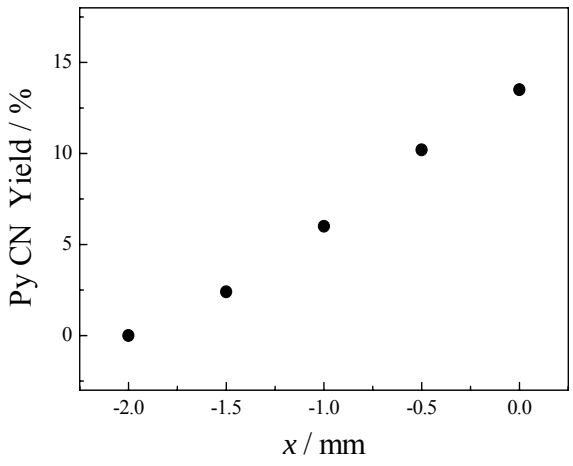

Figure 7-6 WE position (x) dependence of the absolute PyCN yield.

The above discussions indicate that the lifetime of the PyH radical cation generated at the WE is short and the radical cation should deactivate along with solution-flow. In order to confirm this directly, a spectroelectrochemical study by using the microchannel-electrode chip was explored. Experimentally, the absorption spectra of the oil phase at several positions in the vicinity of the WE (x = -2.5 ~ 0.0 mm) were measured upon electrolysis of the solution at V = 1.5 V (vs. Ag). In the experiments, the flow velocity was set at u = 0.1 μl min^{-1} to obtain the absorption spectrum with high signal-to-noise ratios. Figure 7-7 (a) shows the absorption spectra of the oil phase observed at x = -1.9, -1.3, and -0.7 mm. The absorption spectrum showing the maximum wavelength (λ_{max}) at 450 nm was in good accordance with that of the PyH cation radical, observed by laser photolysis or pulse radiolysis of PyH.[8-10] This demonstrates that a PyH radical cation is produced certainly as the intermediate for the cyanation reaction of PyH.

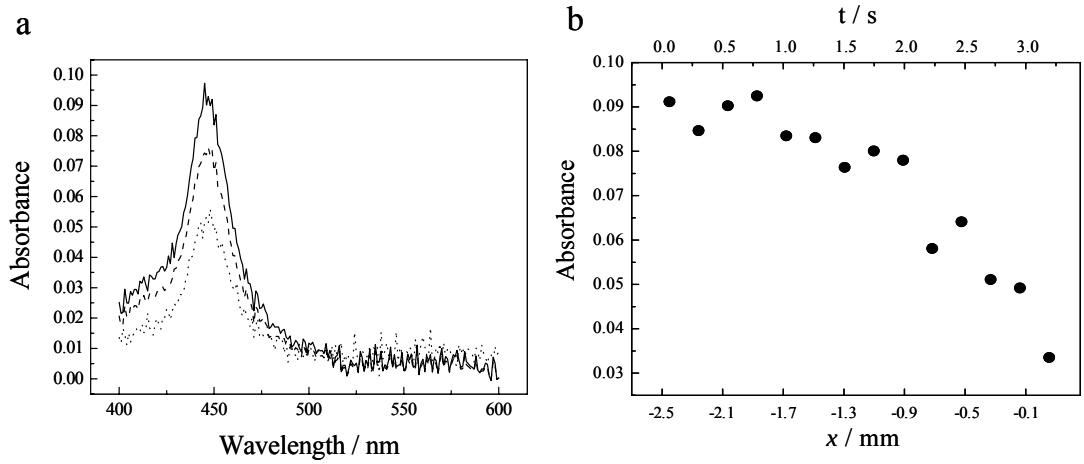

Figure 7-7 (a) The absorption spectra of the oil phase observed at x = -1.9 (the solid line), -1.3 (the broken line), and -0.7 mm (the dashed line). (b) The x dependence of the absorbance at 450 nm.

In the present experiments, the amount of the PyH cation radical can be estimated by the total electric charge flowing at the WE. At u = 0.1 μl min^{-1}, chronoamperometry indicates that one-third of the PyH molecules in the solution is oxidized to the cation radical at the electrode. Knowing the molar absorption coefficient of the PyH radical cation at 450 nm to be 45000 $M^{-1}cm^{-1}$,[11] the absorbance of the radical cation at 450 nm and x = -2.5 can be calculated, under the assumptions that the optical pathlength for absorption measurements is equal to the channel depth (20 μm) and the one-third of PyH in the sample solution (3 mM) is oxidized at the WE. The calculated value of 0.09 was in good agreement with the observed absorbance in Figure 7-7 (a): 0.09. Correct and precise absorption measurements have been shown to be conducted by the present spectroelectrochemical system and it is concluded that quantitative discussions on the cyanation reaction can be done on the basis of the spectroelectrochemical data.

Analogous experiments with those in Figure 7-7 (a) were then conducted at various x and, the x dependence of the absorbance at 450 nm was summarized in Figure 7-7 (b). Although the data were somewhat scattered, the absorbance at 450 nm was almost constant at around 0.09 in the x range of -2.5 ~ -1.9 mm. In this x range, therefore, the concentration of the cation radical is in the steady-state, in which mass (i.e., cation radical) feed to each position is balanced with deactivation of the cation radical, since the electrolyzed solution is provided continuously to each x position from the upstream side of the channel. At x > -1.7 mm, however, the absorbance of the cation radical decreased gradually with x. Since the flow velocity (u) is fixed at constant, the positional (x) data in Figure 7-7 (b) are converted very easily to the temporal data (t = x/u), as the temporal scale is included in Figure 7-7 (b). The data demonstrate that the absorbance of the cation radical decreased gradually in the t range of 1 - 3 s and,

therefore, the lifetime of the PyH cation radical is evaluated to be in the order of several seconds.

A numerical simulation was also conducted to elucidate diffusion characteristics of the PyH cation radical from the WE to the oil/water interface in the channel. It is considered here the case that a PyH radical cation is generated at the channel wall in the oil phase (i.e., $x = 0$) and it diffuses to the water/oil interface along the channel width direction: defined as the y-axis. Diffusion of the PyH cation radical in the oil phase is described by the one-dimensional Fick's law,

$$C_O(y,t) = \frac{D_O \partial C_O(y,t)^2}{\partial t^2} \qquad (7\text{-}1)$$

where $C_O(y, t)$ is the concentration of the radical cation at given y and a time (t).[12,13] D_O represents the diffusion coefficient of the radical cation in the oil phase and is assumed to be 2.0 x 10^{-6} $cm^2\ s^{-1}$, as the value for PyH in propylene carbonate calculated by the Stokes-Einstein equation. The time dependent transport factor of the PyH cation radical from the oil phase to the oil/water interface calculated by computer simulations is shown in Figure 7-8. On the basis of the data in Figure 7-8, 60% of the cation radical generated at the channel wall (i.e., WE) in the oil phase reaches to the interface within 2 s. This time constant is comparable to the estimated lifetime of the PyH cation radical in Figure 7-7 (b): 1~3 s. Therefore, the cation radical produced at the WE positioned at a moderate x (> -2.0 mm) can survive to the water/oil interface to react with a cyanide ion.

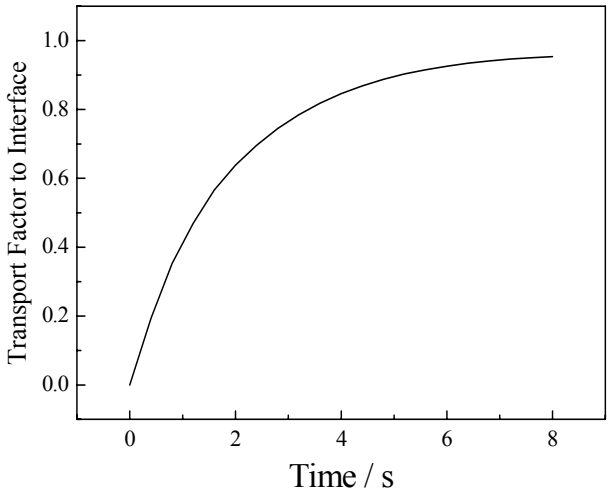

Figure 7-8　The time dependent transport factor of the PyH cation radical from the oil phase to the oil/water interface calculated by computer simulations.

On the basis of such experiments, simulations, and discussions, the experimentally observed electrochemical interfacial cyanation reaction of PyH in the microchannel is discussed and analyzed as follows. It has been reported that the rate of the nucleophilic substitution reaction of the PyH radical cation with a cyanide ion at a water/oil interface is fast enough, as compared to the mass transfer rate of the radical cation from the oil phase to the interface. It implies that the rate determining step of the overall cyanation reaction is the mass transport rate of the radical cation in the PC phase. Therefore, it is assumed that all of the radical cation molecules arrived to the interface afford PyCN, which enables one to simulate numerically *u* and *x* dependences of the PyCN yield. The results are shown in Figure 7-9, together with the observed data. For given *x* and *u*, the experimental data were slightly lower than those by the numerical calculations. This might be due to the fact that all of the PyH cation radicals diffuse to the interface do not

react necessarily with a cyanide ion and deactivate by a reaction with other molecules including water. However, the calculated curves reproduce reasonably the experimental data. It was confirmed that solution-flow velocity and electrode-position dependent experiments could elucidate the reaction mechanisms proceeding in a microchannel-electrode chip.

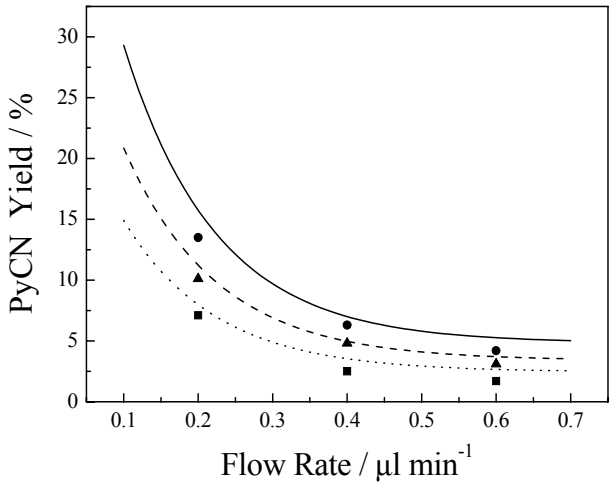

Figure 7-9 The solution-flow velocity and WE-position dependencies of the PyCN yield. The closed circles, triangles, and squares are the data obtained by the microchannel experiments at x = 0, -0.5, and -1.0 mm, respectively. The solid, broken, and dashed lines represent the results by numerical calculations at x = 0, -0.5 and -1.0 mm, respectively.

7.4 Conclusion

In the present study, two types of a microchannel-electrode chip were fabricated: one for electrochemical cyanation of PyH in a homogeneous aqueous AN solution (Chip

A) and the other for that at a water/propylene carbonate interface (Chip B). In both cases, PyCN was confirmed to be produced in a moderate yield even by the reaction in the microchannel. Furthermore, 1,3-dicyanopyrene is also produced under certain conditions. As one of the important results, however, the product selectivity (PyCN : $Py(CN)_2$) was shown to be controlled by both the experimental mode (Chip A or B) and the solution-flow velocity. In the case of the experiments with Chip B (interfacial system), PyCN as the sole product was obtained exclusively from the oil phase, demonstrating that the chip can be utilized as an automated electrochemical reactor. Furthemore, the PyCN yield was modulated by both the position of the WE in the microchannel and the solution-flow velocity. These cannot be done by a conventional bulk experiment and, the present results demonstrate certainly the high potentials of a microchannel-electrode chip. It is concluded that various new research fields could be developed by the use of microchannel chips. As a typical example of a novel microchip experiment, the microchannel-electrode chip was applied successfully to a microchannel-heater chip, and the heater chip was employed as a thermal microreaction system as described in the following Chapter.

7.5 References

1) Löwe, H.; Ehrfeld, W. *Electrochim. Acta* **1999**, 44, 3679-3689.
2) Weigl, B. H.; Kriebel, J.; Mayes, K. J.; Bui, T.; Yager, P. *Mikrochim. Acta* **1999**, 131, 75-83.
3) Yang, Z.; Matsumoto, S.; Goto, H.; Matsumoto, M.; Maeda, R. *Sens. Actuat. A: Phys.* **2001**, 93, 266-272.
4) Weigl, B. H.; Bardell, R. L.; Kesler, N.; Morris, C. J. *Fresen. J. Anal. Chem.* **2001**,

371, 97-105.

5) Hinsmann, P.; Frank, J.; Svasek, P.; Harasek, M.; Lendl, B. *Lab. Chip* **2001**, 1, 16-21.

6) Costin, C. D.; Synovec, R. E. *Anal. Chem.* **2002**, 74, 4558-4565.

7) Kam, L.; Boxer, S. G. *Langmuir* **2003**, 19, 1624-1631.

8) Grellmann K. H.; Watkins, A. R. *J. Am. Chem. Soc.* **1973**, 95, 983-985.

9) Shida T. Hamill, W. H. *J. Chem. Phys.* **1966**, 44, 4372-4377.

10) Kira, A.; Arai S.; Imamura, M. *J. Chem. Phys.* **1971**, 54, 4890-4895.

11) Hino, T.; Akazawa, H.; Masuhara H.; Mataga N. *J. Phys. Chem.* **1976**, 80, 33-36.

12) Cabrera, C. R.; Finlayson, B.; Yager, P. *Anal. Chem.* **2001**, 73, 658-666.

13) Kamholz, A. E.; Yager, P. *Sens. Actuat. B: Chem.* **2002**, 82, 117-121.

Chapter 8.

Fabrication of Polymer Microchannel-Microheater Chips and Their Applications to Thermal Phase Transition of a Polymer Solution and a Thermal Synthetic Reaction

8.1 Introduction

Microchannel-electrode chips were shown to be applied successfully to versatile microchip experiments such as GC mode experiments and an electrochemical cyanation reaction of pyrene as described in the previous Chapters. As another possibility of a microchannel-microelectrode chip, the electrode integrated in the microchannel chip was used as a micrometer-sized heater in the present study.

A microheater is a very important device for a miniaturized PCR (polymerase chain reaction) chip and a microreactor. A combination of a microchannel with a microheater provides certainly a new way to controlling chemical reactions in minute dimensions. In order to realize such a system, however, *in situ* and on-site observations of the temperature and solution-flow profiles in a microchannel-microheater chip are of primary importance. So far, the temperature profile of a solution in the vicinity of a heater in a microchannel has been studied by using a thermo-electric sensor. A fluorescence probe method, by using a thermochromic compound or system, is another candidate.[1,2] As the third possibility, the use of a polymer solution showing a lower critical solution temperature (LCST) is very attractive. As a representative example, an aqueous poly(N-isopropylacrylamide) (PNIPAM) solution exhibits LCST at around 32 °C. Below this temperature, the polymer is in the coil state and the solution is clear, while the solution becomes turbid above 32 °C owing to the coil-to-globular transition

of the polymer and simultaneous precipitation of polymer microparticles.[3-9] It has been reported that the phase transition of the PNIPAM solution is very sharp, and the precipitated PNIPAM particles above 32 °C can be seen easily under an optical microscope.[10,11] Therefore, the polymer solution would exhibit sensitively the temperature profile (i.e., below or above 32 °C) in a microchannel-microheater chip. As the advantage of the use of the phenomenon, furthermore, since precipitated PNIPAM particles can be seen under a microscope, a solution-flow profile could be also observed simultaneously as the formation area or profile of the precipitated particles in a microchannel. Thus, the use of a PNIPAM solution is very novel and promising to monitor both the temperature and solution-flow profiles in a microchannel-microheater chip.

As another interesting aspect into the phase transition of a PNIPAM solution, it has been reported that precipitated PNIPAM particles in water can be employed as an extraction medium for various water-soluble hydrophobic solutes.[12-15] Above LCST, namely, hydrated water molecules around the amido groups in PNIPAM (i.e., coil state) are pushed out to the surrounding water phase, so that the interior of the particle becomes hydrophobic (i.e., globular state), leading to precipitation of the particles. In the presence of both PNIPAM and a water-soluble hydrophobic solute, the solute is homogeneously solubilized in water below LCST, while that is likely to distribute to the hydrophobic interior of PNIPAM above 32 °C. In practice, such a system has been applied to simultaneous concentration/analysis of an ultratrace amount of a solute in water: porphine derivatives,[12] metal chelate complexes,[13-15] and so forth.[16] Although these studies have been conducted by bach experiments, the phase transition of a PNIPAM solution in a microchannel-microheater chip under solution-flow conditions

will be applied to automated and continuous concentration/analysis of an ultratrace amount of various analytes, which is another interesting target of the study.

In the present study, thermal phase transition behaviors of an aqueous PNIPAM solution in plastic microchannel-microheater chips were elucidated. The phenomenon was then applied to visualizing both temperature (i.e., below or above 32 °C) and solution-flow profiles in the microchannel as well as to automated concentration/ analysis of a dye molecule solubilized in water. Space- and time-resolved fluorescence spectroscopy of a thermo-sensitive dye (Rhodamine B) was also explored to monitor a temperature profile in a microchannel and the results were compared with those obtained by the phase-transition study. On the basis of such studies, furthermore, the fabricated microchannel-microheater chips were applied to a thermal synthetic reaction. The results on the thermal condensation reaction between benzaldehyde and malononitrile in the chip were also described.

8.2 Experimental

8.2.1 Chemicals and Sample Preparations

Thermal Phase Transition of an aqueous Poly(N-isopropylacrylamide) solution

N-Isopropylacrylamide (Wako Pure Chemicals Co. Ltd., GR grade) was purified by repeated recrystallizations from *n*-hexane. Polymerization of the monomer (2.4 g, 0.21 mol) in *t*-butanol (Wako Pure Chemicals Co. Ltd., GR grade) in the presence of 2,2'-azobis(isobutyronitrile) (Wako Pure Chemicals Co. Ltd., GR grade, 150 mg) was conducted by heating the solution at 70 °C for 15 h. The resultant PNIPAM was purified by repeated reprecipitations of the tetrahydrofuran solution into an enough amount of

dry diethyl ether. The polymer was then dissolved in a minimum amount of methanol and it was reprecipitated in distilled *n*-hexane. PNIPAM was collected by suction filtration and dried in vacuum. The average molecular weight of PNIPAM (M_n), determined in water by an Ostwald viscometer (25 °C) and the reported relationship ($[\eta]=14.5 \times 10^{-2} M_n^{0.5}$, where $[\eta]$ represents an intrinsic solution viscosity), was 5.2 x 10^5. Transmittance measurements of an aqueous PNIPAM solution (1 wt%) at various temperatures indicated that the solution exhibited reversible LCST at 30~32 °C. Although LCST has been reported to be 32 °C and is dependent on M_n of PNIPAM, the phase transition behavior was sharp enough for the present purpose of the study. Acridine Orange (Tokyo Kasei Kogyo Co. Ltd.) and Rhodamine B (RhB, Tokyo Kasei Kogyo Co. Ltd.) were used without further purification. Water was distilled and deionized prior to use (Advantec Toyo, GSR-200). The structural formulas of RhB and PNIPAM are shown in Figure 8-1.

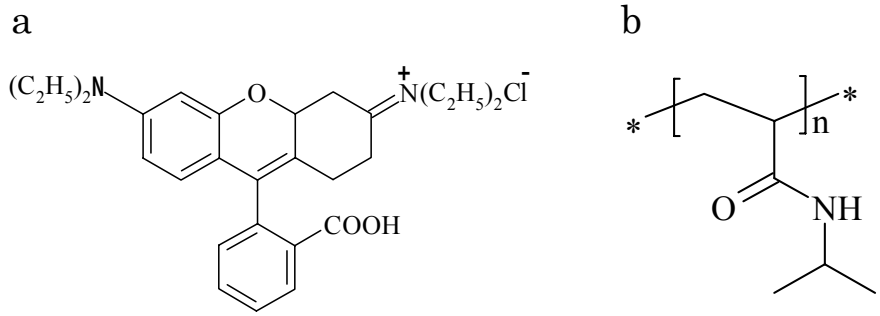

Figure 8-1 The structural formulas of RhB (a) and PNIPAM (b).

Thermal Synthetic Reaction between Benzaldehyde and Malononitrile

Benzaldehyde (BA), malononitrile (MN), and methanol, all purchased from Wako Pure Chemicals Co., Ltd., were used without further purification.

Benzilidenemalononitrile (BMN) was prepared by refluxing a methanol solution of BA and MN for 4 h. The structural formulas of BN, MN, and BMN are shown in Figure 8-2.

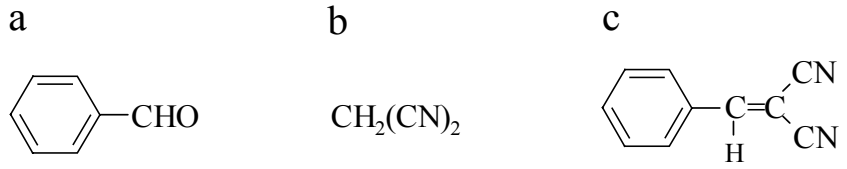

Figure 8-2 The structural formulas of BN (a), MN (b), and BMN(c).

For product analysis of the thermal synthetic reaction, the sample was collected from the exit of the microchannel-heater chip and analyzed by GC-MS (Shimadzu, QP5050). The absolute yield of benzilidenemalononitrile (BMN) as the product of the thermal synthetic reaction was determined on the basis of a calibration curve obtained by GC analysis using an authentic BMN sample obtained by a large-scale synthesis.

8.2.2 Fabrication of Polymer Microchannel-Microheater Chips

Polymer microchannel-microheater chips were fabricated on the basis of photolithograph/etching and imprinting methods as described in Chapter 5. The overall structural layout of a fabricated chip is illustrated in Figure 8-3. The dimension of the microchannel was 100 μm width x 20 μm depth. The width of the Au microheater (thickness 50 nm) was set 20 μm for the experiments of the thermal phase transition of an aqueous polymer solution. In the case of a thermal synthetic reaction, on the other hand, the width of the microheater was set 100 or 200 μm. In both cases, the heater was fabricated perpendicularly to the channel length as shown in Figure 8-3. Therefore, the

length of the heater was equal to the channel width (100 μm). Besides the heater part, the dimensions of the Au parts as connectors and bonding pads were designed to minimize heat generation. Analogous solution-flow system with that described in Chapter 2 was used. A model HG-100 potentiostat (Hokuto Denko Co. Ltd.) was used to apply a voltage to the microheater.

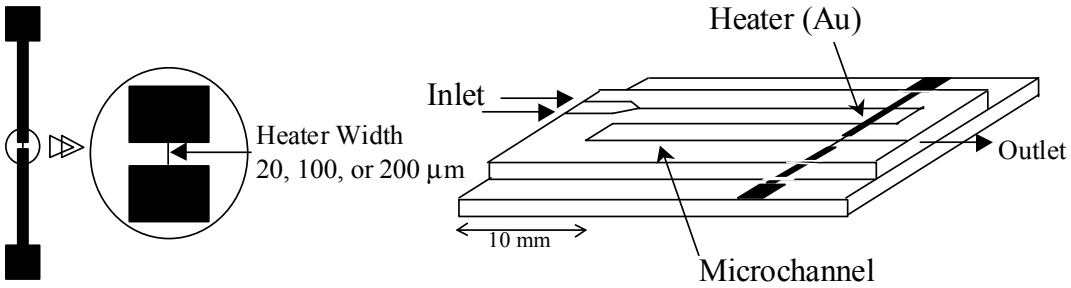

Figure 8-3 Schematic illustration of the fabricated polymer chip. The channel width and depth were 100 and 20 μm, respectively, and the width of the microheater was set 20, 100, or 200 μm.

8.2.3 Experimental Setup

Absorption spectroscopy was conducted by using a Hitachi UV3200 spectrophotometer. For observation of the phase-transition behavior of an aqueous PNIPAM solution, a microchannel-microheater chip was set on the stage of an optical microscope (Nikon, Optiphoto-2) and the images of the phase-transition were accumulated on a video recorder by using a CCD camera attached to the microscope as described in Chapter 2. Data analysis was made on the basis of the video data. For fluorescence spectroscopy of AO in a microchannel, the fluorescence

microspectroscopy system described in Chapter 3 was employed.

Picosecond fluorescence microspectroscopy was conducted by the system mentioned in Chapter 2 with slight modifications. The 532 nm laser pulses (repetition rate, 100 kHz; fwhm, 150 fs) from a femtosecond laser system were introduced to a confocal fluorescence microscope (Olympus, BX-50) and irradiated to the sample solution (spot size ~2 μm) in a microchannel-microheater chip through a super-long working distance objective (x 10, N.A.= 0.4). The fluorescence from the sample was collected by the same objective and passed through both a cut filter ($\lambda > 560$ nm) and a bandpass filter (570 ± 10 nm, Andover). The fluorescence was then led to a multichannel-plate photomultiplier tube (Hamamatsu, R3809U-50) equipped with a monochromator (Jobin Ybon, H-20, monitoring wavelength 570 nm) and analyzed by a single photon counting module (Edinburgh Instruments, SPC-300). Decay profiles were analyzed by using an iterative nonlinear-least-squares deconvolution method.

8.3 Results and Discussions

8.3.1 Temperature Profiles in Polymer Microchannel-Microheater Chip

In order to apply the chip to the thermal phase transition of an aqueous PNIPAM solution, temperature profiles of the solution phase in the microchannel as a function of an applied voltage (V) and a solution-flow velocity (u) should be known. Before discussing the results on the phase transition of PNIPAM, therefore, the performances of the fabricated microchannel-microheater chip are described below.

To study the temperature profile in the chip, the fluorescence lifetime of RhB was used. The primary deactivation path of the excited singlet state of RhB is the rotational

motions of the diethylamino group in RhB,[17] and the fluorescence lifetime of the dye decreases with increasing temperature. In practice, the fluorescence lifetime of RhB in water (aerated) decreased from 2.1 to 0.6 ns by elevating the temperature from 10 to 60 °C,[18] which was used as a calibration curve. An aqueous RhB solution (4.0×10^{-5} M, aerated) was introduced to the microchannel-microheater chip at several flow velocities and, the fluorescence lifetime (τ) of RhB in the aqueous phase (at the center of the channel width, excitation spot ~2 μm) was determined as a function of V and the distance (x) from the heater along the channel length. Figure 8-4 shows a typical example of the fluorescence decay profiles determined at several distances (x) in the downstream side of the heater: x = 0 (above the heater), 200, 500, and 1000 μm (V = 500 mV and u = 1 μl min^{-1}). Each decay profile was always fitted by a single exponential function irrespective of the conditions (i.e., x, V, and u), and τ increased with an increase in x, demonstrating the temperature gradient along the channel length. The temperature at each position was then estimated on the basis of the temperature dependence of τ determined in bulk water (data are not shown here). Analogous experiments with those in Figure 8-4 were conducted at various positions in the microchannel and the results at V = 500 mV and u = 1 or 2 μl min^{-1} are summarized in Figure 8-5 as the temperature profiles in the chip, where the minus or plus sign in the abscissa (distance = x) represents the upstream- or downstream-side of the heater, respectively. As seen in Figure 8-5 (a), the solution temperature was the highest (~47 °C) at x = 0 and u = 1 μl min^{-1}. The temperature is high enough to induce the thermal phase transition of an aqueous PNIPAM solution in the microchannel-microheater chip.

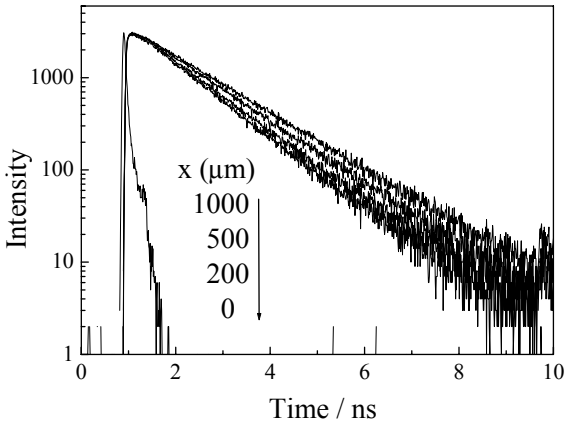

Figure 8-4 Fluorescence decays of RhB (4.0 x 10^{-5} M) in the aqueous phase in the microchannel at several positions; x = 0 (above the heater), 200, 500, and 1000 μm in the downstream-sides of the heater. *V* and *u* were set at 500 mV and 1 μl min^{-1}, respectively.

Figure 8-5 (a) also demonstrates that the solution temperature strongly depends on both x and *u*. The results are readily understood by the fact that a slower *u* (1 μl min^{-1}) at a given *V* allows for a longer heating time for the solution above the heater, so that this leads to the higher temperature at *u* = 1 μl min^{-1} as compared to that at *u* = 2 μl min^{-1}. Although it is discernible from Figure 8-5 (a), furthermore, the temperature profile of the solution along the channel length is quite different between the upstream- and downstream-sides, as shown in Figure 8-5 (b). The temperature gradient along x is relatively sharp in the upstream-side (x < 0), while the temperature decreases gradually with x in the downstream-side. This tendency was more pronounced at a faster solution-flow velocity. These results are also explained as follows. In the upstream-side, generated heat at x = 0 must diffuse against solution-flow and the temperature at each

position is determined primarily by a heating/cooling equilibrium. Cooling of the solution takes place very quickly and efficiently through heat transfer to the channel substrate irrespective of *u*, so that the temperature decreases sharply with x. On the other hand, since generated heat is forced to transfer to the downstream-side by pressure-driven flow, the temperature decreases gradually along x, as compared to the profile in the upstream-side. At u = 1 μl min^{-1}, cooling of the solution takes place more efficiently as compared to that at 2 μl min^{-1}, so that the temperature profile becomes sharper at a slower flow velocity. The solution temperature profile in the vicinity of the microheater depends strongly on both *u* and x, and such a temperature profile should reflect the thermal phase transition behaviors of an aqueous PNIPAM solution in the microchannel.

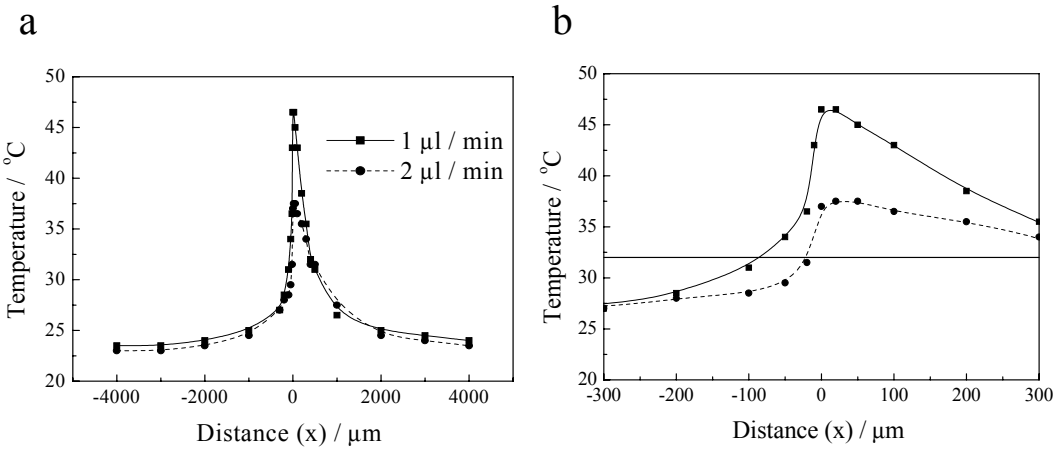

Figure 8-5 Temperature profiles of the solution phase in the microchannel at u = 1 and 2 μl min^{-1}, as estimated by the temperature dependent fluorescence lifetime of RhB. *V* was set at 500 mV. The minus and plus signs in the abscissa represent the distances (x) from the heater in the upstream- and downstream-sides, respectively. The horizontal line in (b) represents the contour line at 32 °C.

8.3.2 Thermal Phase Transition of an Aqueous PNIPAM Solution in Polymer Microchannel-Microheater Chip

An aqueous PNIPAM solution was brought into the microchannel-microheater chip and, V and u dependencies of the phase transition behaviors were studied. Figure 8-6 shows the optical micrographs of a PNIPAM solution (0.25 wt%) in the vicinity of the microheater. Upon application of V (400 mV, without solution-flow), the phase transition of the solution certainly took place as confirmed by formation of micro~submicrometer precipitates near the heater as seen as white dots in Figure 8-6 (a), indicating that the solution temperature of the precipitated region was above 32 °C. It is worth noting that the degree of polymerization of the present PNIPAM is not necessarily high enough (M_n = 5.2 x 10^5), so that the precipitated particles will be the aggregates of PNIPAM. At V = 500 mV, the precipitated regions increased in both the upstream- and downstream-sides of the heater as compared with those at V = 400 mV. Also, the lengths of the phase transition regions were almost equal to both sides of the heater, and it increased almost linearly with V: at 350 < V < 550 mV, ~20 μm/100 mV (data are not shown here). Therefore, the thermal phase transition of a PNIPAM solution is controllable by V in the microchannel-microheater chip.

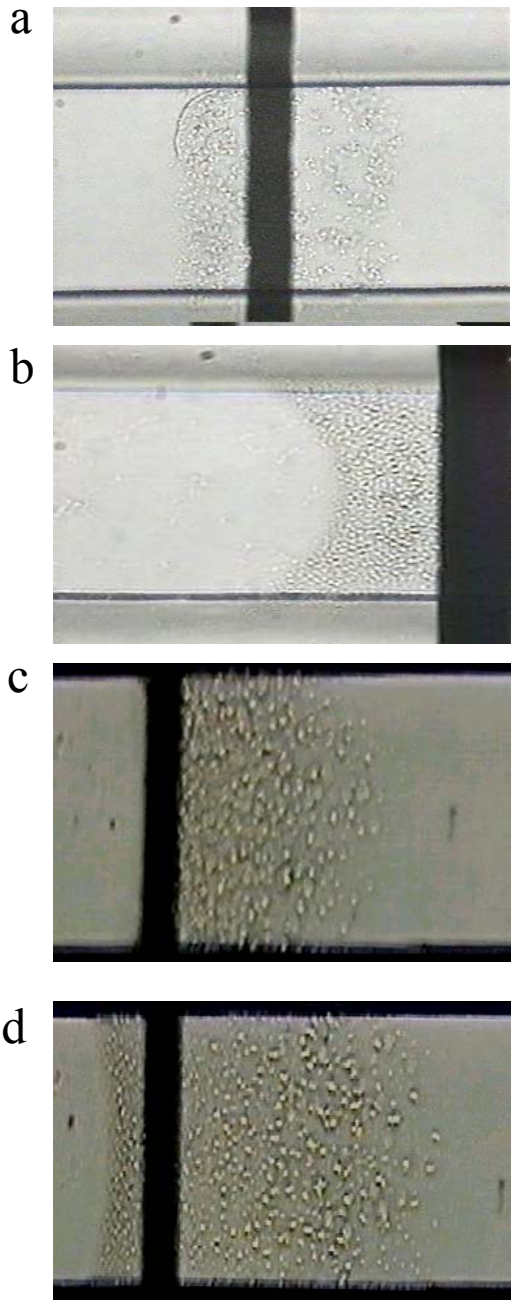

Figure 8-6 Optical micrographs of the phase transition behaviors of an aqueous PNIPAM solution (0.25 wt%) in the microchannel-microheater chip. **(**a) V = 400 mV without solution-flow, (b) u = 2 μl min^{-1} and V = 530 mV (upstream-side of the heater), **(**c) ν = 2 μl min^{-1} and V = 450 mV, and (d) u = 1 μl min^{-1} and V = 450 mV. The solution flows from the left- to the right-handed side.

Under solution-flow conditions, on the other hand, the characteristic flow profile in the microchannel was visualized by the use of the phase transition. A typical example of the results observed in the upstream-side of the heater is shown in Figure 8-6 (b) (u = 2 μl min^{-1}; V = 530 mV). It is well known that solution-flow in a microfluidic device having a low Reynolds number is described by the Navier-Stokes equation and best characterized by laminar flow. In a microchannel such as the present case, the flow velocity becomes maximum at the center of the channel width and the top front of the solution is described by parabolic flow. In practice, this can be seen in Figure 8-6 (b), where the formation edge of the PNIPAM particles is parabolic. Even at the same flow velocity (u = 2 μl min^{-1}, V = 450 mV), however, the parabolic profile of the particles could not be seen in the upstream-side of the heater, as shown in Figure 8-6 (c). At x < 0, the solution is cooled below 32 °C or PNIPAM particles are forced to transfer to the downstream-side by solution-flow. In the downstream-side, the solution is heated above the heater, so that the particles are produced along the parabolic solution-flow profile as shown in Figure 8-6 (c). At u = 1 μl min^{-1} and V = 450 mV, on the other hand, since generated heat is higher than that at u = 2 μl min^{-1}, PNIPAM particle formation is observed in both upstream- and downstream-sides of the heater (Figure 8-6 (d)).

Analogous experiments with those in Figure 8-6 were conducted at several V and u. The results are summarized in Figure 8-7, as V and u dependencies of the lengths of the particle formation regions in both the upstream- (a) and downstream-sides of the heater (b); the formation length is defined as the length from the heater edge to the formation edge of the particles at the center of the channel width. In the upstream-side, the formation length of the particles became longer with an increase in V, but was always shorter at u = 2 μl min^{-1} as compared to that at u = 1 μl min^{-1} at a given V (Figure 8-7

(a)). The curvature of the plot at u = 1 μl min^{-1} was also steeper than that at u = 2 μl min^{-1}. In the downstream-side (Figure 8-7 (b)), on the other hand, the formation length increased almost linearly with V, and was almost independent of u. These results are explained on the basis of the data in Figure 8-5. The horizontal line inserted in Figure 8-5 (b) represents the contour line at 32 °C. Figure 8-5 (b) indicates that the formation length of the particles (i.e., the region above 32 °C) in the upstream-side ($x < 0$) at u = 1 μl min^{-1} should be longer than that at 2 μl min^{-1}. This agrees very well with the results in Figure 8-7 (a). Although a quantitative discussion is very difficult, both heating and cooling of the solution take place simultaneously and the solution temperature under given conditions is determined by the heating/cooling equilibrium. In the upstream-side ($x < 0$), heating of the solution takes place more efficiently at a slower flow velocity, so that the larger V dependence is observed at u = 1 μl min^{-1} as compared to that at u = 2 μl min^{-1}. In the downstream-side, on the other hand, PNIPAM particles should produce in the whole region at $0 < x < 300$ μm irrespective of u, as the temperature profiles in Figure 8-5 (b) demonstrate. These predictions were certainly confirmed by the present results in Figure 8-7 (b), in which the slope at u = 1 μl min^{-1} almost agreed with that at u = 2 μl min^{-1}. The temperature profile (i.e., below or above 32 °C) in the microchannel-microheater chip was visualized successfully on the basis of the thermal phase transition of a PNIPAM solution and, the results in Figure 8-7 agreed very well with those in Figure 8-5. All of the results are explained by the single context as described above.

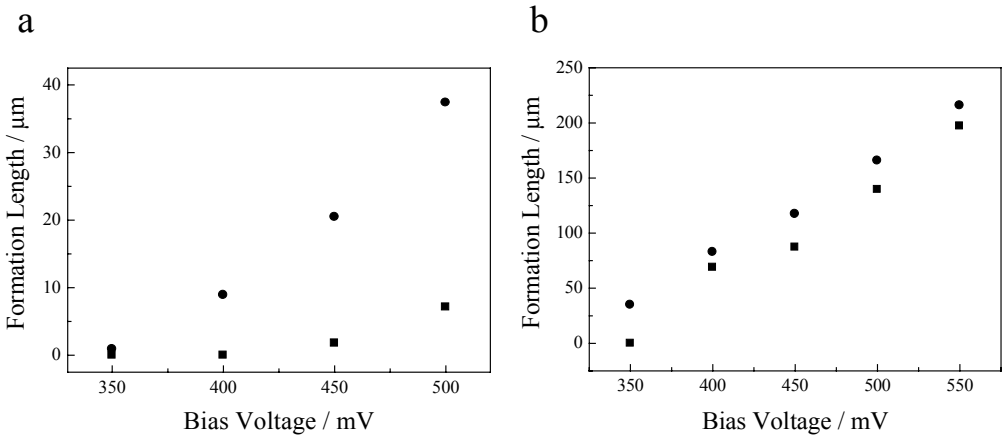

Figure 8-7 The V and u dependencies of the formation lengths of the PNIPAM particles in the upstream- (a) and downstream-sides of the heater in the microchannel (b); u = 1.0 (♦) and 2.0 μl min^{-1} (■). The concentration of PNIPAM was set 0.25 wt%.

8.3.3 Application of Thermal Phase Transition of PNIPAM to Automated Concentration of a Dye under Solution-Flow Conditions

The thermal phase transition of the PNIPAM solution in the microchannel-microheater chip was also applied to controlling concentration/accumulation of a trace amount of an analyte by switching on/off of a bias voltage to the heater. As a water-soluble hydrophobic dye, acridine orange (AO) was chosen, since AO shows strong fluorescence in hydrophobic environments while that is a weak emitter in water.[19] In the actual experiments, an aqueous PNIPAM solution (0.25 wt%) containing AO (1.0 x 10^{-3} M) was introduced to the chip at u = 2 μl min^{-1} and the fluorescence from AO was monitored by switching on/off of V. Figure 8-8 shows the fluorescence image of the microchannel in the vicinity of the microheater (V = 400 mV, excited at 488 nm). It is seen clearly from Figure 8-8 that the precipitated PNIPAM particles

exhibit fluorescence while the solution phase below LCST does not show fluorescence. It is worth emphasizing that the parabolic flow profiles in the channel can also be seen as the fluorescence image in both the upstream- and downstream-sides of the heater, similar to the image in Figure 8-6. The brightest region of the photograph is the image just above the microheater (i.e., seen as a band structure) and, the fluorescence intensity becomes weaker on going from the heater to the downstream-side, suggesting that the number of the precipitated particles decreases along this direction. Qualitatively, the results agree very well with those in Figures 8-5 and 8-7.

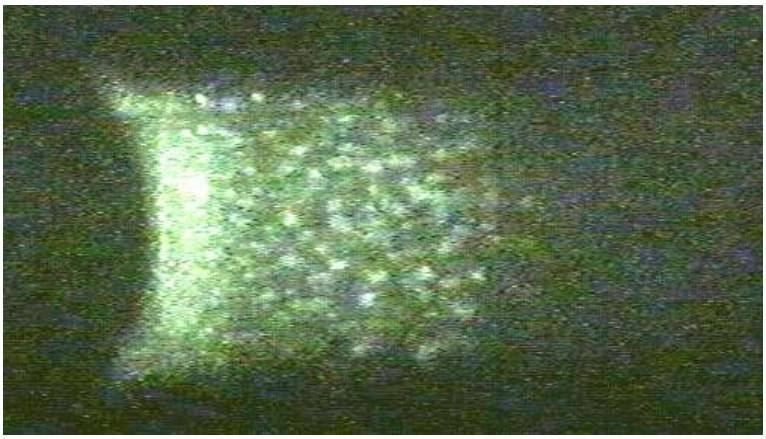

Figure 8-8 Fluorescence image of AO (1.0×10^{-3} M) in the precipitated PNIPAM particles in the microchannel under the conditions of PNIPAM = 0.25 wt%, V = 400 mV, and u = 2 μl min^{-1}. Excitation and monitoring wavelengths were set at 488 and 525 nm, respectively.

Accumulation/concentration of AO in the particles was also followed as the time (t) course of the fluorescence intensity. A typical example of the results monitored at x = 0 is shown in Figure 8-9 (a) (V = 500 mV, u = 2 μl min^{-1}, PNIPAM = 0.25 wt%, excitation spot size ~2 μm). At t = 0 (i.e., V = 0), the weak AO fluorescence from the

aqueous solution was observed at around 525 nm: the sharp peak at 488 nm is scattering of excitation light. Upon applying *V*, the fluorescence intensity increased without any change in the spectral band shape and leveled-off at ~20 s. As shown in Figure 8-9 (b), the time necessary to reach the saturated fluorescence intensity was dependent on *V* and needed a longer time at a lower *V*, since the heating/cooling rate leading to an equilibrium temperature depended on *V*. Switching off of *V* renders fast cooling of the solution, so that the fluorescence intensity decreases very sharply with *t*. On the other hand, the absolute fluorescence intensity was stronger at V = 500 mV as compared with that at V = 400 mV. This will indicate that the number of the precipitated PNIPAM particles is larger at a higher *V* and, therefore, the total concentration of AO accumulated in the particles could be higher at a higher *V*. Unfortunately, the extraction efficiency of AO to the PNIPAM particles has not been estimated on the basis of the fluorescence intensity changes with *t* or *V*, since distribution of AO into the PNIPAM particle results in the change in the fluorescence quantum yield and this has not been evaluated in the present stage of the investigation. It has been reported, however, that the distribution coefficient of a solute, defined as $K = [\text{solute}]_{\text{PNIPAM}}/[\text{solute}]_{\text{water}}$, is in the order of 10^2~10^3, depending on the hydrophobicity of a solute. In the present experiments, since the volume ratio of the particle phase to the water phase varies with *u* and *V*, a comparison of the present system with the reported one is not straightforward. Judging from the hydrophobic nature of AO and the reported value for anthracene,[20] however, the *K* value of the present system would be ~300. Although further detailed studies are necessary to discuss quantitatively the experimental observations, the idea of automated concentration/analysis of a solute by using a microchannel-microheater chip and the phase transition of PNIPAM was demonstrated successfully.

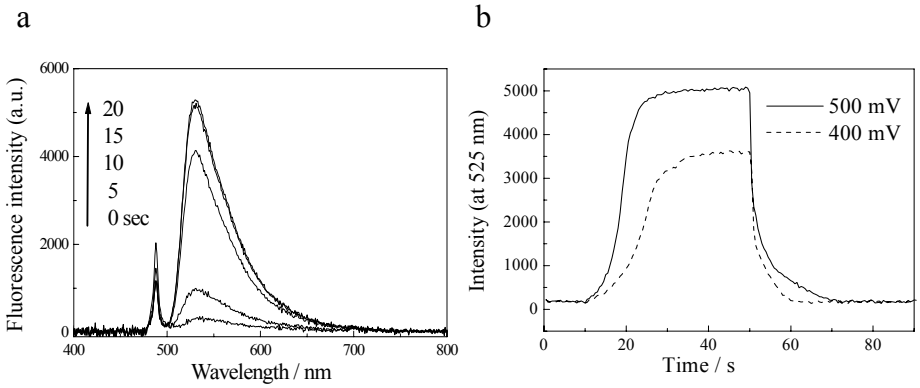

Figure 8-9 (a) Temporal profiles of the AO fluorescence spectrum upon an application of a bias voltage at 500 mV (PNIPAM = 0.25 wt% and u = 2 μl min^{-1}, excitation spot ~2 μm). (b) The time responses of the AO fluorescence intensity upon switching on/off of V (400 or 500 mV).

8.3.4 Application of Polymer Microchannel-Microheater Chips to Thermal Synthetic Reaction

In order to apply the fabricated chip to a thermal synthetic reaction, the temperature profiles of the solution phase in the micorchip used in this section were studied by the analogous experiments with those described previously (Section 8.3.1). A methanol solution of RhB (4.9 x 10^{-4} M, aerated) was introduced to the microchannel-microheater chip and the fluorescence lifetime of RhB in the solution phase (at the center of the channel width, excitation wavelength = 532 nm, excitation spot ~2 μm) was determined as a function of V and the distance from the heater along the channel length (x). The decay profiles were always fitted by single exponential functions analogous to those observed in bulk methanol. On the basis of τ observed in the chip and the temperature dependence of τ in bulk methanol, the solution-temperature profiles in the microchip were obtained. A typical example of the

results at u = 0.1 μl min^{-1} (heater width = 100 μm) is shown in Figure 8-10, where zero and the plus/minus signs in the abscissa scale represent the position above the microheater and the downstream-/upstream-sides of the heater, respectively. The results in Figure 8-10 demonstrate clearly that the solution-temperature is dependent strongly on V and x. The solution-temperature was the highest just above the heater (x = 0) at a given V and increased with increasing V. As an example, the temperature just above the heater was 37, 28, or 23 ºC at V = 0.7, 0.5, or 0.3 V, respectively. Furthermore, the solution-temperature decreased sharply at -100 < x < +100 μm, demonstrating rapid cooling in the microchannel. At a faster flow velocity (0.2 or 0.3 μl min^{-1}), analogous temperature profiles with those in Figure 8-10 were observed, although the solution-temperature at given V and x was lower than the relevant value at u = 0.1 μl min^{-1}. Since a slower u at a given V allows a longer heating time for the solution above the heater, the results mentioned above are the reasonable consequence.

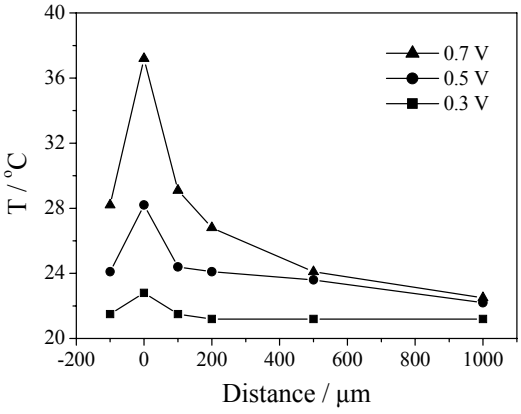

Figure 8-10 Solution-temperature profiles in the vicinity of the microheater (width = 100 μm) in the microchannel. The minus and plus signs in the abscissa represent upstream- and downstream-sides of the microheater (x = 0), respectively. The solution-flow velocity was set at 0.1 μl min^{-1}.

Since the solution-temperature profiles in the chip was confirmed, the chip was then applied to a thermal synthetic reaction. A reaction studied was the condensation reaction between BA and MN in methanol, giving BMN as the product. BMN and its derivatives have been reported to be effective anti-fouling agents, fungicides and insecticides. Therefore, the compounds are of primary importance for applications in industry, agriculture, medicine, and biological science.[21] Conventionally, the condensation of aromatic aldehydes and MN is catalyzed by a base such as piperidine, sodium ethoxide, or sodium hydroxide in organic media. Lewis acids also catalyze the reaction. On the other hand, Bigi et al. recently reported that the reaction between BA and MN proceeded without a base,[21] which was meaningful as green chemistry. Therefore, the condensation reaction between BA and MN in the microchip is expected to be proceeded without a base catalyst.

Methanol solutions of BA and MN (both 4 x 10^{-2} M) were brought separately into the channel-heater chip by pressure driven flow with the same flow velocity (u = 0.1 ~ 0.3 μl min^{-1}) and the thermal reaction was allowed by applying a voltage to the heater (V = 0.3 - 0.7 V). Analysis of the reaction mixture, sampled from the channel exit, by GC-MS demonstrated that the product was BMN and, no other component other than unreacted BA and MN was confirmed under the present experimental conditions for GC-MS.

Although the reaction between BA and MN proceeded slightly (~ 6% yield) even at room temperature without V, the BMN yield increased upon applying V to the heater. When the microheater (width = 100 μm) was set at 1 mm in the downstream-side of the channel junction, the BMN yield at V = 0.7 V and u = 0.1 μl min^{-1} was ~25% and it decreased with increasing u as shown in Figure 8-11 (closed circles). Although the use

of the chip having the microheater width of 200 μm improved the yield as the data were included in Figure 8-11 (open circles), the optimum yield under the present conditions was ~45% (V = 0.7 V and u = 0.1 μl min^{-1}). The results are readily understood by flow characteristics in a microchannel.[22] Namely, two methanol solutions are not mixed immediately at the channel junction, but mixed gradually along solution-flow to the downstream side of the junction on the basis of laminar flow. The spatial position of the heater in the channel (0.1 mm from the junction) is the primary reason for the low BMN yield in Figure 8-11.

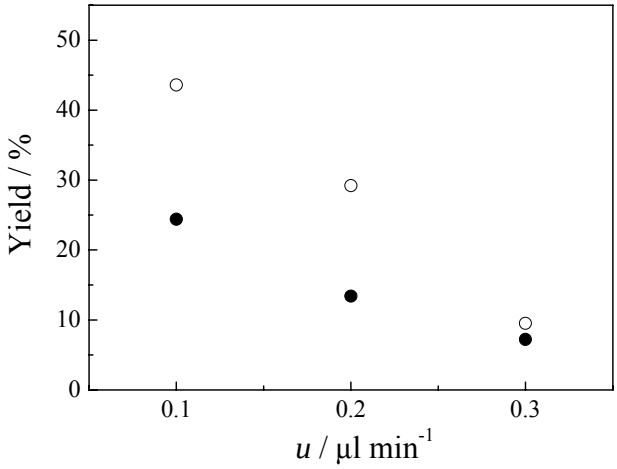

Figure 8-11 Flow velocity (u) dependences of the BMN yield (V = 0.7 V). The microheater (width = 100 μm (●) or 200 μm (○)) in the microchannel was set at 1 mm from the channel junction.

In order to improve the reaction yield, therefore, the microheater in the channel was set at 5.9 cm from the junction (see also Figure 8-3) to allow efficient mixing of the two solutions before the thermal reaction above the heater. The results by using the 100

μm microheater width are shown in Figure 8-12. At V = 0.7 V and u = 0.1 μl min^{-1} (closed triangles), the BMN yield was ~50%, which was higher than the relevant value in Figure 8-11 (~25%). The homogeneous solution mixed by self-diffusion between the BA and MN solutions in the microchannel is heated above the heater and the reaction proceeds along solution-flow to the downstream-side of the heater. The solution-temperature becomes higher at higher V and a slower u, so that the BMN yield increased with increasing V and decreasing u. The results are in good accordance with those in Figure 8-10.

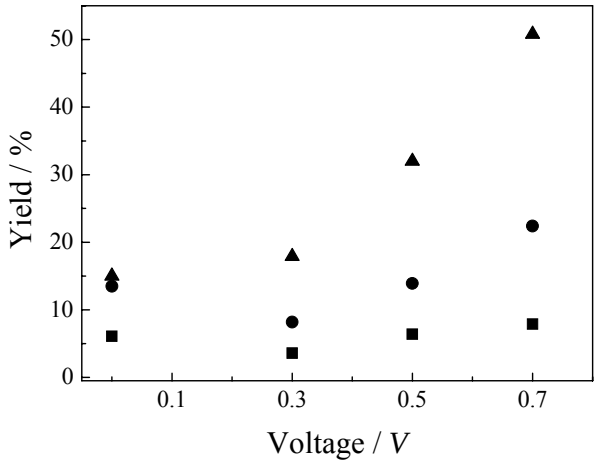

Figure 8-12 Applied voltage dependence of the BMN yield at the flow velocity of 0.1 (▲), 0.2 (●), or 0.3 μl min^{-1} (■). The chip with the heater width of 100 μm was used.

Analogous experiments with those in Figure 8-12 were also conducted by using the chip having the heater-width of 200 μm (set at 5.9 cm from the junction). The results at V = 0.7 V are summarized in Figure 8-13 as the flow velocity dependence of the BMN yield. The yield increased from 20 to 96% by slowing u from 0.3 to 0.1 μl min^{-1} and, at

a given *V*, that was almost two times higher than the relevant value in Figure 8-12. The solution-temperature in the 200 μm-wide heater chip, estimated by the τ values of RhB, was almost the same with that by the chip having the 100 μm-wide heater as mentioned above. Beside solution temperature itself (i.e., *V*), therefore, the heating time of the solution above the heater (i.e. heater-width and *u*) is another important factor governing the BMN yield in the microchip. At u = 0.1 μl min^{-1}, the resident time of the solution in the channel (from the channel junction to the channel exit) is calculated to be 84 s. At V = 0.7 V and u = 0.1 μl min^{-1}, therefore, almost quantitative yield (96%) was attained by using the 200 μm-wide heater chip with the reaction time of 84 s.

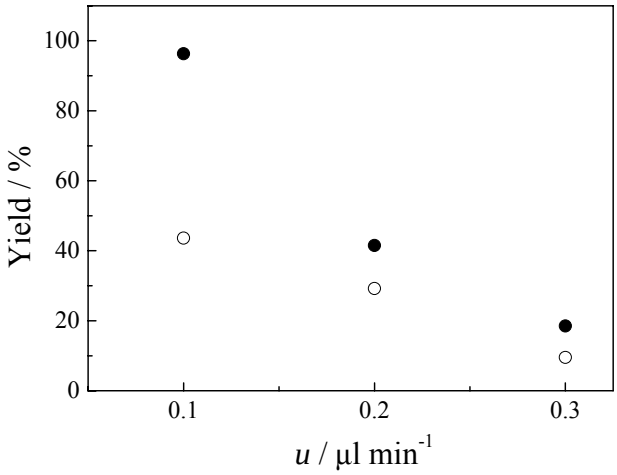

Figure 8-13 Flow velocity dependence of the BMN yield (V = 0.7 V). The microheater (width = 200 μm (●) and 100 μm (○)) in the microchannel was set at 5.9 cm from the channel junction.

It is worth noting that the BMN yield by the microchannel-microheater chip is 96%, while that by bulk experiments (reflux in methanol) is ~70%. It is certainly true that the

yields by the two experiments cannot be compared directly. For a chemical reaction in a microchannel, however, the reaction yield or product selectivity becomes sometimes higher than that by the relevant bulk experiment,[22,23] and such results have been discussed in terms of a high surface area/volume ratio (A/V) of a microchannel or liquid/liquid interface produced in a channel. As an example, since the A/V ratio of a microchannel is very large as compared to that of a conventional glass vessel, the surface properties of the channel themselves influence the product yield/selectivity of a chemical reaction. In the present case, however, the channel dimension is not small enough to influence the reaction yield. As another aspect, a high A/V ratio of a microchannel is very favorable for fast heating/cooling of a reaction mixture. In the present system, although the solution-temperature is not so high, the fast heating/cooling rate in the microchip will be one of the reasons for the high BMN yield. However, thermodynamics and kinetics of the reaction in the microchip should be essentially the same with those in a bulk solution. As another important aspect, therefore, one-directional solution-flow of the reactant solution in the microchannel plays crucial roles in determining the yield. In the microchannel under solution-flow, namely, the reactant solution is heated only once in a short time (0.28 s for the 200 μm-wide heater at u = 0.1 μl min^{-1}) and the product is cooled rapidly after the solution being passed over the microheater. Such a situation is essentially different from that of a chemical reaction in a conventional flask. This will be another reason for the high BMN yield (96%) in the microchip.

8.4 Conclusion

In the present study, plastic microchannel-microheater chips were fabricated to study temperature/solution-flow profiles in the microchannel as well as to test an idea to automated concentration/analysis of a trace amount of an analyte on the basis of the thermal phase transition of an aqueous PNIPAM solution. Indeed, control the phase transition of a PNIPAM solution by both the applied voltage to the heater and the solution-flow velocity was succeeded. Furthermore, the characteristic solution-flow profile in the microchannel was visualized by the use of the PNIPAM particle formation. Besides the studies on the phase transition, space- and time-resolved fluorescence spectroscopy was conducted and the solution temperature profile in the microchannel-microheater chip was estimated. The results explained very well the bias voltage and the solution-flow velocity dependencies of the phase transition behaviors. The fabricated chip combined with the phase transition of PNIPAM was also shown to be applied to automated concentration/analysis of a water-soluble hydrophobic solute. Since the fabricated chip can control the solution temperature in the microchannel spatially and temporally, the system can be applied to various thermal synthetic reactions in minute dimensions. In practice, the fabricated chip was applied to the thermal synthetic reaction between benzaldehyde and malononitrile, and the product yield of benzilidenemalononitrile as high as ~96% was attained by using the microchannel chip under optimum conditions (i.e., high applied voltage and slow solution-flow velocity). It was concluded that one-directional solution-flow of the reactant solution in the microchannel played crucial roles in determining the reaction yield in addition to fast heating/cooling in the channel. Furthermore, it is worth emphasizing that, after experiments, the microheater, connectors, and bonding pad in

the chip can be removed very easily by mechanical pealing of the channel and heater substrates. Expensive Au can be thus recovered and used again if needed. Plastic microchannel-microheater chips are thus employed as a very versatile and inexpensive (disposable) microreactor.

8.5 References

1) Sun, K.; Yamaguchi, A.; Ishida, Y.; Matsuo, S.; Misawa, H. *Sens. Actuat. B: Chem.* **2002**, 84, 283-289.
2) Ross, D.; Gaitan, M.; Locascio, L. E. *Anal. Chem.* **2001**, 73, 4117-4123.
3) Heskins, M.; Guillet, J. E. *J. Macromol. Sci., Chem.* **1968**, 1441.
4) Yamamoto, I.; Iwasaki, K.; Hirotsu, S. *J. Phys. Soc. Jpn.* **1989**, 58, 210-215.
5) Winnik, F. M. *Macromolecules* **1990**, 23, 233-242.
6) Winnik, F. M. *Polymer* **1990**, 30, 2125-2134.
7) Chee, C. K.; Rimmer, S.; Soutar, I.; Swanson, L. *Polymer* **1997**, 38, 483-486.
8) Wu, C.; Wang, X. H. *Phys. Rev. Lett.* **1998**, 80, 4092-4094.
9) Wang, X. H.; Wu, C. *Macromolecules* **1999**, 32, 4299-4301.
10) Ishikawa, M.; Misawa, H.; Kitamura, N.; Masuhara, H. *Chem. Lett.* **1993**, 481-484.
11) Ishikawa, M.; Misawa, H.; Kitamura, N.; Fujisawa, R.; Masuhara, H. *Bull. Chem. Soc. Jpn.* **1996**, 69, 59-66.
12) Saitoh, T.; Ohkubo, S.; Matsubara, C. *Chem. Lett.* **1999**, 151-152.
13) Saitoh, T.; Ohyama, T.; Takamura, K.; Sakurai, T.; Kaise, T.; Matsubara, C. *Anal. Sci.* **1997**, 13, 1-4.
14) Fujinaga, K.; Yamato, Y.; Seike, Y.; Okumura, M. *Anal. Sci.* **1997**, 13, 141-144.
15) Saitoh, T.; Ohyama, T.; Sakurai, T.; Kaise, T.; Takamura, K.; Suzuki, Y.; Matsubara,

C. *Talanta* **1998**, 46, 541-550.

16) Matsubara, C.; Izumi, S.; Takamura, K.; Yoshioka, H.; Mori, Y. *Analyst* **1993**, 118, 553-556.

17) Ishizaka, S.; Kitamura, N. *Bull. Chem. Soc. Jpn.* **2001**, 74, 1983-1998.

18) Habuchi, S. Ph.D. Thesis, Hokkaido University, **2001**.

19) Murad, M. M. *J. Fluoresc.* **1999**, 9, 257-263.

20) Saitoh, T.; Yoshida, Y.; Mastudo, T.; Fujiwara, S.; Dobashi, A.; Iwaki, K.; Suzuki, Y.; Matsubara, C. *Anal. Chem.* **1999**, 71, 4506-4512.

21) Freeman, F. *Chem. Rev.* **1980**, 80, 329-350.

22) Bigi, F.; Conforti, M. L.; Maggi, R.; Piccinno, A.; Sartori, G. *Green Chem.* **2000**, 2, 101-103.

23) Burns, J. R.; Ramshaw, C. *Chem. Eng. Res. Des.* **1999**, 77, 206-211.

24) Ueno, M.; Hisamoto, H.; Kitamori, T.; Kobayashi, S. *Chem. Commun.* **2003**, 936-937.

Chapter 9

Summary and Conclusions

Polymer microchannel chips and chips integrated with functional elements such as microelectrodes and microheaters were fabricated by photolithography/imprinting methods. Mass transfer and chemical reaction processes in the fabricated microchannel chips were then studied on the basis of microspectroscopy and microelectrochemical techniques in special reference to demonstrate the rich chemistry of microchips.

So far, a micromachined silicon or glass channel has been employed as a microchip. Integration of a miniaturized total analysis system and a chemical system on a single chip has been also demonstrated. Besides these chips, polymer microfluidic devices such as those made of PDMS and PMMA have been reported. Among the various fabrication methods of microchips so far proposed, a new and novel fabrication methodology toward a polymer microchannel chip and the chip integrated with microband electrodes was demonstrated in the present thesis. An application of a polymer channel chip and an imprinting method is very promising, since an arbitrary-structured channel chip (size, shape, length, and so on) can be easily fabricated. A solution-flow system based on pressure driven flow can be also combined with the fabricated channel chip, which enable one to control a solution-flow velocity arbitrary (Chapter 2). Although durability of polymer chips might be lower in comparison with that of silicon channel chips, it was shown that the polymer channel chip was potential enough for the present purpose of the study (Chapters 2 ~ 8).

Microfluidic liquid/liquid extraction devices have been sometimes reported. In the case of such devices, nonetheless, since flow characteristics in a microchannel are

governed by several factors such as a channel dimension, channel geometries, and a flow velocity, the liquid/liquid extraction efficiency should be studied systematically as a function of these factors. Also, *in-situ* observations of the mass-transfer processes of a solute across the liquid/liquid interface in a microchannel are worth to be explored to optimize necessary conditions for realizing an ideal liquid/liquid extraction microdevice and an interfacial chemical reaction. Therefore, the liquid/liquid extraction processes in the microchannel chip were studied on the basis of spatially-resolved fluorescence spectroscopy. Along the line of the study, it was confirmed that water/oil extraction proceeded with solution-flow and was governed by the contact time between the two phases. A one-dimensional mass-transfer model along the channel-width direction explained very well the relevant dynamics. Furthermore, in order to study shape effects on the extraction efficiency, polymer chips having non-flat-side-walled microchannel chips (symmetrical and unsymmetrical zigzag-side walled) were fabricated and were applied to liquid/liquid extraction of a metal chelate complex. It is worth empathizing that the study has demonstrated for the first time that the liquid/liquid extraction efficiency of the chelate in the channel is governed by the side-wall structures of the channel (Chapter 3).

These studies demonstrated that the mass transfer processes of a solute across a water/oil interface in a microchannel and the liquid/liquid interfacial structures could be manipulated through a solution-flow velocity, channel structures, and so forth. These should be applied to a chemical reaction in a microchip, which is one of the present purposes of the study: manipulation of chemistry in a microchip. In order to realize an oil/water interfacial chemical reaction system, therefore, photocyanation of pyrene in a microchannel was studied as a function of channel geometries and solution-flow

velocity. The pyrene cation radical generated by a photoinduced electron transfer reaction with an electron acceptor was attacked by a cyanide ion at the oil/water interface in the channel, and 1-cyanopyrene was confirmed to be produced on the basis of product analysis of the solution mixture sampled from the channel exit. The yield of the interfacial photoreaction was shown to be controlled through the specific interface area and the contact time between the two phases in the channel chip. Under optimum conditions, the cyanated product yield of 86% was attained with the reaction time of 210 s by the channel chip (Chapter 4).

As one of the important achievements of the study, polymer microchannel-microelectrode chips were shown to be fabricated very easily with a technique-free method. The characteristics of the electrochemical responses of an electrode(s) incorporated in a microchannel chip fabricated were then studied in detail. It was demonstrated that the electrochemical responses of the electrode in the microchannel were different from those without the channel cover. Such characteristics of the responses reflected on the collection efficiency of an oxidized solute by an adjacent electrode determined by the generation-collection mode experiments. Namely, the collection efficiency in the channel was about two-times higher than that in the absence of a channel substrate, since the space around the working electrode was restricted in the microchannel. Furthermore, the collection efficiency as high as ~90% was obtained in the microchannel under the solution-flow conditions. A restricted space and solution-flow in the microchannel enable one to make efficient mass-transport of an electrochemical specimen, leading to such a high collection efficiency, not realized in a bulk system. Numerical simulations also demonstrated the characteristics of the electrochemical responses of the electrode in the channel (Chapter 5).

As an example of unique experiments by using a microchannel-electrode chip, furthermore, a spectroelectrochemical study on the perylene cation radical generated at the electrode integrated in a channel chip was explored. Usually, a spectroelectrochemical study has been conducted by using an optically-transparent thin-layer electrode. In this thesis, the perylene cation radical generated at the electrode in the channel chip was shown to be monitored quantitatively on the basis of *in-situ* absorption microspectroscopy. Furthermore, the formation efficiency of the cation radical was studied as a function of electrode geometries, an applied potential, and a solution-flow velocity. The study demonstrated quantitatively formation of the dimer cation radical of perylene for the first time. A space-resolved spectroscopy and solution-flow experiments demonstrated the formation and disappearance processes of both monomer and dimer cation radicals of perylene (Chapter 6).

On the basis of the characteristic electrochemical behaviors of the electrode incorporated in a microchannel, one-step electrochemical cyanation reaction of pyrene in the microchannel-electrode chip was also conducted. The pyrene cation radical generated at the electrode in the channel was reacted with a cyanide ion, and thus resulted in formation of 1-cyanopyrene as the final product of the reaction. The product yield and selectivity of 1-cyanopyrene were studied as a function of the electrode geometries and solution-flow velocity. In the microchip, it was shown that the product selectivity was improved in comparison with that by the relevant large-scale reaction, owing to the one-directional solution-flow in the microchannel. The electrochemical reaction mechanisms were elucidated on the basis of *in-situ* absorption microspectroscopy of the reaction intermediate and numerical simulations of the mass transfer processes in the microchannel (Chapter 7).

The microchannel-electrode chip fabricated was also shown to be applicable to a microchannel-heater chip. As an example along the line of the study, thermal phase transition of an aqueous poly(*N*-isopropylacrylamide) (PNIPAM) solution was studied as a function of several parameters. The study demonstrated that the phase transition of an aqueous PNIPAM solution certainly provide information about the solution-temperature and solution-flow profiles in the channel. By utilizing the thermal phase transition of PNIPAM in the channel, the system was also applied to simultaneous concentration/analysis of an ultratrace amount of a solute in water. Furthermore, the microchannel-heater chip was applied to the thermal synthetic reaction between benzaldehyde and malononitrile in methanol. One-directional flow of the reactant solution and efficient heating/cooling in the channel were shown to be the important factors in determining the reaction yield. Under optimum conditions, benzilidenemalononitrile as the product of the reaction was obtained in a 96% yield with the reaction time of 84 s. (Chapter 8).

The fabrication methods of polymer microchannel chips were developed on the basis of technique-free lithography and an imprinting method. This is one of the most important achievements of the present study. Fabrication of a channel-electrodes chip can be conducted without any special facilities and instruments, and is easily performed in an ordinary chemical laboratory. In spite of the easy fabrication methods, the solution-flow characteristics in the polymer microchannel were shown to be almost the same as those by a theoretical prediction for an ideal channel fabricated on a silicon or glass substrate. As demonstrated in the thesis, furthermore, the spatially-resolved spectroscopy and microelectrochemical measurements of a solute in a microchannel can provide useful information to analyze the kinetics and dynamics of various reactions,

including diffusion, adsorption, and extraction processes of a solute. Besides applications of microfluidic devices to μ-TAS and lab-on-a-chip systems, polymer microfluidic channel chips and its combination with microspectroscopy and microelectrochemistry play decisive roles in various fields of science. At the present, unfortunately, the microchip chemistry is not so common. Nonetheless, the microchip chemistry will certainly change the chemistry in the next generation.

Acknowledgments

I would like to express my science gratitude to Prof. Noboru Kitamura for his continuing guidance and stimulating criticisms throughout the works of this thesis.

I am much grateful and indebted to Prof. Haeng-Boo Kim, the University of Tokyo, for his valuable discussions and advices.

I wish to express my gratitude to Dr. Yasuyuki Tsuboi, and Dr. Shoji Ishizaka for helpful suggestions and discussions.

I am much grateful to Prof. Hiroaki Misawa (present address, Hokkaido University), Dr. Shigeki Matsuo, Dr. Akira Yamaguchi (present address, Tohoku University), and Mr. Tomonobu Tokunaga, The University of Tokushima, for their kind help to fabricate silicon templates.

I am much grateful to Prof. Kohei Uosaki and Prof. Kei Murakoshi for the examination of this thesis.

I wish to thank Ms. Yukiko Hosoda, Ms. Chiaki Iwasaki, and other members of the Analytical Chemistry Laboratory (Kitamura Laboratory) for their collaborations in the researches, Division of Chemistry, Graduate School of Science, Hokkaido University.

Sapporo, Hokkaido (2004) Kosei UENO

Publication Lists

1) Kim, H.-B.; Ueno, K.; Chiba, M.; Kogi, O.; Kitamura, N.

"Spatially-Resolved Fluorescence Spectroscopic Study on Liquid/Liquid Extraction Processes in Polymer Microchannels"

Anal. Sci., **2000**, 16, 871-876

2) Ueno, K.; Kitagawa, F.; Kim, H.-B.; Tokunaga, T.; Matsuo, S.; Misawa, H.; Kitamura N.

"Fabrication and Characteristic Responses of Integrated Microelectrodes in Polymer Channel Chip"

Chem. Lett., **2000**, 29, 858-859

3) Ueno, K.; Kitagawa, F.; Kitamura, N.

"Photocyanation of Pyrene across an Oil/Water Interface in a polymer Microchannel Chip"

Lab. Chip, **2002**, 2, 231-234

4) Ueno, K. Kim, H.-B.; Kitamura, N.

"Channel Shape Effects on Solution-Flow Characteristics and Liquid/Liquid Extraction Efficiency in Polymer Microchannel Chips"

Anal. Sci., **2003**, 19, 391-394

5) Ueno, K.; Kim, H.-B.; Kitamura, N.

"Characteristic Electrochemical Responses of Polymer Microchannel-Microelectrode Chip"

Anal. Chem., **2003**, 75, 2086-2091

6) Kitamura, N.; Hosoda, Y.; Iwasaki, C.; Ueno K.; Kim, H.-B.

"Thermal Phase Transition of an Aqueous Poly(N-isopropylacrylamide) Solution in a Microchannel-Microheater Chip"

Langmuir, **2003**, 19, 8484-8489

7) Ueno, K.; Kitamura, N.

"A Spectroelectrochemical Study on Perylene Cation Radical in Polymer Microchannel-Microelectrode Chips"

Analyst, **2003**, 128, 1401-1405.

8) Ueno, K.; Kitagawa, F.; Kitamura, N.

"One-Step Electrochemical Cyanation Reaction of Aromatic Hydrocarbons in Polymer Microchannel-Microelectrode Chips"

Bull. Chem. Soc. Jpn., submitted.

9) Kitamura, N.; Hosoda, Y.; Ueno, K.; Iwata, S.

"An Application of Plastic Microchannel-Microheater Chips to a Thermal Synthetic Reaction"

Anal. Sci., submitted.